Understanding Interfacial and Spin-Orbit Torque Effects in Thin Film Magnetic Multilayers.

BEN NICHOLSON

Understanding Interfacial and Spin-Orbit Torque Effects in Thin Film Magnetic Multilayers.

Ben Nicholson

A Thesis presented for the degree of
Doctor of Philosophy

Centre for Materials Physics
Department of Physics
Durham University

PhD? Doesn't look so bad,
I'll have it done by the end of the week...
- Ben Nicholson, far too often.

Abstract

The understanding of both the fundamentals of spin-orbit torques and the potential avenues for spin-orbit exploitation is crucial for the development of future spintronic devices. Accurate quantification of the relevant parameters, such as the spin-orbit effective field strengths, is vital for both performance comparisons and the understanding of the physical origins. In this work, a common effective field measurement technique is probed for its potential inaccuracies, a new method for achieving field-free magnetic reversal is demonstrated and both the structural and magnetic property variations in structurally inverted thin films are investigated.

The design, construction and commissioning of a multi-functional MOKE instrument has been presented. The multi-functional nature of the instrument allowed for sample environments which included the simultaneous application of external fields and sample charge currents for spin-orbit torque effect measurements.

Raster scanned 2D MOKE data were collected for multiple samples based upon a 20 µm-wide perpendicularly magnetised Pt/Co/Pt rectangular bar. Each rectangular bar had a differing lateral displacement with respect to the 60 µm wide electrical contacts, with positions varying from the centre of the electrical contacts to being parallel with the edge. It was shown that the series of samples exhibit deterministic bi-directional field-free magnetic reversal. After discussing the previously known methodologies for field-free magnetic reversal, a new methodology was required in order to explain the symmetry of the results, where the charge current Oersted field is the cause of both the initial domain nucleation and the overall bi-directional magnetic reversal pattern.

The accuracy of a common methodology for quantifying the spin-orbit effective fields was studied by probing the effect of magnetic reversal. It was shown that if magnetic reversal occurs when otherwise unwanted, the resultant effective field values can be exaggerated by over an order of magnitude compared to their typical values. This inaccuracy can be undetectable, particularly in thin films with non unity magnetic remanence.

Structural and magnetic property variations in Pt/CoFeTaB/Ir, together with its structural inverse, were probed with a variety of techniques including polarised neutron reflectometry. Both structural and magnetic variations were observed, with the most dominant change being a Curie temperature variation of over 100 K, where Ir/CoFeTaB/Pt is paramagnetic at room temperature whereas Pt/CoFeTaB/Ir is ferromagnetic.

Declaration

Unless stated otherwise, the work in this thesis is solely that of the author. No part of this thesis has been submitted elsewhere for any other degree or qualification.

The construction of the MOKE instrument involved the manufacture of various parts including mounting brackets, sample holders, cryostat housings and optics bench support frames. All designs were completed by the author, while the manufacturing was undertaken by the mechanical workshop team within the physics department.

The energy dispersive X-ray measurements presented in chapter 7 were performed at the GJ Russell Microscopy Facility at Durham University. The sample lamella was fabricated by Dr Joseph Troughton and the measurement was performed by Dr Budhika Mendis. The author was present for all stages and the analysis was completed solely by the author.

The data collection for the polarised neutron reflectivity data presented in chapter 7 involved the work of many colleagues, including the beamline scientists, Dr Christy Kinane and Dr Andrew Caruana, as well as university colleagues, Dr Aidan Hindmarch, Dr Oto-Obong Inyang, Dr Ariam Mora-Hernandez and Mr Sam Moody. All analysis was performed by the author.

Finally, the vibrating sample magnetometer measurements presented in chapter 7 were performed by the author in the materials characterisation laboratory at the ISIS neutron facility with the assistance of Dr Gavin Stenning.

Acknowledgements

Firstly, I would like to thank my supervisor Dr. Aidan Hindmarch for his guidance, support and friendship over the years and, in particular, for entertaining my experimental ideas and encouraging me to continue tinkering with instruments, without which my interest in instrument development would certainly not have transpired. I would also like to thank Prof. Del Atkinson for the occasional reminders that I must stop tinkering and take some measurements!

I am grateful for the warm welcome provided by Dr. Christy Kinane, Dr. Andrew Caruana and Dr. Laurence Bouchenoire while attending many beamline experiments. Although I have recently transitioned from a synchrotron user to a synchrotron developer, my decision to pursue a career at an international research facility would not have happened if it was not for all those that I have met during these visits.

This work would not have been possible without the support of Stephen Lishman and the rest of the mechanical workshop team. I would also like to thank the Level 2 technicians, Dr. Jason Anderson, Mr Kristian Whatcott and Mr Reece Stockport for providing many a fun afternoon whilst teaching and for never saying no when asked to borrow equipment.

It has been a pleasure to share my time at Durham with Charles Swindells, Ariam Mora-Hernandez, Oto-Obong Inyang, Joe Troughton, Alejandro Galan-Gonzalex, João Luis, Kalel Alsaeed, Thomas Hicken, Luke Turnbull, Sam Moody and Zachary Hawkhead. Thank you for the great discussions, whether physics related or not, which kept us all going.

Finally, I would like to thank my family for their unlimited support over the years.

List of publications

Field-Free Current-Induced Magnetic Reversal Activated by the Oersted Field.
B. Nicholson, M.D. Cooke, A.T. Hindmarch.
In preparation.

PNR and FMR Studies of CoFeTaB Thin Films with Pt and Ir Capping Layers.
B. Nicholson, M. Tokaç, C.J. Kinane, A. Caruana, A. Mora-Hernández,
O. Inyang, S. Moody, A.T. Hindmarch.
In preparation.

Proximity Induced Magnetization in Co_2FeAl Ultrathin Films: Effects of the Annealing Temperature and Heavy Metal Material.
A. Mora-Hernández, **B. Nicholson**, O. Inyang, A.T. Hindmarch, M. Belmeguenai,
Y. Roussign, H. Bouloussa, S.M. Chrif, A. Stashkevich, M. Nasui, M.S. Gabor.
In preparation.

Dzyaloshinskii-Moriya Interaction in Multilayers with Engineered Interfacial Roughness.
A. Mora-Hernández, **B. Nicholson**, A.T. Hindmarch, M. Belmeguenai,
Y. Roussign, A. Huxtable, T.A. Moore.
In preparation for submission to Physical Review B.

Proximity-Induced Magnetism in Pt Layered with Rare-Earth–Transition-Metal Ferrimagnetic Alloys.
C. Swindells, **B. Nicholson**, O. Inyang, Y. Choi,
T. Hase, D. Atkinson.
Physical Review Research 2.3, 033280 (2020)

Ferromagnetic Resonance of FeNi/Cu/FeNi Thin Film on Coplanar Waveguide with Operating Frequency of 1 to 20 GHz.
S.V. Shcherbinin, S.O. Volchkov, C. Swindells, **B. Nicholson**,
D. Atkinson, G.V. Kurlyandskaya.
Russian Physics Journal 63, 1-8 (2020)

Threshold Interface Magnetization Required to Induce Magnetic Proximity Effect.
O. Inyang, L. Bouchenoire, **B. Nicholson**, M. Tokaç, R.M. Rowan-Robinson,
C.J. Kinane, A.T. Hindmarch.
Physical Review B 100.17, 174418 (2019)

Thickness Dependence of the Dzyaloshinskii-Moriya Interaction in Co_2FeAl Ultrathin Films: Effects of Annealing Temperature and Heavy-Metal Material.
M. Belmeguenai, Y. Roussign, H. Bouloussa, S.M. Chrif, A. Stashkevich,
M. Nasui, M.S. Gabor, A. Mora-Hernández, **B. Nicholson**,
O. Inyang, A.T. Hindmarch.
Physical Review Applied 9, 044044 (2018)

Contents

Chapter 1

Introduction

Spin-induced phenomena is at the heart of both current and future magnetic element based memory devices. After the discovery of giant magnetoresistance by Albert Fert [1] and Peter Grünberg [2] in 1988, further advances have been made, such as tunnelling magnetoresistance [3–6], which have now become the standard in modern hard disc drive read heads. While the hard disk drive has revolutionised the world of data storage, new spin current based devices have begun to enter the market in recent years [7]. Since existing hard disc drive technologies rely on magnetic fields for the writing of each magnetic element [8], there is a limit to the maximum data storage density before the stray magnetic field begins to interfere with the neighbouring magnetic elements. Spin current devices, based on either the spin transfer torque or spin-orbit torque, write each magnetic element directly through the use of a spin current [9]. These early magnetic memory technologies offer many advantages over existing hard disc drive devices including the absence of magnetic field-induced writing.

Of particular interest in this thesis is the spin-orbit torque phenomena. This effect begins with a material which exhibits spin-orbit coupling. Heavy metals are typically used [10–12], with Pt and Ir being used within this thesis. As a charge current propagates through the heavy metal, a transverse spin current is created which, if the heavy metal is in isolation, causes spin accumulation at the edges of the material. The polarity of spin accumulation is opposite for opposing interfaces. When an adjacent layer is introduced, the spin current can continue to propagate across the interface and enter the second layer rather than accumulate at the interface. If this second layer is ferromagnetic, a torque is exerted upon the magnetisation. This torque has been shown to be strong enough to induce magnetic reversal [13–17].

For device applications, a method of symmetry breaking is required to achieve deterministic magnetic reversal. Current methods include exchange biasing from an-

tiferromagnets [18, 19], piezoelectric substrates [20], tilted anisotropies [17, 21, 22] and out-of-plane spin polarisations [23–26]. Two important factors in the choice of methodology is the scalability of the magnetic element size [27] and the compatability with current CMOS production methods [28]. Devices must offer an avenue to scale the technology down to sizes which are, at the very least, comparable to current data storage devices. As each device will require secondary architecture embedded within the chip, the processes required to create the magnetic elements must be consistent with current CMOS processes and vice versa. Within this thesis, a new method for achieving the required symmetry breaking is presented, in which the Oersted field and the spin current from an applied charge current can induce magnetic reversal.

For effective comparisons between device performances, accurate quantification of the spin current generation is required. This is often achieved with the measurement of the effective field strengths [29–32]. There are two effective fields that arise from different origins; the damping-like effective field arises from the spin Hall effect and the field-like effective field is caused by the Rashba effect. The spin Hall effect is a bulk effect in which spin-dependent scattering occurs within the heavy metal layer. The Rashba effect is an interfacial effect in which a potential gradient is induced across the interface. Both of these effects are discussed in detail in chapter 2. These effective fields can be measured, where stronger field strengths are desired for more efficient magnetic reversal. The strength of the spin-orbit torques is often characterised by the spin Hall angle, which represents the ratio of induced spin current to applied charge current [33–35].

An important factor which influences the spin-orbit torque strength is the local structural and magnetic properties at the interface. Efforts have been made to tailor the interface structure in order to improve the interface transparency [36, 37], which is quantified by the spin mixing conductance [38]. Local changes in the crystalline structure, element composition or magnetisation can influence the spin mixing conductance and, hence, spin-dependent phenomena such as spin-orbit torque-induced magnetic reversal.

1.1 Aims of the thesis

The overarching aim of this thesis is to further the understanding of spin-orbit torques in the context of spintronic device applications. Perpendicularly magnetised Pt/Co/Pt trilayer structures were fabricated in order to demonstrate field-free magnetic reversal through a novel method, which may offer better scalability and

compatibility over the currently discovered methods. Furthermore, a detailed understanding of the influence of magnetic reversal on spin-orbit torque effective field measurements is presented, which may explain the variation in reported spin-related quantities within the literature. Another explanation for the variations reported in the literature is that of differing thin film and/or interface qualities. Studying the structural, magnetic and alloy composition variations across Pt/CoFeTaB/Ir thin films may lead to both a greater understanding of the physical origins of the observed phenomena and enhanced optimisation for spintronic devices.

1.2 Thesis outline

This thesis begins by presenting the theoretical aspects relevant for the later works. Chapter 2 begins with a brief overview of the fundamentals of magnetism before detailing spin-orbit torques. Within this section, the origins of the spin Hall and Rashba effects are discussed together with their impact upon the Landau-Lifshitz-Gilbert equation.

Chapter 3 presents the experimental techniques used throughout this thesis. These range from the sample fabrication techniques of magnetron sputtering and photolithography, to X-ray and neutron reflectivity techniques. The reflectivity discussion includes both specular and off-specular techniques and concludes with a brief overview of the data fitting procedure.

Chapter 4 details the theoretical, experimental and instrument design aspects of a magneto-optical Kerr effect (MOKE) instrument. After beginning with an overview of a typical instrument, a discussion of the various pathways available in order to produce such an instrument is presented. The latter half of the chapter details the commissioning of the MOKE instrument.

In chapter 5, current-induced magnetic reversal is demonstrated along with a novel method for achieving field-free magnetic reversal. The chapter opens with extensive sample characterisation, before presenting trial measurements in order to understand any unwanted sample heating effects. The chapter proceeds by varying the lateral offset of a 20 µm wide rectangle with respect to the 60 µm wide electrical contact pads. The current distribution is simulated, with the chapter concluding by comparing the simulated Oersted field symmetries with that of the observed field-free magnetic reversal results.

Chapter 6 investigates the potential inaccuracies of a common spin-orbit torque effective field measurement technique. In particular, the effect of magnetic reversal is probed in instances when only magnetic axis tilting is desired. A detailed method

is presented which isolates the magnetic reversal contribution through the use of the hysteresis loop remanence, before concluding with a comparison to typical effective field strength values.

Chapter 7 shows the structural and magnetic property variations in trilayer structures of Pt/CoFeTaB/Ir when compared to the structurally inverted thin film of Ir/CoFeTaB/Pt. Both X-ray and neutron reflectivity measurements are presented along with a detailed discussion of the resultant depth-resolved density profiles. The chapter continues by exhibiting magnetisation measurements, obtained through three independent magnetometry techniques, which show a substantial change in magnetic depth profile and Curie temperature.

Finally, chapter 8 concludes the thesis with a summary of the key findings, before exploring the possibilities of future work.

Chapter 2

Theory

2.1 Introduction

This chapter describes the relevant theoretical aspects required throughout this thesis. The chapter begins by detailing the origins of ferromagnetism, before introducing the effective field theory required for the inclusion of spin-orbit torques. spin-orbit torques are central to this thesis and have been described through an explanation of their roots within the spin Hall and Rashba effects. Finally, the spin mixing conductance is briefly described.

As chapter 4 details the construction of a magneto-optical Kerr effect instrument, the theoretical aspects for the interaction of light and magnetism is reserved for chapter 4.

2.2 Fundamentals of magnetism

Magnetism originates from two types of angular momentum within atomic systems, electron spin and orbital angular momentum. The electron spin is a fundamental property of the electron, while the orbital angular momentum is thought of as arising from the electrons' orbit about an atomic nucleus. The electrons within an atom can be arranged such that there is no overall magnetic moment. This occurs in elements with fully occupied electron shells and are termed diamagnetic materials. If elements possess unfilled shells, a net magnetic moment per atom occurs. However, if no interaction exists between atoms, the net moment is of a random orientation and, when averaged over many atoms within a material, no net magnetisation is observed. Under the application of an external magnetic field, the initially random atomic moments can align creating a net magnetisation. These materials are called paramagnets. The third most common form of magnetism within elements is ferro-

magnetism. Here, atoms exhibit a net magnetic moment which interacts with the neighbouring atoms and produces a net magnetisation even in the absence of an external magnetic field. This interaction is called the exchange interaction.

2.2.1 The Heisenberg exchange interaction

While there exists a small dipolar interaction between neighbouring magnetic atoms, the thermal activation at modest temperatures can easily overcome such an energy barrier [39]. Hence, the exchange interaction is required in order to explain room temperature ferromagnetism. The exchange interaction is a quantum mechanical interaction where there exists an overlap of the electronic wavefunction and is explained by the Coulomb force. As electrons are fermionic particles, they are indistinguishable and must obey the Pauli exclusion principle. This means that the electron wavefunction must be antisymmetric upon the exchange of two electrons. The Pauli exclusion principle states that no two electrons can share the same quantum state.

Considering the total wavefunction for a pair of interacting electrons with spatially varying waveforms ψ_i and ψ_j, at positions r_1 and r_2, the total electron wavefunction can be written as,

$$\Psi_S = \frac{1}{\sqrt{2}} \left(\psi_i(r_1)\psi_j(r_2) + \psi_i(r_2)\psi_j(r_1)\right) \chi_S \tag{2.1}$$

$$\Psi_T = \frac{1}{\sqrt{2}} \left(\psi_i(r_1)\psi_j(r_2) - \psi_i(r_2)\psi_j(r_1)\right) \chi_T, \tag{2.2}$$

where χ represents the spin wavefunction and the subscripts S, T represent a singlet and triplet waveform respectively. As the total wavefunction must be antisymmetric under the exchange of two electrons, χ_S must be antisymmetric and χ_T must be symmetric. If the singlet total wavefunction is of lower energy, the electrons will align antiparallel with each other due to the antisymmetric χ_S. Materials where the magnetic moments are ordered antiparallel are termed antiferromagnets. The magnetic materials studied within this thesis are ferromagnets, where the triplet total wavefunction is of lower energy and the symmetric spin wavefunction dictates that electrons align parallel to each other. As the electron spin state within ferromagnets is symmetric, the spatial waveform must be antisymmetric. Hence, electrons of neighbouring atoms cannot occupy the same point in space. The coulomb force is subsequently minimised due to the distance between such electrons, hence, creating an energetically favourable state of spin alignment.

2.2.2 Ferromagnetism

Within ferromagnetic materials, the exchange interaction causes electron spins to favour parallel alignment. This creates long range ordering of the atomic moments which produces a net magnetisation. At high temperatures, the additional thermal energy can overcome the energy barrier created by the exchange interaction to break the preference of parallel spin alignment. At these temperatures, the magnetic moment per atom remains while the exchange interaction is nullified, therefore, the material behaves as a paramagnet. The point of transition is called the Curie temperature, T_C, and can be modelled in the mean-field approximation with the Curie-Weiss law,

$$\chi = \frac{C}{T - T_{\mathrm{C}}}, \tag{2.3}$$

where C is a material specific constant, T is the temperature and χ is a magnetic susceptibility.

The magnetic susceptibility describes the response of a system to an external magnetic field. For an applied field $\vec{H}$, the induced magnetisation, $\vec{M}$, can be written as,

$$\vec{M} = \chi \vec{H}. \tag{2.4}$$

Ferromagnets typically exhibit large, positive values for the magnetic susceptibility. The non-zero magnetisation observed in the absence of an external magnetic field can be explained by the inclusion of an internal field. Weiss proposed an internal molecular field, H_m, which is proportional to the magnetisation,

$$H_m = \lambda M. \tag{2.5}$$

where λ is a material dependent proportionality factor often referred to as the molecular field constant.

2.2.3 Magnetic domains

The previous discussions of ferromagnetism explain the presence of a spontaneous magnetic moment in the absence of an external field. However, ferromagnets can exhibit a net zero magnetic moment if the material is divided into magnetic domains,

with the magnetisation in each domain pointing in different directions. The reason for the existence of magnetic domains is a minimisation of the magnetostatic energy due to the demagnetisation field.

The parallel alignment of magnetic moments creates a magnetic field within the same material. This magnetic field is in the opposite direction to the aligned spins, hence, it is termed the demagnetisation field. The magnetostatic energy is the magnetic potential energy of a magnetic body within a magnetic field. The magnetostatic energy density, ϵ_{ms}, is proportional to the stray field, H_{S},

$$\epsilon_{\mathrm{ms}} = \frac{\mu_0}{2} H_{\mathrm{S}} \cdot M_{\mathrm{S}}. \tag{2.6}$$

where M_{S} is the saturation magnetisation. For the case of a single domain, there is a large magnetostatic energy contribution from the demagnetisation field due to the stray field being parallel to the local magnetisation vector. However, by introducing magnetic domains with random magnetisation directions within the system, long range demagnetisation fields are reduced due to the reduced average magnetisation vector. Subsequently, the magnetostatic energy contribution is also reduced.

There exists other energy contributions, including Zeeman, magnetocrystalline, magnetostriction and the previously introduced exchange energy (due to the exchange interaction). By introducing magnetic domains within a material, the magnetostatic energy is reduced, but this is at the cost of an increase in the magnetocrystalline and exchange energy (and in some cases, the magnetostriction energy). At the border of two domains with magnetisation vectors in differing directions, the border spins must rotate from being parallel to the magnetisation within domain one, to being parallel to the magnetisation of domain two. This rotation in spins is called a domain wall. The exchange energy increase is caused by the spins no longer being parallel to their neighbours. The magnetocrystalline energy cost is due to the likelihood of some domain wall spins not being aligned along a magnetic easy axis. Both the domain size and density, together with the domain wall size, are dependent upon the relative strengths of the individual energy contributions.

2.2.4 Effective magnetic fields

In the previous section, it was stated that the magnetic configuration of a material is a result of a minimisation of the various energies at play. To simplify the analysis, an effective magnetic field can be introduced. Each magnetic energy contribution can be written in the form of an effective field. For example, the magnetocrystalline

anisotropy energy describes the preferential alignment of spins along particular crystallogaphic directions. This can be thought of as an effective magnetic field along the the magnetocrystalline easy axis. The effective fields from all energy contributions can be summed to produce a single effective field vector. The observed magnetisation dynamics can be subsequently explained through the use of a single effective field parameter.

The following section introduces spin-orbit torques by first introducing the spin-orbit interaction. The impact of spin-orbit torques on ferromagnetic materials is subsequently described through the use of spin-orbit effective fields within the Landau-Lifshitz-Gilbert equation.

2.3 Spin-orbit torques

Spin-orbit torques (SOTs) describe the mechanism in which the magnetisation can be influenced by the application of an electrical current in the presence of the spin-orbit interaction. SOTs originate from two effects, the spin Hall effect and the Rashba effect, both of which have been widely studied in ferromagnetic/heavy metal bilayers [40–43]. Here, the heavy metal contributes a strong spin-orbit interaction which can influence the magnetic behaviour of the adjacent ferromagnetic layer.

To explain spin-orbit torques, it is useful to first consider magnetic dynamics in the absence of spin-orbit torques. The Landau-Lifshitz-Gilbert (LLG) equation describes the time evolution of the magnetisation in terms of effective fields from sources including internal and external fields. Therefore, if spin-orbit torques can be displayed as an effective field, it is possible to extend the LLG equation to include such phenomena.

2.3.1 Spin-orbit interaction

The spin-orbit interaction (SOI) describes the relativistic coupling between the electron spin and the orbital angular momentum and is responsible for many spin-related phenomena, including the spin Hall and Rashba effects. These two effects will be discussed in a later section after a description of the SOI has been presented.

While the SOI is a relativistic phenomenon, much like other relativistic effects, there often exist (semi)classical models which can be used to aid understanding. By using a semiclassical model, the spin-orbit interaction can be explained through the example of an electron orbiting a positively charged nucleus. Figure 2.1(a) represents the model that the majority of readers would instinctively think of, in which the nucleus is static and the electron follows an orbital motion. However, we

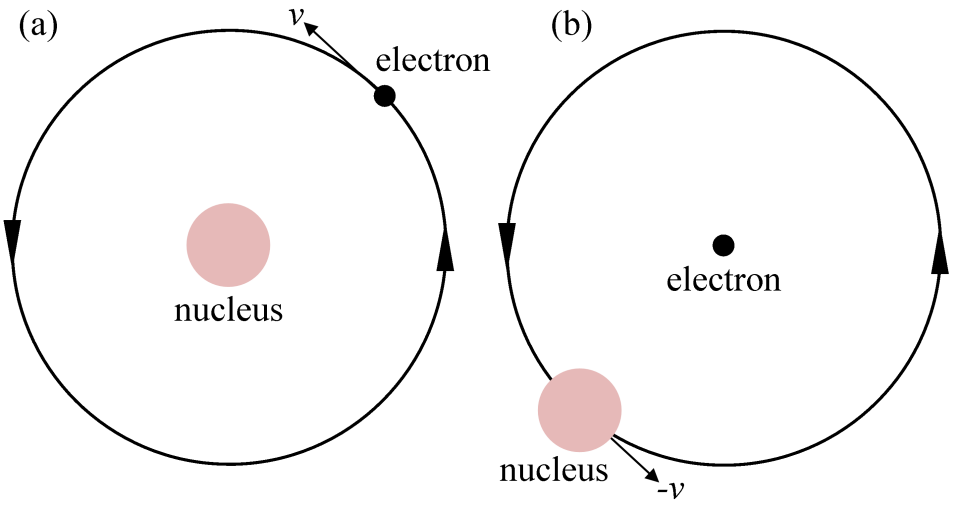

Figure 2.1: (a) Electron orbiting a nucleus with velocity v, in the reference frame of the nucleus. (b) When transformed to the electrons frame of reference, the nucleus is orbiting the electron with a velocity of -v.

can transfer this scenario into the reference frame of the electron (figure 2.1(b)), such that it is now the positive nucleus which is orbiting the electron. Due to the presence of a flowing positive charge (the orbiting nucleus), a magnetic field is created at the location of the electron which interacts with the electron spin, giving rise to the appropriately named SOI. The strength of the SOI scales with Z^4 for core states, where Z is the atomic number. Other electron states, such as conduction electrons, see a reduced potential and, hence, a reduced atomic number scaling. The overall SOI scaling is approximately Z^2 [44], which is why heavy metals such as Pt, Ir and Ta are often used within the literature. Shanavas *et al.* [44] also show the relative change in spin-orbit coupling strength for differing atomic shells, hence, transition metals with 5d electron states at the Fermi energy, such as Pt, exhibit a higher spin-orbit interaction strength than the likes of Au, which has only s-states at the Fermi energy.

2.3.2 Landau-Lifshitz-Gilbert equation

The LLG equation is commonly shown as

$$\frac{d\vec{M}}{dt} = -\gamma\vec{M} \times \vec{H}_{\text{eff}} - \frac{\alpha}{M_{\text{S}}}\vec{M} \times (\vec{M} \times \vec{H}_{\text{eff}}), \tag{2.7}$$

where γ is the gyromagnetic ratio, α is the damping constant and $\vec{H}_{\text{eff}}$ is the total effective field dictating the equilibrium orientation of the magnetisation. This

equation describes the magnetisation dynamics, in particular the $\vec{M} \times \vec{H}_{\text{eff}}$ term represents the precessional motion of the magnetisation around the effective field and the second term, $\vec{M} \times (\vec{M} \times \vec{H}_{\text{eff}})$, describes the relaxation of such precessional motion towards the effective field. The dimensionless Gilbert damping parameter, α, describes the scale of precessional energy dissipation to the lattice and, hence, the speed of magnetisation relaxation.

There are two types of damping, intrinsic and extrinsic. Intrinsic damping occurs due to scattering between electrons and uniform magnons. The energy contained within the magnon is transferred to the electron, promoting the electron to an excited state while annihilating the magnon. The excited electron state can then decay to its ground state through scattering with phonons and/or lattice defects. Extrinsic damping describes the process in which the primary scattering mode first decays into secondary non-uniform modes, which subsequently decay to the lattice.

When a ferromagnet is interfaced with a non-magnetic metal, an enhancement of damping can occur due to spin pumping. Due to the accumulation of one spin state at the ferromagnetic interface, a spin current can flow across the interface into the non-magnetic layer. The spin current undergoes scattering events which, due to the equal number of spin up and spin down states within the non-magnetic layer, undergoes spin-flip scattering events. The spin polarisation decays over a characteristic length scale termed the spin diffusion length. A spin back-flow can also occur, in which a spin current propagates from the non-magnetic layer to the ferromagnetic layer exerting a torque upon the magnetisation.

2.3.3 Spin-orbit torques

Spin-orbit torques are introduced into the LLG equation as an effective field,

$$J\vec{\sigma} = a\vec{\sigma} \times \vec{M} + b\vec{\sigma}, \tag{2.8}$$

where J describes the exchange coupling, σ represents the spin accumulation and a and b are material dependent scaling parameters [45]. When this effective field is included, equation 2.7 becomes

$$\frac{d\vec{M}}{dt} = -\gamma\vec{M} \times (\vec{H}_{\text{eff}} + J\vec{\sigma}) - \frac{\alpha}{M_{\text{S}}}\vec{M} \times (\vec{M} \times (\vec{H}_{\text{eff}} + J\vec{\sigma})). \tag{2.9}$$

The $J\vec{\sigma}$ term within the second term of equation 2.9 is often neglected since $\alpha << 1$. The inclusion of spin-orbit torque effective fields produces two new terms within

the LLG equation. Named due to their similarity to the original two terms, they are the field-like torque of $b\vec{M} \times \vec{\sigma}$ and the damping-like torque of $a\vec{M} \times (\vec{\sigma} \times \vec{M})$. The damping-like torque directly drives magnetic switching and the field-like torque reduces the energy barrier. It is thought that the damping-like torque is predominantly produced by the spin Hall effect (SHE) and the field-like torque is predominantly produced by the Rashba effect. As it is difficult to separate these two effects, this statement remains unproven yet widely accepted.

2.3.4 Spin Hall effect

The SHE occurs due to both intrinsic and extrinsic effects in many materials, including non-magnetic materials with strong spin-orbit coupling [46, 47]. As a charge current flows through a strongly spin-orbit coupled material, for example Pt, Ta or W, opposite spins will gain opposite transverse velocities, creating a transverse spin current. This is a pure spin current, i.e. zero net charge flow.

Extrinsic contributions can be described by two scattering mechanisms, skew scattering [48] and side jump scattering [49]. The first contribution, skew scattering, is a product of asymmetric scattering probabilities in semi-classical Boltzmann transport theories and was first proposed by Smit [48]. Inclusion of the spin-orbit interaction in the disordered scattering potential results in different scattering cross

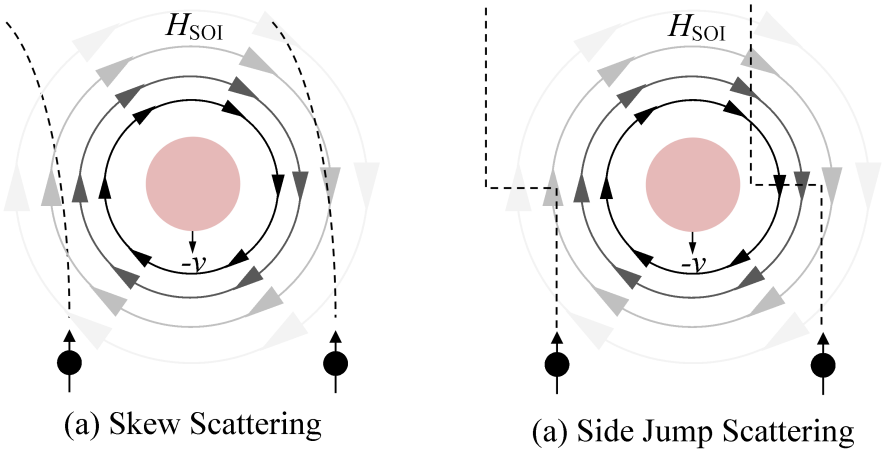

Figure 2.2: (a) In the frame of reference of the electron, an approaching heavy metal ion produces an effective field, H_{SOI}, which attracts (repels) spin up electrons which pass the the right (left) of the ion. (b) Due to the gradient of the effective field, the electron density function becomes asymmetric, such that there is a finite probability of a spontaneous lateral displacement in the electrons position. The effective field gradient is represented by the fading concentric circles, with darker circles representing a stronger effective field.

sections for electron spins that are aligned parallel or anti-parallel to the spin-orbit effective field. This induces opposite transverse velocities for opposite spins due to the different scattering probabilities and is shown graphically in figure 2.2. When viewing the scattering event from the electron's frame of reference, an impurity with strong spin-orbit coupling travelling towards the electron produces an effective magnetic field gradient. When the electron interacts with such effective field gradient, it is either attracted or repelled by the impurity depending on whether the effective field and electron spin are anti-parallel or parallel respectively. Figure 2.2 shows that the induced transverse velocity for one spin state is independent upon which side of the impurity the electron passes. It is also clear that the opposite spin state will acquire an opposite transverse velocity.

The second extrinsic effect, side jump scattering, is also a result of the effective field gradient and was first proposed by Berger [49]. In the absence of a magnetic field, the position of an electron is described by a Gaussian probability distribution. When an impurity with an associated local effective field gradient is introduced, an asymmetry is induced within the electron's position probability distribution which causes the distribution to deviate slightly from the original Gaussian shape. Therefore, there exists a finite probability that the electron is spontaneously displaced laterally. The induced asymmetry in the electron position probability distribution is opposite for electrons of opposite spin and, consequently, produces lateral displacements in opposite directions for opposing spin states.

Intrinsic effects, proposed by Luttinger and Karplus [50], are related to the band structure of the host material [51]. Contrary to skew and side jump scattering, an intrinsic spin current is generated between scattering events rather than during. To explain this effect, the spin-orbit coupling is introduced into the band structure calculations which can split certain bands. If the Fermi level is at approximately the same point as these spin-orbit split bands, this effect can dominate the conductivity and produce a transverse spin current.

2.3.5 Rashba effect

The Rashba effect occurs when structural inversion asymmetry (SIA) is present, in particular at the interface of two distinct materials [52]. The asymmetry produces a potential gradient along the axis of symmetry breaking (normal to the sample surface) in the reference frame of the lattice. When this electric field is transformed into the reference frame of the electron, it becomes a magnetic field perpendicular to the electron motion and within the sample plane. This magnetic field interacts with the conduction electrons to form an effective magnetic field, often referred to

as the Rashba effective field, given by [53],

$$\vec{H}_{\mathrm{R}} = \alpha_{\mathrm{R}}(\hat{z} \times \langle \vec{k} \rangle), \tag{2.10}$$

where α_{R} is a material dependent spin-orbit strength factor, $\hat{z}$ is a unit vector parallel to the electric field and $\langle \vec{k} \rangle$ is the average conduction electron wave vector. Under the application of a charge current, $\langle \vec{k} \rangle$ becomes non-zero which produces an effective field perpendicular to the electron flow. In a non-magnetic material, the Rashba effect causes spins to align perpendicular to the electron motion remaining within the sample plane. In a ferromagnetic material with perpendicular magnetic anisotropy, the Rashba field causes the spins to cant away from the magnetic easy axis.

In both cases, the spin polarisation is k dependent, therefore, it is possible to induce a spin polarisation under the application of an electrical current. In the non-magnetic case, an electric current propagating along the x axis produces a spin polarisation in the y direction for majority spins and $-y$ direction for minority spins. As the majority spin contour is larger, a net spin polarisation is achieved in the y direction. For the ferromagnetic case, in terms of the effective magnetic field H_{R}, conduction electrons will precess about the local effective field creating a torque on the magnetisation.

2.3.6 Spin Hall angle

The efficiency of spin-orbit torques is often quantified through the spin Hall angle, $\theta_{\mathrm{SH}} = j_s/j_e$, which is the ratio of the spin current (j_s) to the charge current (j_e) [33]. Typical values are in the range of ± 0.3, with the typical values for commonly used materials shown in table 2.1. The spin Hall angle scales with the magnitude of the SOI, yet also depends upon sample specific properties such as the proximity-induced magnetisation and effective spin mixing conductance. Theoretical predictions [54] agree well with both the sign and magnitude of experimental values in the majority of cases [55]. The remaining variances and/or inaccuracies are often explained by changes in the effective spin mixing conductance at the interface and/or measurement techniques. The quality of such interfaces, including the surface roughness and intermixing, partly determines the interface spin transparency and, hence, the value of the spin Hall angle observed. Other properties, such as the ferromagnetic material choice and heavy metal thickness, also play a role in the interface transparency and, hence, the spin Hall angle measured [56].

	Au	Pt	Ir	Ta	W
Spin Hall angle	0.003 to 0.11	0.03 to 0.1	0.02	-0.02 to -0.12	-0.33

Table 2.1: Typical spin Hall angles for common heavy metals. A more detailed comparison of literature values can be found in the works of Hoffmann [59] and Sinova [57].

There exists several measurement techniques available for spin Hall angle determination. As differing techniques can be susceptible to different sources of error, it is possible to achieve results that vary by over an order of magnitude for the same structure, as detailed by Sinova *et al* [57]. Using Pt as an example, the spin Hall angle has been reported as low as 0.0037 in non-local inverse spin Hall effect electrical measurements [58]. This experiment was particularly susceptible to the interface spin transparency at multiple locations which can distort the measured spin Hall angle. Other studies which involve spin pumping, spin transfer torque and spin Hall magnetoresistance measurements report a range of values covering an order of magnitude. This is partly due to the various techniques differing significantly with respect to (i) the driving perturbation, (ii) the probed observable, (iii) the magnetization and external-field geometry, (iv) the use of either the direct or the inverse SHE and (v) the possible frequency range.

2.3.7 Spin mixing conductance

The spin mixing conductance was first developed in order to quantify the spin current relaxation in non-magnetic materials [60]. The spin mixing conductance is used extensively in spin-pumping theory, where a spin current generated by magnetic precession within a ferromagnetic layer propagates into an adjacent non-magnetic layer. The angular momentum from the spin current is dissipated to the non-magnetic lattice through the SOI. The spin mixing conductance, $G^{\uparrow\downarrow}$, can be defined in terms of real and imaginary parts,

$$G^{\uparrow\downarrow} = G_{\mathrm{r}} + iG_{\mathrm{i}}. \tag{2.11}$$

The imaginary term is often assumed to be negligible in comparison to the real term.

To better represent experimental observations, the spin mixing conductance was expanded to include an interfacial contribution and was subsequently called the effective spin mixing conductance. For a ferromagnetic/heavy metal bilayer (FM/HM), the effective spin mixing conductance can be written as (in the limit of $G_{\mathrm{r}} >> G_{\mathrm{i}}$)

$$G_{\text{eff}}^{\uparrow\downarrow} = \frac{G_{\text{HM/FM}}^{\uparrow\downarrow}}{1 + \frac{2G_{\text{HM/FM}}^{\uparrow\downarrow}}{G_{\text{HM}}^{\uparrow\downarrow}}}, \tag{2.12}$$

where $G_{\text{eff}}^{\uparrow\downarrow}$ is the bare interfacial spin mixing conductance and $G_{\text{HM}}^{\uparrow\downarrow}$ is the spin conductance of the heavy metal layer.

The effective spin mixing conductance can be broken down into its respective components, namely, reflection and transmission probabilities for spin up and spin down electrons at an interface, with more details in other works [61–63]. The effective spin mixing conductance, and hence the efficiency of magnetic reversal through spin-orbit torque, can be influenced by the interfacial crystal structures [64] and material choice [65], therefore, sample quality and overall structure plays a key role in the effective spin mixing conductance and any subsequent spin-dependent behaviour.

Chapter 3

Experimental techniques

3.1 Introduction

This chapter presents the experimental techniques used to fabricate and characterise the thin film structures used throughout this thesis. All samples were grown using magnetron sputtering, with the samples used in chapters 5 and 6 requiring photolithographic patterning. The measurement technique of reflectometry is then discussed in the context of both X-ray and polarised neutron sources. Both of these techniques provide a non-destructive method to resolve the structural information, with additional magnetic information being provided in the case of polarised neutron reflectivity.

While a magneto-optical Kerr effect instrument is used extensively throughout this work, details of the technique is reserved for chapter 4.

3.2 Sample preparation

All samples presented within this thesis were grown on single crystal silicon wafers (001 orientation) which included a 100 nm thick thermally grown SiO_2 surface layer for improved surface roughness. Sample sizes ranged from 5 mm $\times$ 5 mm to 30 mm $\times$ 30 mm depending on the measurement requirements and were cut from a six inch diameter wafer. Samples that did not require lithographic patterning were cut to size prior to the film deposition. However, when lithographic patterning was required, the sample size was initially cut larger than the final dimensions required, before cutting to the final size post film deposition. Further details can be found in section 3.2.2. Prior to any film deposition or lithographic work, the samples were cleaned with the common wet processing method of an acetone bath, followed by an isopropanol wash, for approximately two minutes each within an ultrasonic bath.

The samples were dried with N_2 gas and the time between completion of the cleaning process and the beginning of the following thin film processing technique was kept to a minimum (generally less than 30 minutes).

3.2.1 Magnetron sputtering

Magnetron sputtering is a physical vapour phase deposition technique in which material is removed from a target through charged ion bombardment. The atoms removed from the target propagate through the vacuum chamber until a surface is met, at which point the atoms condense onto the surface. Over time, more atoms condense on the surface to build up the required thin film.

A simplified view of the sputtering process is shown in figure 3.1. Under vacuum, the target material is negatively charged while all other components, including the sample stage, vacuum vessel and sputter head shielding are grounded. When Ar gas is introduced to the chamber, ionised Ar atoms are attracted to the cathode and collide with the target surface. The kinetic energy of the Ar ion is transferred to the target material which can eject the target atoms and/or secondary electrons from the target surface. The target atoms propagate through the vacuum, eventually coming into contact with a surface at which they are deposited. The magnets within the sputter head are of alternating polarity, creating a strong magnetic field near

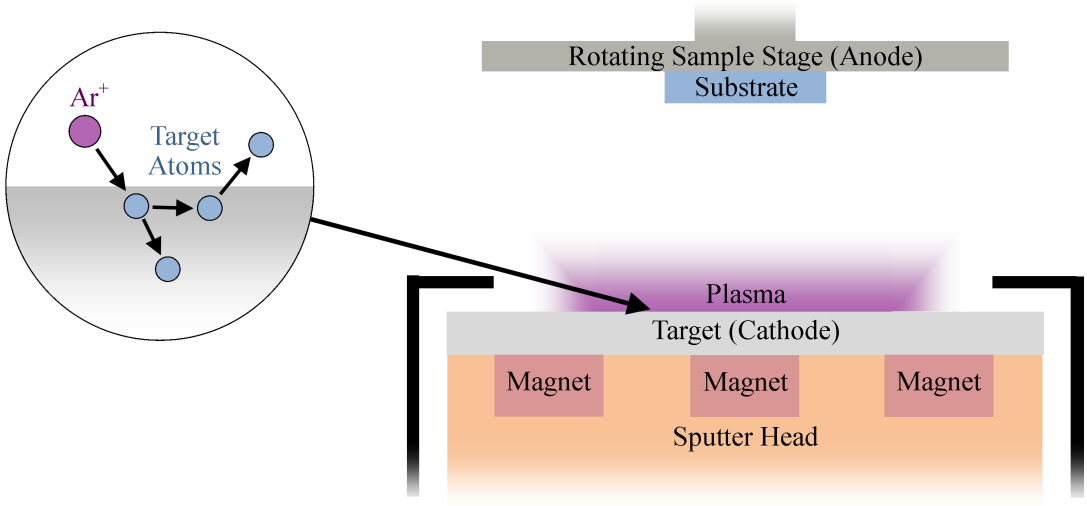

Figure 3.1: Schematic of the important features of a typical magnetron sputtering system. The sputtering system is contained within a vacuum chamber with additional instruments not shown (see figure 3.2). The magnet polarities from left to right are north, south, north, creating a high magnetic field strength near the target surface.

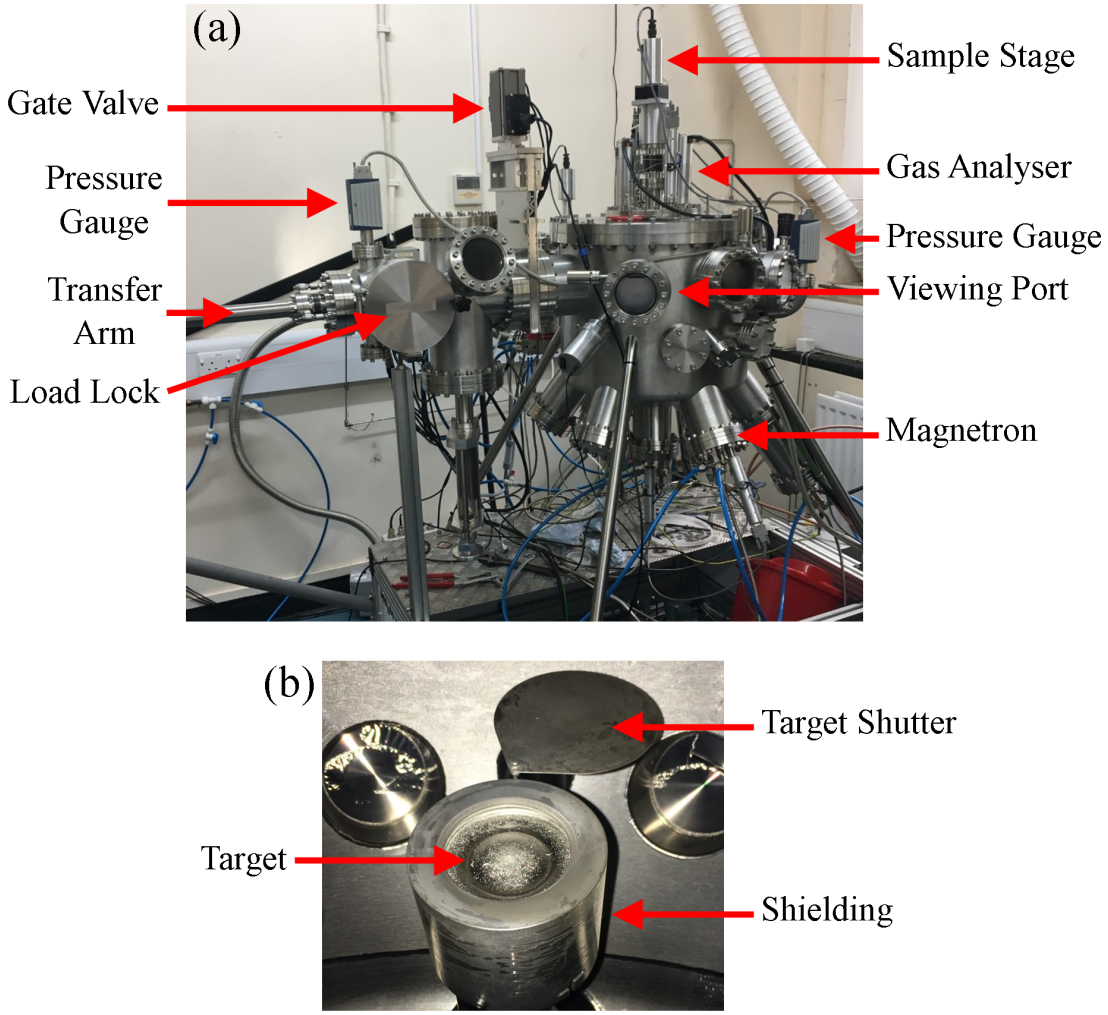

Figure 3.2: (a) Mantis QPrep-500 sputtering system. (b) One of five magnetron sputtering heads within the system. A ring can be observed on the target surface (termed the racetrack) which is caused by the increased sputtering rate at this position due to the increased Ar ion generation within the ring shaped magnet field.

the surface of the target. The primary and secondary electrons within the system become trapped in circular orbits within the magnetic field due to the Lorentz force, creating a plasma in close proximity to the target surface. This creates a local increase in the electron density which increases the ionisation rate of the Ar gas in the immediate vicinity of the negatively charged cathode, thereby increasing the deposition rate. While charging the cathode with a DC bias works for electrically conductive target materials, a positive charge quickly builds up on the surface of insulating materials, hence, a DC bias is unsuitable. Instead, a radio frequency (RF) source is used (typically 13.56 MHz) in order to allow for the positive charge build up to dissipate.

The magnetron sputtering system used within this thesis was a Mantis QPrep-500 sputtering system and is shown in figure 3.2. The system consists of two chambers, a load-lock (left) and the main chamber (right) separated by a gate valve. Due to the smaller chamber volume, the time taken for the load-lock to reach the base vacuum pressure is on the order of three hours, compared to three days for the main chamber. Hence, the presence of the load-lock allowed for more efficient sample fabrication. The typical base vacuum pressure was 1×10^{-7} Torr and the typical deposition Ar gas pressure was 1×10^{-3} Torr. The load-lock chamber contains a storage carousel with space for five samples. This allowed for the deposition of multiple samples without breaking the vacuum which aids in consistency of layer deposition. The samples can be transferred from the load-lock to the main chamber with the use of the transfer arm. The main chamber contains five magnetron sputter heads which can be powered by a DC or RF power supply. An example of the magnetron sputter head is shown in figure 3.2(b). Each sputter head includes a target shutter which covers the target when not in use, preventing cross contamination when an adjacent sputter head is in use.

3.2.2 Photolithography

The samples used within chapters 5 and 6 required micrometre scale dimensions in order to achieve the required current densities. To fabricate such samples, the method of photolithography was employed. Photolithography describes the process in which a pattern is transferred from a mask to an ultraviolet (UV) light sensitive coating on the substrate. It is then possible to deposit the film using standard magnetron sputtering techniques and, after the removal of the UV sensitive coating, a patterned thin film structure is produced.

Photolithography is a five stage process summarised in figure 3.3. First, an UV sensitive film (termed photoresist) is spin coated onto the substrate with an approximate thickness of 1.5 μm. Here, Microposit S1813 photoresist was used, manufactured by Shipley [66]. The substrate is heated to 95 °C for 90 seconds in order to remove the solvent from the photoresist. Secondly, the sample is exposed to UV light through a mask, exposing some areas of photoresist while other areas are shielded. The mask is a transparent quartz slide, with a Cr coating of the required pattern on one side. At this stage, two categories of photolithography become important. Positive lithography describes a photoresist where exposure to UV light breaks the molecular bonds, thereby weakening the exposed areas. Negative lithography describes a photoresist where the bonds are strengthened when exposed to UV light. Within this thesis, only positive lithography is used. Thirdly, after

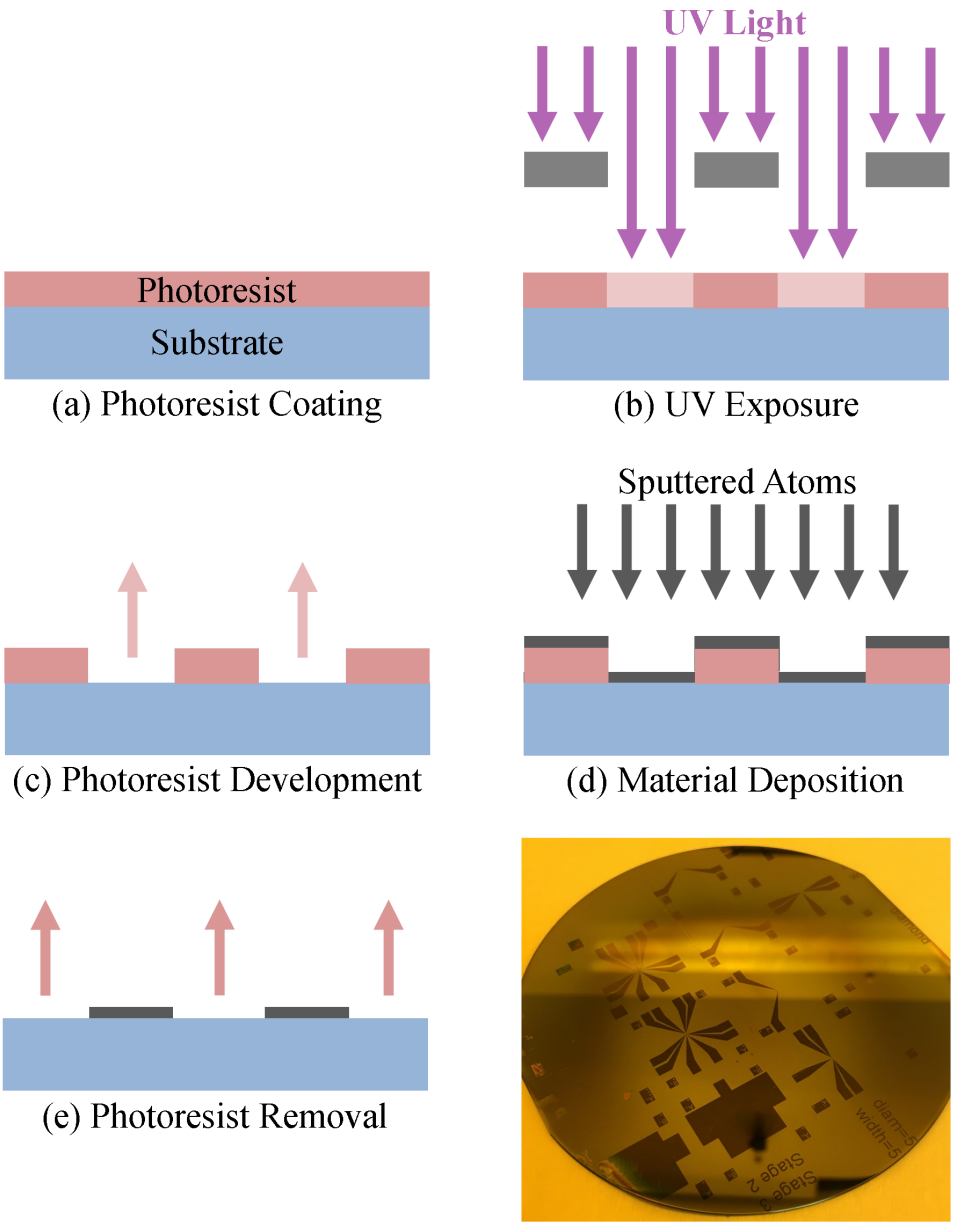

Figure 3.3: Flow chart for the photolithography process, together with an example wafer after three stages of development.

some areas of photoresist have been weakened by UV light, the sample is washed in a developer solution for 30 seconds in order to remove the weakened photoresist. A de-ionised water rinse is performed in order to stop the development process by removing any excess developer solution. Fourthly, the desired thin film structure is deposited following the standard magnetron sputtering deposition process detailed in the previous section. Finally, the sample is washed in an acetone bath to remove all remaining photoresist, before being washed with isopropanol in order to remove any acetone residue. An example wafer after stage three of the lithography process

is also shown in figure 3.3, where the dark blue areas are exposed Si wafer and the lighter areas are photoresist. The process can be repeated in order to build up individual elements of the required sample. For example, the Hall bars used within chapters 5 and 6 require two processes. First, the Pt/Co/Pt Hall bar is deposited following the five step process in figure 3.3. After all of the photoresist has been removed, the process is repeated with a different UV exposure mask, which now allows for the patterning of the electrical contacts rather than just the Hall bar.

A common problem with photolithographic lift-off techniques is the presence of ears at the photoresist walls. During the sputtering process, the deposited atoms do not always impact the substrate at normal incidence. Due to this angular spread, some atoms can be deposited on the side wall of the photoresist. After photoresist removal, the atoms deposited onto the photoresist wall can remain if they are also in contact with the thin film, creating a narrow, elevated region at the edge of the thin film, often termed ears. As the thin film structure will differ in the immediate vicinity of the ears as compared to the bulk thin film, the magnetic properties of the film will also vary. These variations can create magnetic domain wall pinning sites which can make it favourable for domain walls to be nucleated at the sample edges.

The samples used for photolithography have to be larger than their final dimensions due to edge beading effects. When the photoresist is spin coated, material is pushed towards the edge of the wafer. While the majority of material is expelled from the wafer, there remains a small build up of material around the circumference. Evidence of this is shown in the bottom left hand corner of the example image in figure 3.3. Here, edge beading is most clearly observed along the wafer edge in the large dark blue region. Due to the build up of photoresist, this area is thicker than the nominal 1.5 μm. Therefore, this region is underexposed during stage two of the lithography process and not all photoresist is subsequently removed in stage three. To avoid edge beading effects, the sample is initially made larger than required, then after process completion, the outer areas, along with the associated edge beading, are cut away.

3.3 Reflectivity

X-ray reflectivity (XRR) and polarised neutron reflectivity (PNR) are non-destructive techniques which produce depth-resolved structural (and magnetic in the case of PNR) information on thin film samples. While there are some differences between XRR and PNR, both methodologies can be explained in a similar fashion. The theoretical background is presented in detail for XRR, followed by a brief explana-

tion of the differences for PNR. The experimental details for performing both XRR and PNR measurements are then presented, followed by an overview of the data modelling procedure.

3.3.1 Specular X-ray reflectivity

XRR is a technique based upon scattering events between X-ray photons and electrons [67, 68]. X-rays incident upon a material cause the electrons within the atomic shells to oscillate at the same frequency as the photon. This electron oscillation acts as a radiation source, emitting an X-ray of identical energy to the incident photon. This elastic process is called Thomson scattering.

In practice, XRR measurement can be explained in terms of reflection and transmission coefficients at the interfaces of materials with differing refractive indices. These coefficients are defined by the Fresnel equations [69] for reflection, r, and transmission, t,

$$\begin{aligned} r &= \frac{n_0\theta_\mathrm{i} - n_1\theta_\mathrm{t}}{n_0\theta_\mathrm{i} + n_1\theta_\mathrm{t}}, \\ t &= \frac{2n_0\theta_\mathrm{i}}{n_0\theta_\mathrm{i} + n_1\theta_\mathrm{t}}. \end{aligned} \tag{3.1}$$

where $n_{0(1)}$ is the refractive index of the incoming (outgoing) medium and $\theta_{\mathrm{i(t)}}$ is the angle of the incident (transmitted) beam. The small angle approximation ($\sin(\theta) = \theta$) has been employed within equation 3.1. The measured intensity of the reflected and transmitted beams is $|r|^2$ and $|t|^2$ respectively. These equations are valid for the reflection/transmission at a single interface, however, multiple interfaces need to be considered for real samples. For example, a single layer thin film has two interfaces, namely air/film and film/substrate. The total reflected intensity is a sum of the initial reflection, together with additional reflections of the initially transmitted wave, as shown in figure 3.4. Using the method proposed by Als-Nielsen [70, 71], the total reflectivity, r_total, from a single layer is given by,

$$r_\mathrm{total} = \frac{r_{01} + r_{12}p^2}{1 + r_{01}r_{12}p^2}, \tag{3.2}$$

where $p^2 = \exp(iqd_1)$ and $q = 2k_1\sin(\theta_1)$. The term p represents a phase factor accounting for the path difference and k_1 represents the incident wavevector.

Equation 3.2 is valid for a single layer only, however, it can be generalised for any two distinct layers,

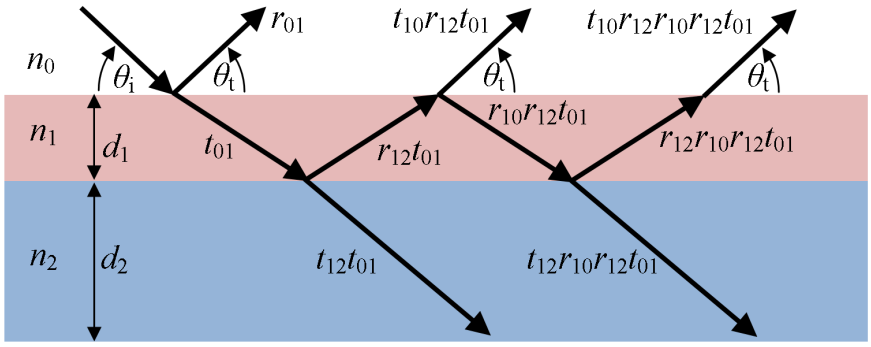

Figure 3.4: Visualisation of the multiple reflected and transmitted X-ray paths within a single layer film. In a typical model, the substrate (blue area, index 2) is assumed to be infinitely thick and no reflections occur from the lower substrate interface.

$$r_{n,n+1} = \frac{r_{n,n+1} + r_{n+1,n+2}p_{n+1}^2}{1 + r_{n,n+1}r_{n+1,n+2}p_{n+1}^2}, \tag{3.3}$$

where each individual layer is represented by the subscript n. Finally, Paratt's recursive method can be followed in order to determine the total reflectivity from a multi-layered thin film [72]. This method first computes the reflection at the lowest interface before stepping through each film interface until the total reflection at the film surface is known, with further details in the following section.

Figure 3.5 shows example specular reflectivity profiles for two film structures. For the blank Si wafer, no transmission exists below the critical angle of 0.5°, while above the critical angle the curve is proportional to θ_i^{-4}. For the sample with a 10 nm thick layer of Pt, the critical angle is now 1.3° due to the change in refractive index of the surface material. Additionally, fringes are observed within the reflectivity profile [73]. These Kiessig fringes are a result of constructive and destructive interference between the differing reflected waves shown in figure 3.4. The constructive interference follows Bragg's law,

$$2d\sin(\theta_i) = n\lambda, \tag{3.4}$$

where n is an integer and λ is the X-ray wavelength. By measuring the difference in Kiessig fringe spacing in figure 3.5, the film thickness can be measured,

$$\sin(\theta_{i,m+1}) - \sin(\theta_{i,m}) = \frac{\lambda}{2d}. \tag{3.5}$$

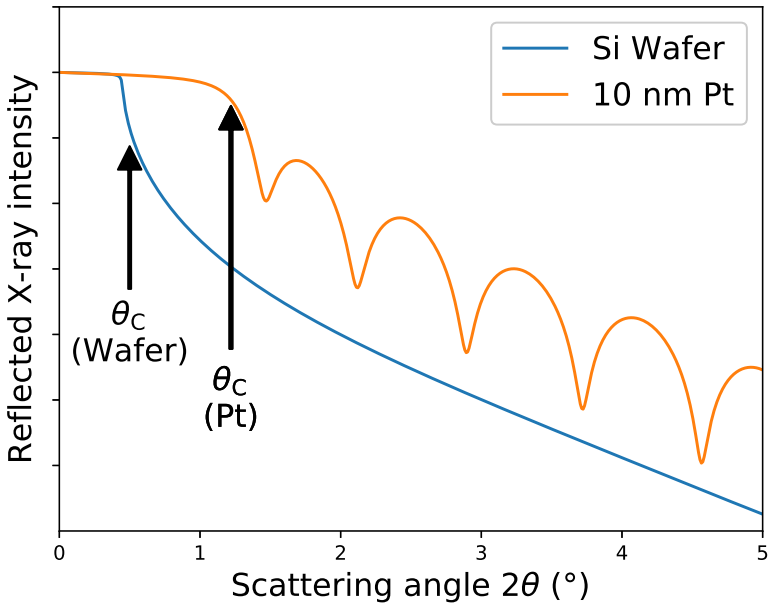

Figure 3.5: Simulated XRR profiles for a Si wafer and a 10 nm Pt thin film. The critical edge (θ_c) has been identified for both profiles.

where $\theta_{i,m}$ represents the incident angle of Kiessig fringe m. This result is valid in the absence of multiple reflections, yet is only an approximation for multi-layered thin films. XRR measurements are often presented as a function of 2θ, where θ is equal to both the incoming and outgoing beam angles ($\theta = \theta_i = \theta_r$).

3.3.2 Rough interfaces and off-specular X-ray reflectivity

The previous section describes the reflection from perfectly sharp interfaces only. In reality, all interfaces are imperfect and can be characterised by an interface width, σ. While specular XRR can determine the overall interface width, it cannot distinguish between interface roughness and intermixing. This section first describes the scattering from rough interfaces, before detailing off-specular measurements.

Figure 3.6 shows the difference between interface roughness and intermixing. Both interfaces can be modeled by a series of intermediate layers, each perfectly flat, where the chemical gradient is described by a Gaussian distribution of width σ. If the intermediate layer thickness is chosen to be much lower than the overall interface width, the total interface reflectivity is calculated by integrating the reflectivity of each intermediate layer over the full interface width. This discretisation can be extended to the full film, as shown in figure 3.7. The inclusion of a finite interface

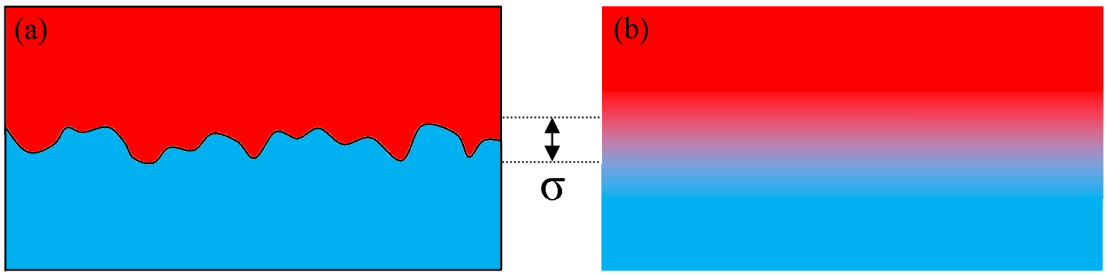

Figure 3.6: Schematic of the interfacial roughness (a) and intermixing (b) contributions to the overall interface width. The chemical gradient across the interface can be represented by a Gaussian distribution in both cases.

width results in a Debye-Waller-like factor for the interface reflectivity, such that,

$$R_{\text{rough}} = R_{\text{smooth}} \exp(-q^2\sigma^2), \tag{3.6}$$

where $q = 2k_1 \sin(\theta_1)$.

To distinguish between interface roughness and intermixing, off-specular XRR measurements are required. Typically, off-specular scans are performed by fixing the angle between the X-ray source and detector ($\theta_i + \theta_r = \text{constant}$) while rocking the sample angle, hence, off-specular measurements are often termed rocking curve

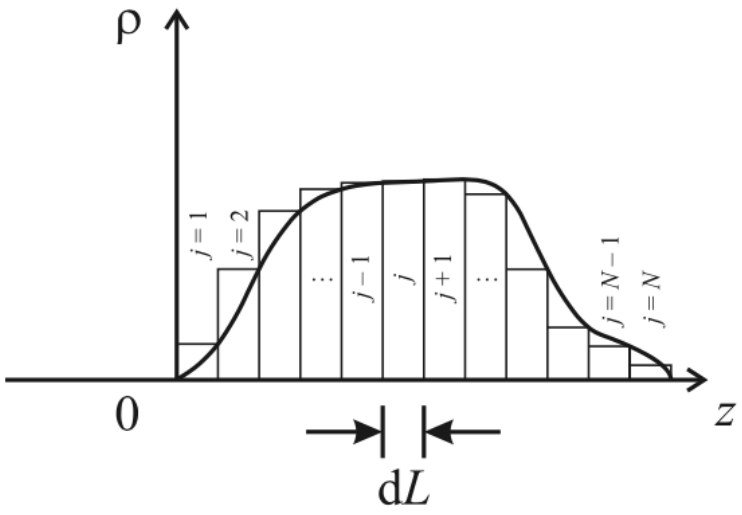

Figure 3.7: Example discretisation of a non-uniform film density profile (ρ) as a function of sample depth (z). Using Paratt's recursive method, the reflectivity is first calculated at the lower $j = 1$ interface, before iterating through each $j + 1$ interface.

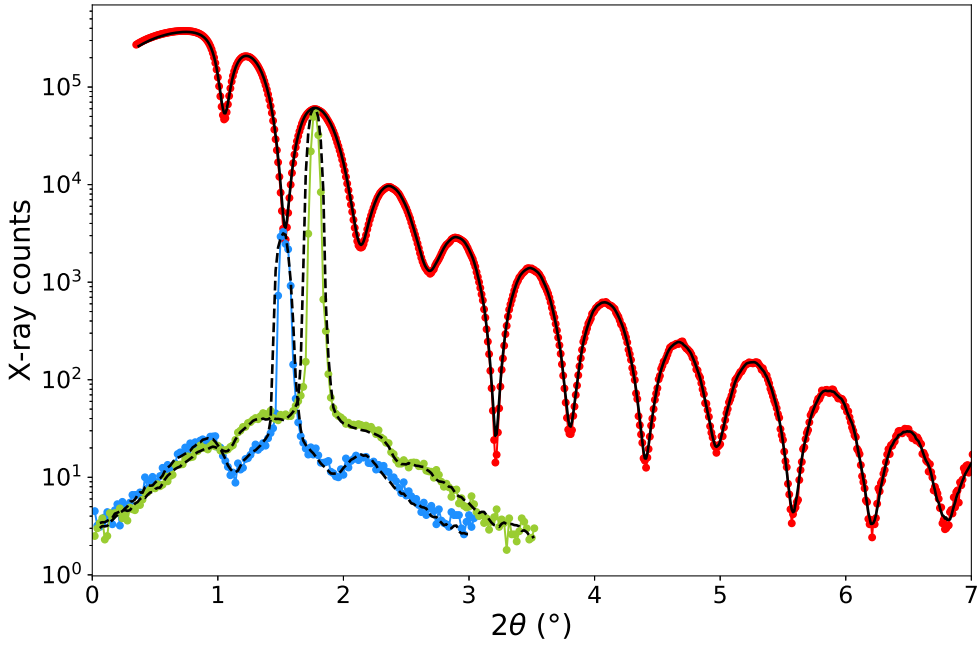

Figure 3.8: Example transverse diffuse scattering measurements (blue and green) together with the associated specular reflectivity (red) for a Pt(3 nm)/CoFeTaB(10 nm)/Ir(3 nm) sample. The transverse scans have been projected onto the 2θ axis for clarity. Dashed lines represent the best fits for the associated data.

measurements within the literature. As the incident and outgoing angles now differ, the resultant intensity at the detector is a result of diffuse scatter at the interfaces. The resultant reflectivity profile can be modelled based on the distorted-wave Born approximation, first developed by Sinha *et al.* [74] before being further developed by Wormington [75]. Example rocking curve data are shown in figure 3.8 for a Pt(3 nm)/CoFeTaB(10 nm)/Ir(3 nm) sample along with the associated specular reflectivity. Within the rocking curve measurements, Yoneda wings occur which produce reflectivity enhancements either side of the specular peak. For the blue data points, the Yoneda wings occur at 1.0° and 2.2°. The position is determined by the critical angle of the film, $\theta_c = 1.0°$, where the Yoneda wing at 1.0° (2.2°) occurs when the incident (outgoing) beam angle is equal to the critical angle.

3.3.3 Polarised neutron reflectivity

Neutron reflectometry differs from X-ray reflectometry in the sense that the neutron interacts with the nucleus of the atom rather than the electron cloud. This allows

for the neutron to also probe the magnetisation of the atom as well as the structure. Magnetic sensitivity is achieved due to the neutron spin interacting with the local magnetic flux density of the atom. Probing the magnetisation is also possible with X-rays, however, there is a requirement for the X-ray energy to be on resonance with a magnetically split transition. Hence, magnetically sensitive X-ray measurements are performed at synchrotron facilities rather than with the use of laboratory based sources.

As neutrons scatter from atomic nuclei, the scattering length factors differ to those for X-ray scattering. The depth-dependent scattering potential, V, for the neutron is given by,

$$V = \frac{2\pi\hbar^2}{m_{\mathrm{n}}}[b_{\mathrm{i,nuc}}(r - r_i) \pm b_{\mathrm{i,mag}}(r - r_i)], \tag{3.7}$$

where $b_{\mathrm{i,nuc}}$ is the nuclear (structural) scattering length factor, $b_{\mathrm{i,mag}}$ is the magnetic scattering length factor and r_i is the position of the i-th atom. The presence of the $\pm$ sign represents the difference in potential observed when the neutron spin is aligned parallel or antiparallel to the atomic moment.

Using the Born approximation, the total reflectivity, R, as a function of the scattering vector, Q, is given by,

$$R(Q) = \frac{16\pi}{Q^2}|\rho(Q)|^2, \tag{3.8}$$

where $\rho(Q)$ is the average scattering length density profile and Q is defined as,

$$Q = k_i - k_f = \frac{4\pi\sin(\theta)}{\lambda}. \tag{3.9}$$

The scattering length density, $\rho(Q)$, is the one dimensional Fourier transform of the scattering length density as a function of position, $\rho(z)$, such that,

$$\rho(Q) = \int_{-\infty}^{\infty} \rho(z)\exp(iQz)dz. \tag{3.10}$$

where the scattering length density, $\rho(z) = \sum N_i(z)b_i(z)$, is the product of the local atomic number density, N_i, and local total scattering length, $b_i = b_{i,\mathrm{nuc}} \pm b_{i,\mathrm{mag}}$. For thicker layers, the reflectivity can be approximated by,

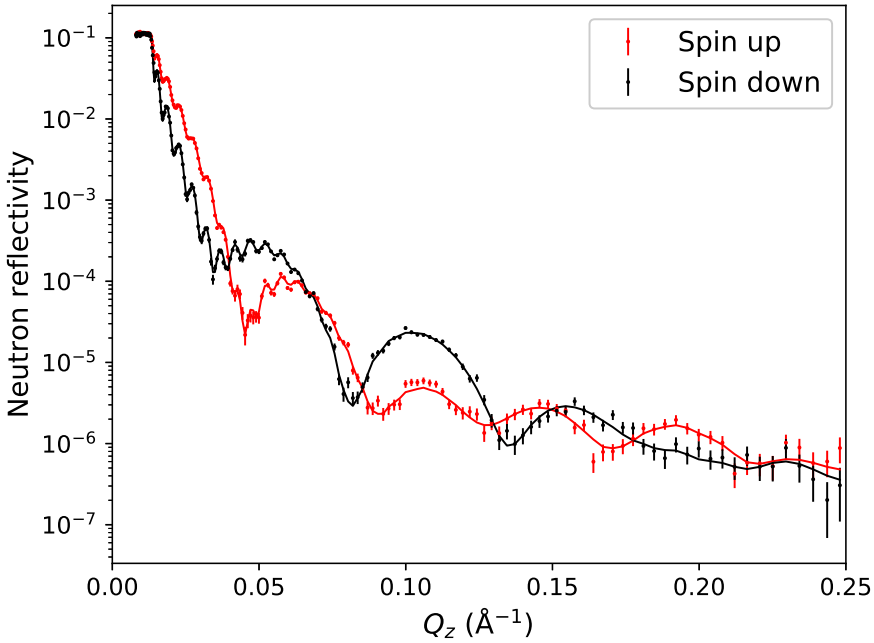

Figure 3.9: Example PNR measurements on a Pt(3 nm)/CoFeTaB(10 nm)/Ir(3 nm) sample. A DC external magnetic field is applied to the sample while the spin polarity of the neutrons is reversed between measurements. The reflectivity profile for spin up and down neutrons is not identical, hence, $b_{\text{mag}} \neq 0$.

$$R = \frac{16\pi^2}{Q^4}(N(b_{\text{nuc}} \pm b_{\text{mag}}))^2, \tag{3.11}$$

where N is this atomic number density. In practice, PNR is modelled much the same as XRR. The discussion of the reflection/transmission at the film interfaces for both specular and off-specular XRR in the previous sections also apply to PNR. Reflectivity profiles for PNR include a critical angle, analogous to the XRR critical angle, where complete reflection is observed below such angle. Above the critical angle, PNR also displays Kiessig fringes.

The key difference for PNR over laboratory based XRR is the variation in the reflectivity due to the magnetic scattering length factor (equation 3.11). By changing the sign of this interaction, through the reversal of the atomic moment or neutron spin polarity, two unique reflectivity values are obtained. An example measurement is shown in figure 3.9, where the reflectivity contrast is obtained by reversing the polarity of the neutron spin while keeping the magnetic moments within the film constant with the use of a DC guide magnetic field.

3.3.4 Experimental technique for X-ray reflectivity

All XRR measurements within this thesis were obtained with the use of a Bede D1 Diffractometer. A schematic of the instrument is shown in figure 3.10. The instrument produces X-rays with a wavelength of 1.54 Å using the Cu-Kα_1 spectral line. Isolation of this spectral line is achieved with the use of a double bounce channel cut silicon crystal. The X-rays are collimated by a pair of 0.5 mm $\times$ 15 mm slits. The sample stage has six degrees of freedom, namely linear motion along the three Cartesian axes as well as rotation in all three planes. The detector arm includes a second pair of collimating slits immediately prior to the detector.

Specular XRR measurements are performed by keeping the incident and reflected beam angles equal. First, the sample as aligned to the beam such that it is flat with respect to the beam profile and is at the beam centre. Due to the 0.5 mm $\times$ 15 mm slit size, the beam profile is approximately rectangular. Scans are performed of each axis in order to ensure the sample surface is flat with respect to the long axis of the beam envelope. During alignment of the sample a *half-cut* is performed, where the intensity as measured when the detector and sample are at 0° is half that when the sample is removed. This ensures that the surface of the sample is in the centre of the short axis of the envelope. The sample angle is defined as θ and the detector

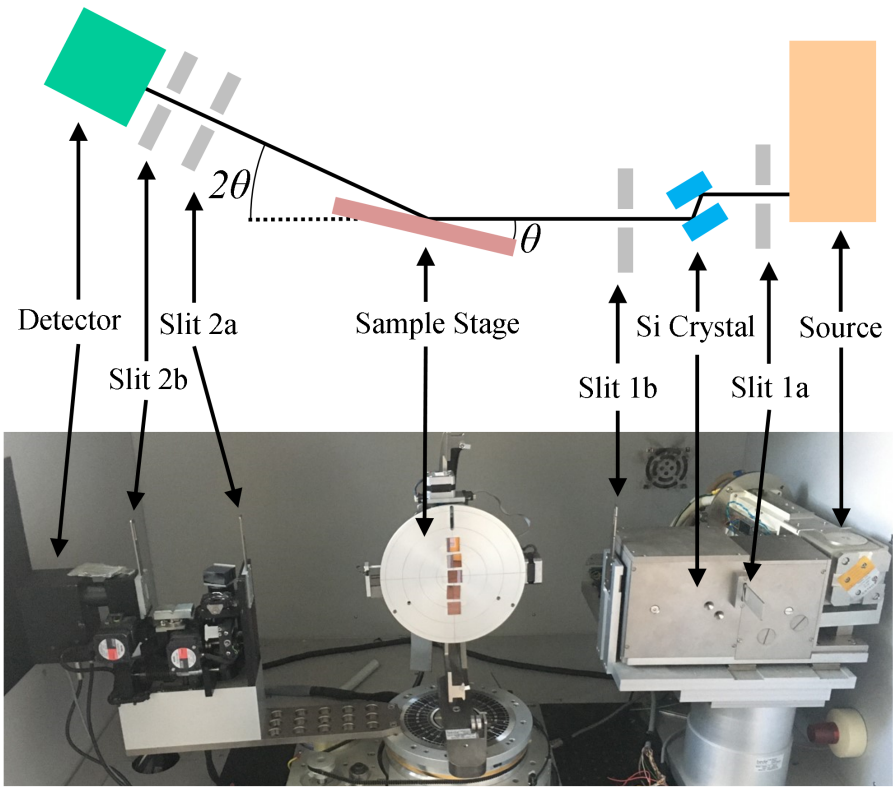

Figure 3.10: Schematic and photograph of the Bede D1 Diffractometer.

angle is 2θ. Typical XRR measurements involve scanning 2θ in the range of 0° to 10° with step sizes of 0.01°.

3.3.5 Experimental technique for polarised neutron reflectivity

The PNR measurements reported in this thesis were obtained on the PolRef beamline at the ISIS neutron source, England. This facility uses a pulsed proton beam to initiate a spallation reaction within a tungsten target. A spallation reaction describes the violent process of high energy incident particles breaking a target atom into various particles such as protons, neutrons and α-particles. Immediately after a spallation event, the emitted neutrons carry too much kinetic (thermal) energy and must elastically scatter from a moderator. Once the energy has been reduced, the neutrons can be used for scientific purposes.

The neutrons produced at spallation sources vary in energy and, hence, their de Broglie wavelength $\lambda = h/m_{\mathrm{n}}v$. As such, the PolRef beamline uses neutrons within the wavelength range of 0.5 Å $-$ 6.5 Å. Whereas XRR measurements obtain reflectivity profiles by fixing the X-ray wavelength and varying the incident angle, time of flight neutron beamlines, such as PolRef, measure reflectivity profiles through fixed angles and varying neutron wavelengths. As a result of this, the reflectivity profiles are often presented as a function of Q_z, as opposed to θ.

The general beamline layout is presented in figure 3.11, including an image of the experimental hutch. The beamline is 2.3° below the horizontal in order to reduce the background noise from fast neutrons and X-rays direct from the moderator. The neutrons first pass through a chopper in order to define the neutron pulse edges. If timed incorrectly, the fast neutrons of one pulse may catch up to the slow neutrons of the previous bunch and create false results. The polariser then defines the beam polarisation in the spin up direction. If spin down neutrons are required, the polariser still defines spin up neutrons, however, the spin flip mirror is activated such that the neutron spin is reversed.

Between the point of neutron polarisation and the sample stage, a continuous guide field is required in order to maintain the neutron polarisation. The sample stage includes an electromagnet which produces a horizontal magnetic field transverse to the neutron beam direction which saturates the magnetisation of the sample. As all samples used within this thesis are fully saturated within the applied field of 100 Oe, spin flip measurements are excluded. Instead, the polarisation of the neutron post sample reflection is neglected. At multiple stages along the beam path, slits of various sizes are included to maintain the resolution. Due to effects such as

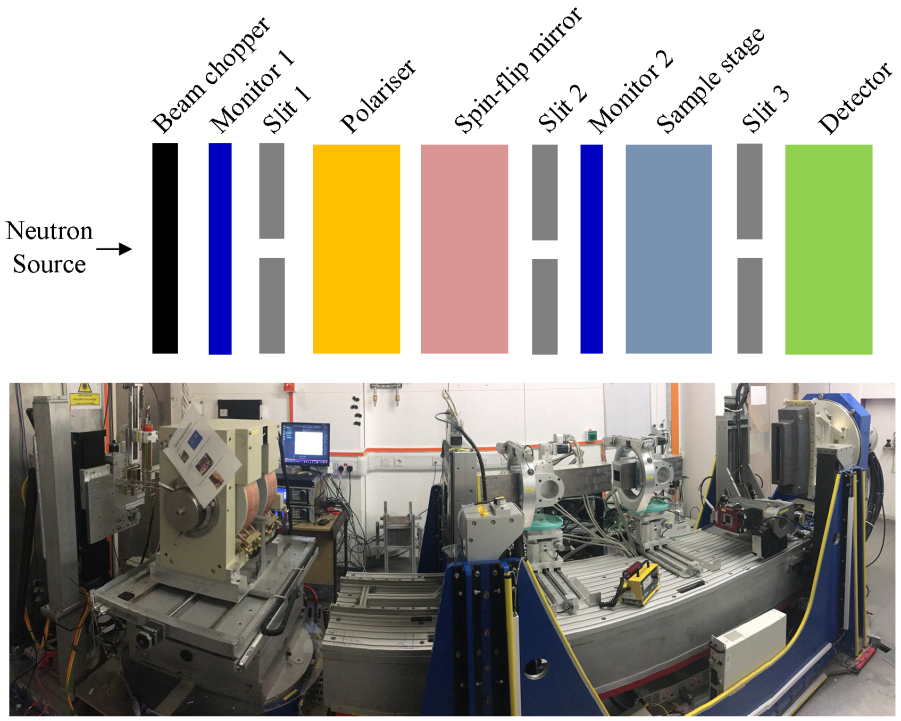

Figure 3.11: Simplified PolRef beamline schematic along with a photograph of the experimental hutch. The experimental hutch contains all components from slit 2 (left of image) up to the detector (right of image).

gravity, the opening within the slits generally increases in size when further away from the source due to the increased fast and slow neutron spread. Two monitors are included within the beamline. The differences observed between monitor one and two define the polarisation efficiency of the neutron beam. The signal at the detector is normalised to monitor 2.

3.3.6 Data modelling

The procedure for modeling XRR and PNR data is identical, with differences only occurring within the parameters defining the model. An open source program, GenX, was used to optimise the model for each data set. The PhD thesis of Inyang provides an in-depth methodology for the fitting procedure [76], which is identical to that used within this thesis and is summarised below.

An initial model is constructed using the nominal structural information. The input parameters can be separated into three broad categories depending on how they are initially defined. First, material parameters such as the density and scattering factors are set to literature values. Instrument parameters, such as the beam width and sample size can be measured. Finally, sample parameters such as the film

thickness and interface width can be set to their nominal values. The parameter's category broadly dictates the range over which the associated parameters may vary. Measured values, such as sample length and incident X-ray intensity should not vary by any significant amount and have been limited to ± 5 % within this thesis. Literature values, such as density and scattering factors, may vary due to differing growth conditions. For example, it is known that the density of Pt varies depending upon the seed layer to which it is grown. Parameters within this category have been limited to approximately ± 10 %. Finally, layer thicknesses and interface roughness values can vary substantially due to factors including growth rate calibration errors. As such, the parameters can vary by more than ± 50 % in extreme cases.

After the initial model has been optimised, the result is visually inspected for accuracy. Further models are then postulated, which can include intermediate interface layers and surface oxide layers. After further optimisation, these models are compared to the nominal model. If no increase in accuracy is observed, the additional feature is removed, however, if a substantial increase in model accuracy is observed then the additional feature is accepted. This process is repeated until the model reproduces the data in its entirety.

While allowing for a large parameter range when optimising the model and including additional features beyond the nominal structure may be required to find the optimal solution, care must be taken to ensure the result is physical. Reflectivity analysis suffers from the *phase problem*, where the phase information is lost when measuring the reflectivity. In section 3.3.1, it was stated that the measured reflectivity is equal to $|r|^2$. Any phase information contained within r is, therefore, lost when the reflectance is measured. The consequence of this phase loss is that there exists an infinite set of r values, such that $|r|^2$ equals the measured reflectivity. In reality, this means that the quality of fit cannot be taken as the sole measure of the model accuracy and a visual inspection of the model is required.

Chapter 4

Construction of a magneto-optical Kerr effect instrument

The magneto-optical Kerr effect (MOKE) describes the interaction of polarised light with magnetic media, in particular the change in polarisation upon reflection. This was first witnessed in 1877 by Kerr when observing polarised light reflected from the pole piece of a magnet [77]. He was led to this experiment by the results of Faraday thirty years prior in which the rotated polarisation of light passing through a magnetic medium was observed [78].

Over 140 years later the Kerr effect is heavily utilised for thin film magnetic research [79–81]. The Kerr effect (reflection) is employed more than the Faraday effect (transmission) due to the simple fact that most magnetic materials are opaque and are fabricated on substrates which would cause complications in transmission measurements. Modern MOKE instruments typically involve a linearly polarised laser focused onto a sample. The reflected light is passed through a second polariser which converts any polarisation change into an intensity change which is subsequently measured by a photodiode. These instruments offer simple and high throughput experimental measurements for magnetic hysteresis determination and are commonplace in magnetic material research laboratories.

This chapter details the process of constructing a custom MOKE laser system that is used for the measurements throughout this thesis. First, the options for the various components are discussed including an explanation of the choices for this particular setup. From here, the construction is detailed as well as the sample environments required for low temperature and electrical measurements. Finally, any encountered teething problems are presented along with the solutions before concluding this chapter.

4.1 Background

4.1.1 Theory

The MOKE is well documented in literature through the use of dielectric tensor theory, however, one does not need a full understanding of such theory to build and/or use a MOKE instrument. Instead, the acceptance that the refractive index of magnetic materials is magnetisation and light polarisation-dependent is sufficient. The explanation of why this is true is complex and requires knowledge of dielectric tensor theory, and as such I suggest the works by Qiu [79] and Zak [82] for a deeper and more complete understanding. In summary, the dielectric tensor that describes magnetic materials contains off diagonal elements that include Voigt magneto-optical constants. These constants represent the optical response of a material due to the magnetic moment and are directly proportional to the magnetisation of the material to first order. Magnetic sensitivity within MOKE instruments is, therefore, achieved indirectly through the measurement of the Voigt magneto-optical constants.

By acknowledging that different refractive indices exist depending on the incident light polarisation and the materials magnetisation, MOKE measurements can be explained through circular birefringence and dichroism. First, we assume that linearly polarised light is incident upon a magnetic surface. This linearly polarised light can be broken down into right and left circularly polarised (RCP and LCP) light of equal magnitude and phase. Circular birefringent materials have differing refractive indices for RCP and LCP light and as such these polarisations travel at different speeds within the material. This introduces a phase difference between RCP and LCP light and upon exiting the material, the circularly polarised light can be recombined into linearly polarised light with a rotated angle of polarisation proportional to this phase difference.

To explain the ellipticity of the Kerr reflected light, circular dichroism is required. This property defines the differential absorption of RCP and LCP light. Using the previous example of equal RCP and LCP incident light, the magnetic material preferentially absorbs one polarisation resulting in the magnitude of reflected RCP and LCP light being unequal. When recombined into linearly polarised light, this preferential absorption introduces a polarisation component that is orthogonal and in phase with the original linear polarisation. It is this additional small orthogonal component which produces elliptically polarised light.

4.1.2 Longitudinal, transverse and polar geometries

There exist three geometrical orientations for MOKE instruments which are sensitive to magnetisation lying along each of the standard cartesian x, y, z axes, as depicted in figure 4.1. Throughout this thesis, the MOKE results shown are taken using polar and longitudinal MOKE for out-of-plane and in-plane magnetised samples respectively.

The first geometry to consider is the polar orientation in which the magnetisation lies out of the sample plane and the laser is reflected at normal incidence. To obtain a Kerr rotation, a component of the magnetisation has to lie within the plane of incidence. The plane of incidence is defined as the plane which contains both the incident light wave vector and the vector defining the surface normal. For light at normal incidence these vectors are antiparallel, therefore, there exists an infinite set of planes which contain these vectors and the definition of a singular plane of incidence within this set is arbitrary. No matter the choice of plane within this set, as the magnetisation vector lies within all such planes, a Kerr rotation will always be observed for linearly polarised incident light. The magnitude of such polar Kerr

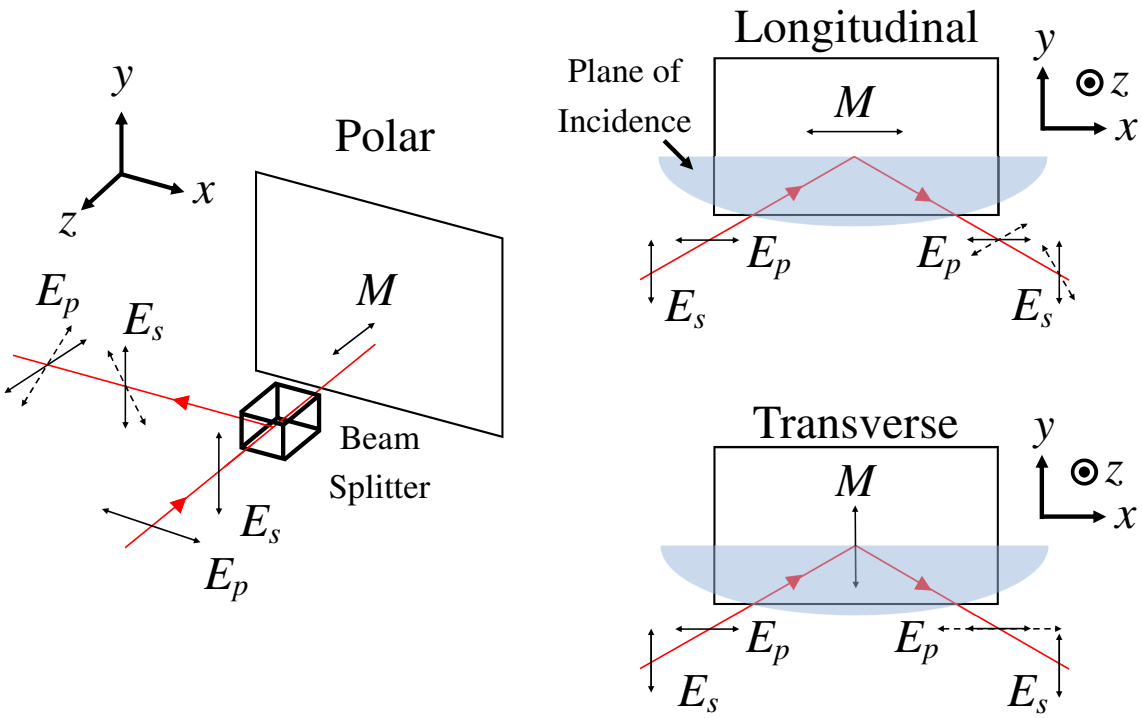

Figure 4.1: The experimental geometries showing both the optical path and the polarisation for three different types of MOKE measurement. Each schematic includes a vector defining the dominant direction of magnetisation sensitivity (M), two axes of incident light polarisation (E_p and E_s) as well as the plane of incidence for longitudinal and transverse setups.

rotation is typically an order of magnitude larger than that observed for in-plane measurements [83]. As the choice of scattering plane is arbitrary, so is the definition of the vector defining the incident light polarisation axis with respect to the sample. Nevertheless, s- and p-polarised light are still shown for the polar geometry in figure 4.1. Both polarisations are linear, with the axis of polarisation for p-polarised light being in the plane of incidence and the axis of s-polarised light being perpendicular to the plane. As polar MOKE has no defined plane of incidence, these were instead chosen to be of identical orientation with respect to the optics bench to that of the longitudinal and transverse geometries, i.e. p-polarised light is parallel to the optics bench surface and s-polarised light is perpendicular to such surface.

The second geometry to consider is the longitudinal orientation which is sensitive to magnetisation lying in both the sample plane and incidence plane. The incident light is typically at 45° to the sample surface, hence defining a singular plane of incidence. As the magnetisation lies within the plane of incidence, a Kerr rotation is observed which is independent of the incident light polarisation direction.

As the criteria for Kerr rotation to occur is to have a component of the magnetisation within the plane of incidence, it is possible to simultaneously measure many Kerr rotations from moments pointing in several directions. If there exists a component of the magnetisation that lies out of the sample plane, this also lies within the plane of incidence of the longitudinal geometry and hence would also produce a Kerr rotation. To avoid this polar Kerr rotation, the incident angle must be 0°, or as close to such angle as is possible to remove or reduce the polar Kerr component respectively. However, grazing incident angles have the negative effect of elongating the laser spot size upon the sample, hence severely reducing the spacial resolution and a compromise is required. Typically, the angle of incidence for in-plane MOKE systems is 45° which has been found to be a good balance of sensitivity against spatial resolution. Although we are equally sensitive to longitudinal and polar Kerr rotation components at this angle, samples that exhibit in-plane magnetisation often require relatively large magnetic fields to induce out-of-plane magnetisation components, therefore, the measurement of a signal comprised of both an in-plane and out-of-plane rotation is highly unlikely at the small magnetic fields used in most MOKE instruments.

The final geometry, which is also sensitive to in-plane magnetisation, is referred to as transverse MOKE. Here, the magnetisation lies perpendicular to the plane of incidence. As no component of the magnetisation lies within the plane of incidence, no Kerr rotation is observed. Instead, an intensity change is observed for p-polarised light. Transverse MOKE is unique in that this intensity change only occurs for p-

polarised light and s-polarised light remains unchanged.

The typical setup for in-plane MOKE measurements is the longitudinal geometry with s-polarised light. To identify why this is the case we must consider a sample with a multi-domain structure, in particular one with both transverse and longitudinally magnetised domains. If we were to use p-polarised light, the reflection would consist of both an intensity change from the transverse domains and a Kerr rotation from the longitudinal domains. As this Kerr rotation is transformed into an intensity variation via an analysing polariser, it is not possible to separate the contributions from longitudinal or transverse domains within a single measurement of the combined intensity variation. This introduces the preference for s-polarised light as the signal is solely comprised of longitudinal domain Kerr reflections since it remains unchanged for transverse magnetisations.

4.1.3 Penetration depth

The MOKE is a surface sensitive technique, limited by the optical penetration depth of light. The penetration depth, λ, is given by,

$$\lambda = \frac{1}{2k\beta}, \tag{4.1}$$

where k is the incident light wavevector and β is a constant representing the absorptive component of the refractive index. At a depth of λ, typically 10 - 20 nm for a metallic thin film [84], the light intensity is reduced by a factor of $1/e$. This depth depends on material choices and is also significantly affected by reflections at interfaces of two distinct layers. At film thicknesses less than λ, the Kerr signal is proportional to both the total magnetic moment and small thickness changes. At thicknesses greater than λ, the Kerr signal is dominated by the moments closer to the surface and any Kerr rotation due to moments at a depth much greater than λ are significantly suppressed. The Kerr signal is also modified by experimental parameters, including, but not limited to, analyser polariser position, the degree of initial polarisation and detector sensitivity. The extraction of absolute magnetic moments is, therefore, not trivial, hence MOKE measurements are almost always presented with dimensionless Kerr signal scaling.

4.2 Design

A typical MOKE effect instrument is very simple and consists of a stable, linearly polarised laser incident upon a sample in one of the aforementioned MOKE geometries. The reflected laser is passed through a polariser, converting any polarisation rotation into an intensity variation which is subsequently measured through the use of a photodiode. A magnetic field is applied to the sample and the change in laser beam intensity is measured as a function of such applied magnetic fields. A more in-depth description is given in section 4.3.1, which details the chosen experimental setup after component determination, including a schematic diagram, although no information from section 4.3.1 is required to understand this section.

This section serves to describe the available equipment options when building a MOKE measurement system. Each section discusses the important characteristics in the various electrical components, including comparisons between the different types of available electronics where appropriate. This is not an exhaustive list, however, it aims to cover the equipment needed for a typical MOKE setup. It is important to note that the system must be considered as a whole rather than each component in isolation. For example, the choice of detector will determine the amplitude of the Kerr signal photocurrent which will in turn dictate the requirements for the amplifier gain and voltage measurement device. The section concludes by summarising the available options and stating the chosen components for this particular MOKE system build.

4.2.1 Oscilloscopes vs. data acquisition cards

There are many ways in which the measurement of voltage signals can be automated, including through the use of multimeters, oscilloscopes and data acquisition (DAQ) cards. DAQ cards are contained within the computer housing and plug directly into the computer motherboard. There are costs and benefits to all methods, for example, the vast majority of multimeters do not perform well when logging the form of AC signals, yet their precision is often higher than other devices for DC signals. The two methods most appropriate for MOKE systems are oscilloscopes and DAQ cards. Here, these will be discussed through the use of two example devices, a Tektronix TBS1064 oscilloscope [85] and a National Instruments PCIe-6351 DAQ card [86], both retailing for approximately £1100 at the time of writing. Although these devices would suffice for a MOKE instrument, they were not chosen as the best devices currently on the market for a MOKE instrument, but rather to serve as an example comparison for the typical devices on offer.

	Oscilloscope Tektronix TBS1064	DAQ Card National Instruments PCIe-6351
Analogue Input Channels	4	8
Separate Trigger Input	Yes	Yes
Input Sampling Rate	1 GS/s	1 MS/s
Input Range Options	From 2 mV to 5 V/div	From ± 0.1 V to ± 10 V
Input Resolution	8 bits	16 bits
Analogue Outputs	0	2
Output Sample Rate	n/a	2 MS/s
Output Resolution	n/a	16 bits

Table 4.1: Comparison of two example measurement devices for MOKE instruments. A summarised specification showing items of particular relevance to the application of MOKE instruments is presented, with further details available through Tektronix [85] and National Instruments [86].

Firstly, it is worth defining the exact requirements for our particular MOKE measurement system. The minimum number of channels required is two data (Kerr signal, applied field) plus one trigger signal. On top of this, extra signals such as those for sample Hall voltages, monitoring the magnitude of current applied through the sample and temperature sensors for cryostats will be required on a case by case basis. In terms of sampling rate, a typical MOKE measurement involves an oscillating applied field on the order of 10 Hz. To gain a suitable number of data points per hysteresis loop, a sampling rate greater than 20 kHz is required (resulting in 2000 data points per hysteresis loop). For voltage resolution, the expected minimum Kerr signal is on the order of 1 % of the light intensity (the calculations for which are detailed in the following section 4.2.2). In light of these three requirements, the summarised specifications of the example oscilloscope and DAQ card options are shown in table 4.1.

Oscilloscopes are commonplace in laboratories and are typically either two or four channel devices. The intended customer for oscilloscopes has driven manufacturers to develop devices with extremely high sampling rates for the purposes of measuring very high frequency AC signals, which has resulted in oscilloscopes with sampling rates on the order of 1 GS/s being the norm for most entry level devices. There exists DAQ cards designed for direct oscilloscope replacements which can compete with these high sampling rates, however, these will not be discussed here as they are not the most applicable DAQ device for MOKE instruments. Instead, the DAQ device chosen for comparison falls under the category of multifunction I/O (Input/Output) devices due to its analogue input, analogue output and digital channels. These

devices are not aimed at high frequency AC signals, therefore, the sampling rates are typically on the order of MS/s, three orders of magnitude lower than the presented oscilloscope, yet still well above the requirements of our MOKE system.

Instrument resolution is defined in terms of bits, or rather the total number of levels when converting an analogue signal to digital. The presented oscilloscope has a vertical resolution of 8 bits, therefore, there exists 256 (2^8) possible levels to a measurement of an analogue voltage signal. In terms of a percentage value, this equates to each voltage level being 0.39 % of the maximum range (e.g. for a range of 0 - 2 mV, the only possible digital measurements are 0 μV, 7.8 μV, 15.6 μV, 23.4 μV etc.). A higher resolution simply reduces the spacing of such levels, for example the 16 bit resolution of the presented DAQ device equates to levels separated by 0.0015 % of the maximum range. Returning to the requirement of measuring a 1 % Kerr signal, it is clear that the oscilloscope only just meets this criteria compared to the DAQ card which comfortably satisfies this requirement. The presented 1 % requirement represents a 1 % signal change between positive and negative magnetic saturation, therefore, any features within the measured hysteresis loop would then not be visible in the oscilloscope measurement due to the lack of sensitivity. Due to the much higher resolution, these features would be visible when using the presented DAQ card. It is worth reminding the reader at this point that oscilloscopes with higher resolutions are available and that the presented oscilloscope was chosen merely as a typical entry level unit, however, the resolutions are typically lower than that of an equivalently priced multifunction I/O DAQ card.

As previously stated, the most appropriate DAQ card is a multifunction I/O card as opposed to a oscilloscope card. This is partly due to the inclusion of a small number of analogue output channels. Electromagnets are typically powered by high current amplifiers controlled by arbitrary function generators. These two devices can be separate units or combined. If using an oscilloscope, an arbitrary waveform generator is required for the measurement. For multifunction I/O cards, this arbitrary waveform can be produced through the included analogue output channels. This removes the requirement of an external arbitrary waveform generator, hence reducing the complexity and total cost of the system. These analogue outputs can also be used to power small components such as Hall probes, further reducing the requirements for additional system components when compared to measurements involving oscilloscopes.

Up to this point, one may be in favour of multifunction DAQ cards after the previous comparison, however, there are features that are hard to quantify which may counter this. One example is that oscilloscopes offer a physical user interface

complete with a real time signal display, allowing for minimal user training time due to its intuitive operation. On the contrary, DAQ cards offer no physical user interface but rather it is controlled through software. In most cases, the basic proprietary software is almost always less intuitive or versatile than the oscilloscopes physical user interface to the average user. Instead, this software is often intended for use when creating larger instrument control programs, such as through LabVIEW or a custom Python program, at which point the user experience can be made equivalent to or improved upon that of oscilloscopes.

4.2.2 Laser power and detectors

The analysis of the optical path for MOKE systems can be complex or simple, depending on the intended application. It is advisable to perform a full quantitative MOKE analysis if this application requires a high sensitivity for applications such as single shot nanowire detection. Allwood et al. provide an example in-depth calculation for signal to noise determination from various noise sources for such applications, if this is required [87]. In contrast, MOKE systems intended for more generic thin film use or patterned structures with larger dimensions (of comparable to or greater than the focused laser spot size), as is the case for this particular instrument, require a less sophisticated analysis.

Here, the expected smallest feature that the MOKE system should be capable of measuring is a single structure of 10s of micron dimensions or arrays of 1-10 micron sized elements. Therefore, only a basic characterisation is necessary and is presented here. Table 4.2 shows approximate optical transmission values for elements in a typical polar MOKE setup, which is detailed later in chapter 4.3.1, figure 4.3. These values have been derived from Jones calculus which describes the propagation of linearly polarised light through optical elements. The polarisation of light can be described by a two dimensional vector with axes orthogonal to each other as well as the direction of propagation. All optical elements are then described by a 2×2 matrix, which when multiplied with the vector, produces the polarisation vector for the transmitted light. This multiplication can be performed in series for all optical elements in the beam path to produce the final transmission value, as shown in table 4.2. Optical elements with unity transmission, such as focusing lenses, have been omitted from the table. The values will include some variance in practice, therefore, the values presented are intended for an approximate calculation only. For example, diode lasers are typically partially polarised hence alignment of the dominant polarisation axis with the initial polariser can achieve a transmission value greater than 0.5. Other values such as the iris and sample reflectivity are highly

Optical Element	Fibre Optic	Beam Splitter	Polariser	Iris	Beam Splitter	Sample Reflectivity	Beam Splitter	Analysing Polariser	**Total**
Transmission	0.5	0.5	0.5	0.1	0.5	0.5	0.5	0.005	**8e-6**

Table 4.2: The approximate transmission ratios for the optical components present in a typical polar MOKE setup.

measurement dependent, however, the values used here are typical values attained from previously performed measurements.

This short analysis shows that the laser intensity is reduced by over five orders of magnitude from source to detector. One may think the logical solution is to use a high power source, however, it is not as simple as considering the power at the source and detector. Any amount of light incident upon the sample is partially absorbed resulting in a small temperature increase. If the incident light is of too high power then this temperature can become significant. Higher powered lasers also have increased costs, including both the initial purchase and the implementation of extended safety measures to satisfy the associated regulatory requirements. These include system enclosures and interlocks for class 3B/4 lasers, which are not required for class 3R lasers. It is therefore typical of continuous wave MOKE systems to have source intensities in the region of a few mW to remain within the 3R classification. Here, we have chosen a 7.5 mW diode laser of centre wavelength 658 nm (Thorlabs LPS-660-FC [88]). This laser has a power at sample of 50 μW, relating to a power density of approximately 16 W cm^{-2} when focused, which is low enough to be considered negligible in terms of sample heating or other laser induced effects. Using the heat capacity of the silicon wafer as an approximation (due to the volume of the wafer dominating the volume of the sample), the temperature rise is calculated to be between 6×10^{-4} and 0.5 K/s. These values use the full wafer size (10 mm $\times$ 10 mm $\times$ 0.5 mm) and a 0.125 mm^3 region respectively. In reality, the thin film is in good thermal contact with the silicon wafer, which is also in good thermal contact with the sample holder. Hence, an equilibrium state will be quickly reached without any excessive elevated temperatures.

Turning our attention to the detector, the total optical transmission of 8 $\times 10^{-6}$ means that approximately 60 nW is incident upon the detector. A laser line filter is often used immediately before the detector to filter out unwanted light sources such as room lights and computer screens. For simplicity, we will assume 100 %

of the incident light passes through any such filter and lies fully within the active area of the photodiode. To convert this power to a photocurrent, the responsivity of the photodiode is required. Choosing a typical photodiode available at the time of writing (thorlabs FD11A Si photodiode [89]), the associated responsivity of 0.42 A/W at 658 nm results in a photocurrent of 27 nA. Due to the low current used, any attempt to measure the current directly would require specialist ammeters, hence increasing the cost of the system (such as Keithley series 6400 Picoammeters, starting at £2,200 at present). Instead, the common alternative is to use amplifiers which are often cheaper, such as the Melles Griot 13AMP003 large dynamic range amplifier. This amplifier has a gain of 10^7 V/A, therefore, producing an output of 0.27 V for a photocurrent of 27 nA.

So far we have only considered the total light through the optical system resulting in a signal of 0.27 V. This analysis does not include any intensity changes due to Kerr rotations, which we can now consider. If we assume a Kerr rotation of 0.02°, which is typical of ferromagnetic layers [90, 91], we can calculate a new system transmission value through changing the analysing polariser angle. Previously, this was set to 4°, however, now setting this to 4.02° and repeating the previous Jones matrix calculations results in a transmission increase of approximately 8×10^{-8} upon the base transmission of 8×10^{-6}. Following the same photodiode and amplifier calculations, this results in a photocurrent of 0.27 nA and an amplified signal of 2.7 mV.

It is now clear why only a simplified analysis is required for this setup. From this calculation we expect a 2.7 mV Kerr signal upon a 270 mV signal background, which is well within the input ranges of both oscilloscope and DAQ devices. A secondary benefit of this large dynamic range amplifier is the ability to apply a DC offset to the signal. For example, applying a -260 mV DC offset would then mean there exists a 2.7 mV Kerr signal upon a 10 mV background. Instead of measuring a 1 % signal change, there is now a 27 % signal change which has implications for the measurement resolution. In the previous section, the example oscilloscope had a resolution of 0.39 % which was too low to resolve any features within a hysteresis loop with a magnitude of 1 %. Now that such a hysteresis loop is of 27 % in magnitude, this 0.39 % resolution is now sufficient to resolve such inner features.

4.2.3 Lock-in amplifiers

In the previous section, amplification of the photocurrent was achieved through the use of a DC amplifier. Another solution is to use a lock-in amplifier, although this requires some form of AC modulation. This is often achieved through the use of a

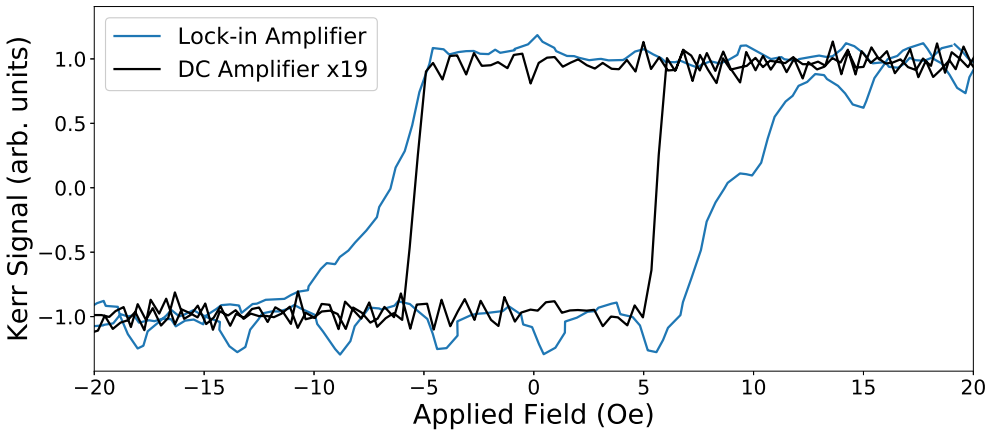

Figure 4.2: Longitudinal MOKE measurements of a reference sample comparing different measurement electronics, namely a DC wide bandwidth amplifier (black) and a lock-in amplifier (blue). Measurements were performed under identical sample conditions.

beam chopper or by the modulation of the laser diode current. Figure 4.2 shows two measurements under the same sample conditions, with one using the DC amplifier introduced previously and a second using a lock-in amplifier. The modulation used here is of 2 kHz frequency and is achieved by modulating the laser diode current by approximately 5 %. Both measurements have been normalised for clarity, yet the data produced from the DC amplifier is a factor of 19 smaller than that of the lock-in amplifier. The greater sensitivity of the lock-in amplifier does come at a cost, which is clearly demonstrated by the shape of both curves.

A lock-in amplifier works by multiplying the signal by a reference frequency and time averaging the result over a period of time much longer than the period of the reference frequency. If the frequency of the signal matches that of the reference, and there exists a constant phase difference between the signal and reference waveforms, then the time average of the product is non-zero. If there is a frequency mismatch, the time average will be zero, assuming a long enough period over which this time average is performed. It is this time averaging period which causes the broadening of the sharp magnetic reversal demonstrated in figure 4.2. The magnetism within the sample reverses over a time period of less than 1 ms (determined from the DC amplifier data), yet the lock-in amplifier time averages a longer period of 25 ms for this measurement. This time period is dictated by the modulation frequency and must be greater than the period of such modulation, which is 0.5 ms for this measurement. Therefore, 10 ms after magnetic reversal, the system is effectively time averaging two states, 10 ms of post reversal Kerr signal and 15 ms and pre

reversal Kerr signal. It is possible to reduce this broadening effect by reducing the time averaging period, yet to achieve the same signal to noise ratio when doing so the modulation frequency must be increased. This frequency increase is hard to reliably achieve beyond the kHz range with our setup and is, therefore, impractical. For the use of faster modulation speeds, beam chopper assemblies are unsuitable as they are commonly used for frequencies of up to 10's of kHz, yet are difficult to stabilise beyond this range. Laser intensity modulation at frequencies on the order of MHz is possible, yet require specialist components which are generally only available on laser sources of increased cost. The same effect can also be achieved by slowing down the measurement frequency, which was 1.6 Hz for figure 4.2. Although this can be achieved with ease, any time benefit gained from the increased signal to noise ratio when using a lock-in amplifier is negated by such reduction in the measurement frequency. It is because of these reasons that a DC amplifier was chosen in place of a lock-in amplifier for the instrument used for the work throughout this thesis.

4.2.4 Equipment choices and conclusions

In conclusion, it was determined that the best measurement devices for our system were two analogue output and input DAQ cards, National Instruments PCI-6713 and PCI-6034E respectively. They were chosen over the use of an oscilloscope due to their versatility when creating a multi-purpose MOKE system. These cards exceed the design specification for this system while also offering room for expansion through the use of extra channels and higher sampling rates. A 7.5 mW red laser was chosen, complete with temperature and current controllers. These controllers allow for the stable laser power output required for measurements with little to no averaging required. The power stability of the laser was better than 0.02 % over a typical measurement time of one minute. The polarisers used were Glan-Taylor calcite crystals with extinction ratios better than 100000:1. Finally, a Melles Griot 13AMP003 amplifier was used along with a pre-owned silicon photodiode of unknown manufacturer.

This instrument achieves the goal of being a highly sensitive MOKE system while remaining a relatively inexpensive setup. There are many variations to MOKE instruments, each with their respective pros and cons. One of the advantages of these many variations is the possibility for instruments to be built around pre-existing parts, for example, the detector arrangement, magnet power supply and some of the other components used here were repurposed from existing instruments. MOKE instruments can, and should, be tailored to their applications and are a highly useful tool for thin film magnetism research.

4.3 Experimental setup

4.3.1 Polar and longitudinal experimental setup

This MOKE instrument is designed to operate in both polar and longitudinal geometries with minimal physical changes to the optical apparatus. Figures 4.3 and 4.4 show a schematic and photograph of the polar configuration and the longitudinal configuration respectively. For the polar geometry, a 7.5 mW red laser is first collimated to decrease any beam divergence to negligible levels. An upper limit for the resultant beam divergence can be estimated from the beam size during initial alignment. To ensure the collimator is aligned parallel to the optics bench mounting holes, a target was placed at the opposing end of the bench, approximately 500 mm away from the collimator. No noticeable change in beam size was observed at this point when compared to the initial beam size of 10 mm radius, to within an estimated precision of 1 mm. An upper limit for the beam divergence after collimation is, therefore, 2 mrad ($\tan^{-1}(1/500)$).

After collimation, a beam splitter is introduced. This beam splitter introduces a white light source for the purposes of sample imaging. The initial polariser is of variable angle in order to select s- or p-polarised light. An iris can reduce the beam diameter from a maximum of 15 mm to approximately 1 mm, although no noticeable focusing benefits are achieved below 5 mm for the chosen focusing lens. A focusing lens of focal length 5 cm was used for room temperature measurements, however, when performing cryostat measurements, space limitations required the use of a 10 cm focal length lens. The typical laser spot size at the best focus is 20 μm. As light is incident upon the sample at normal incidence, the beam splitter that immediately follows the iris serves to split the incident and reflected beam paths. The reflected beam path is deflected by a mirror towards a quarter wave plate. The quarter wave plate removes any induced ellipticity in the laser beam polarisation before it passes through a second polariser which transforms any polarisation rotation into an intensity change. A flip mounted mirror can direct the beam to a camera which, when used in conjunction with the white light source, provides images of the sample features. Under normal operation, the white light source is off and the flip mount mirror is removed such that the laser beam path terminates at the detector. All electrical elements are centrally controlled by a computer running a custom Python user interface, with more details in section 4.3.3.

The longitudinal geometry is largely the same as for the case of the polar geometry, therefore, only changes to the previous polar description will be highlighted. In particular, the only area of optical setup that changes is the portion of the beam

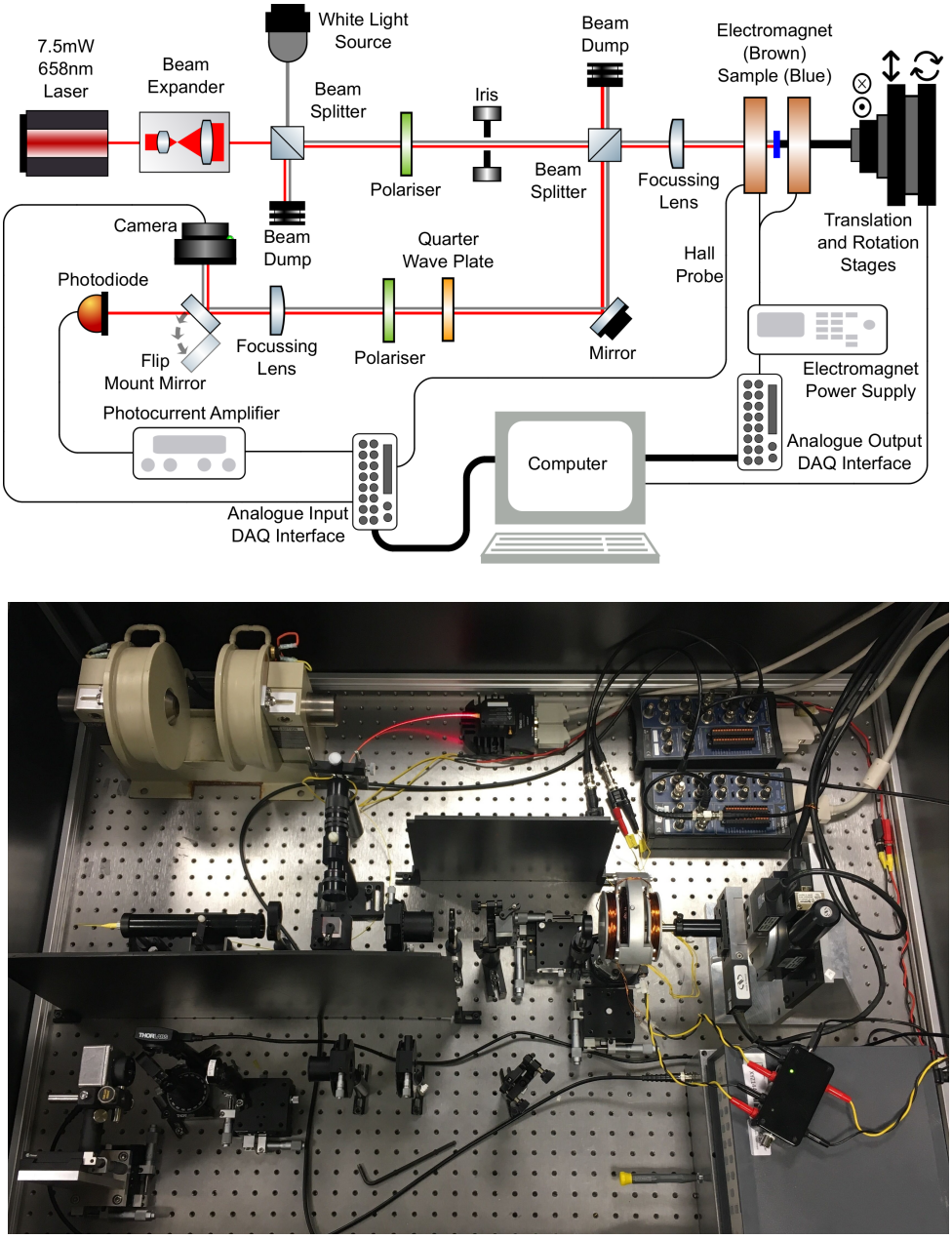

Figure 4.3: The MOKE instrument set up in polar orientation. For schematic clarity, some objects appear in a different place in the photograph; Spare electromagnet (top left), laser diode source (top middle), input and output DAQ board interface boxes (top right), photocurrent amplifier (bottom right).

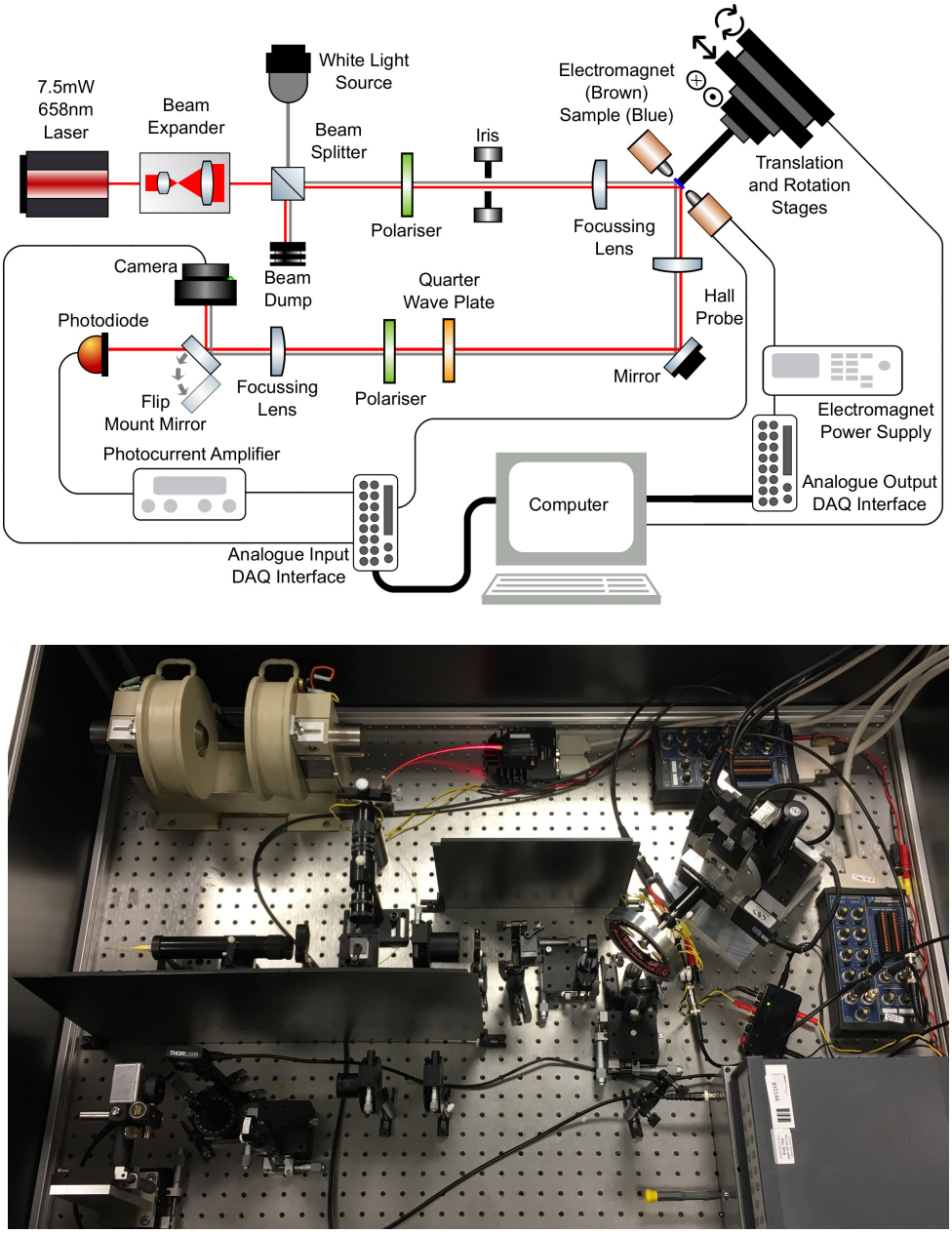

Figure 4.4: The MOKE instrument set up in longitudinal orientation. For schematic clarity, some objects appear in a different place in the photograph; Spare electromagnet (top left), laser diode source (top middle), input and output DAQ board interface boxes (top right and middle right), photocurrent amplifier (bottom right). The beam splitter, present in the photograph before the focusing lens yet omitted from the schematic, is lowered out of the beam path and is unused.

path after the iris and before the quarter wave plate. As the laser is incident at 45° to the sample surface, the reflected light is at 90° to the incoming light allowing for the removal of the beam splitter immediately prior to the first focusing lens. The sample stage has been rotated by 45° to allow for such laser incident angles. For the case of polar MOKE, the reflected beam passes through the same focusing lens which is used to initially focus the beam. This is not the case for the longitudinal setup, therefore, a second focusing lens is added immediately after the sample to re-collimate the laser beam.

It is possible to orient the latter half of the beam path (quarter wave plate and beyond) vertically in both the polar and in-plane schematics as to eliminate the mirror placed after the sample. In practice, however, this mirror serves an important role regarding usability. First, it allows for the separation of the optical bench in to two sections, one that remains the same at all times (left) and one that changes when moving from polar to longitudinal geometries and vice versa (right). This both greatly simplifies the transition and also decreases the set up time significantly as the full re-alignment of all optical elements is not needed. Secondly, it allows for the correction of any small beam deviations when replacing a sample. Although the best effort should be taken to replace the sample at 45° to the beam, in practice there will be an associated variance. If this mirror was missing, then this variance would have to be corrected by either an additional tilt stage for the sample or by adding translation stage mounts for all components between the quarter wave plate and detector. The additional tilt stage for the sample is unsuitable as these can be relatively large (approximately 5 cm by 5 cm) when compared to typical sample sizes (1 cm by 1 cm), hence limiting the magnet pole piece gap and subsequently the applied magnetic field magnitude. As for introducing translation stages, this option can become expensive for multiple stages when compared to the single mirror required for the setup shown.

Figures 4.3 and 4.4 show the relative orientation of each component with respect to each other, yet it ignores the rest of the room. In practice, this is very important as there can be external factors that influence the measurement. The previous laser power calculations (section 4.2.2) show that the incident power upon the detector is approximately 60 nW. Although a laser line filter is used immediately prior to the detector to block any light of an undesired wavelength, it is possible that sources such as room lights, computer screens or instrument displays produce light at a wavelength identical to the laser. This background light can interfere with measurements if it varies with time and as such, it is advisable to both keep background light constant and to also orientate the detector away from potential sources.

Typical experimental parameters

One big advantage of this setup is the diverse parameter range available for the applied magnetic fields. The use of a computer controlled arbitrary waveform generator allows for a much greater variety of waveform profiles when compared to a typical waveform generator, which is limited to a continuous square, sine or triangular waveform. An AC magnetic field frequency of 1.6 Hz was used for all measurements with a sampling rate of 20 kHz, corresponding to 12,500 data points per cycle. For a standard hysteresis measurement, a triangular waveform was used for reasons of a constant magnetic field sweep rate and equal data point density across the applied magnetic field range when compared to the typical choice of a sinusoidal waveform. The magnetic field was cycled between 1 and 200 times to achieve sufficient statistics, as per the specific experimental requirements at the time. A range of electromagnets were used across all measurements, however, the standard magnet is shown in-situ in figures 4.3 and 4.4, with the standard cryostat magnet pictured and labelled as the spare electromagnet. The standard magnet consists of two parts, first, an in-plane circular electromagnet capable of magnetic field of up to 200 Oe as depicted in figure 4.4. A second part can be mounted on top which consists of two helmholtz coils for an out-of-plane magnetic field of up to 100 Oe, as shown in figure 4.3.

4.3.2 Sample environments

Custom sample environments were designed for both room temperature and cryostat measurements. The MOKE system is compatible with two cryostats, a closed cycle He cryostat and an Oxford Instruments Optistat liquid nitrogen bath cryostat. For all measurements presented within this thesis, the liquid nitrogen Optistat was used. These environments include the use of low profile pogo pins for the application and measurement of currents and voltages upon the sample. For cryostat measurements, the Faraday effect plays an important role in the design process. The Faraday effect states that the axis of light polarisation rotates as it passes through a dielectric material under the application of a magnetic field that is colinear to the propagation direction. In the context of cyrostats, this occurs within the cryostat window, visible in figure 4.5(a). It is, therefore, desirable for the laser to enter/exit the cryostat in a direction that is perpendicular to the local magnetic field to reduce such Faraday effects. Although this alone is simple to achieve, complications occur when redirecting the laser for normal incidence during polar measurements or at 45° for longitudinal measurements.

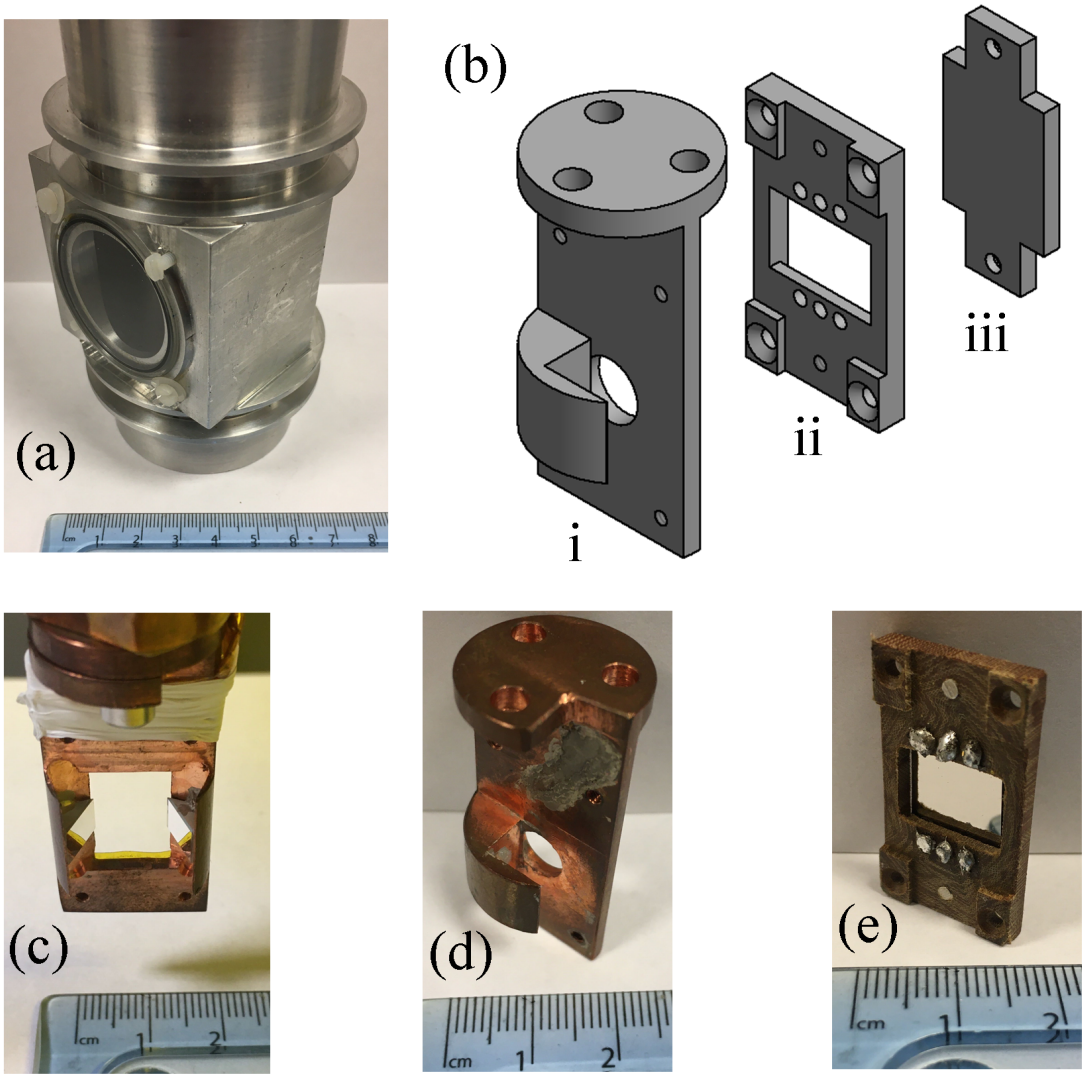

Figure 4.5: Custom sample environment components for electrical measurements of patterned thin film samples in a helium cold head cryostat. (a) Cryostat vacuum housing. (b) Exploded sample environment diagram. (c) Mirror mount for longitudinal MOKE measurements (replaces part i in (b)). The thermometer used is a Si diode and is held in thermal contact with the Cu sample mount under the white PTFE tape shown in the upper portion of (c). (d) Mirror mount for polar measurements (part i in (b)). (e) Electrically isolated sample mount (part ii in (b)).

Figure 4.5(b) shows an exploded diagram of the cryostat sample holder configuration. Part i, also shown in figure 4.5(d), serves to provide a mounting place for a small mirror placed inside the arch like structure half way down the component. This mirror allows for a laser beam entering from the lower right hand side to be reflected by 90°, passing through the hole and towards parts ii and iii at normal incidence. Part ii, also shown in figure 4.5(e), is made of tufnol, a material commonly found in cryostats where electrical isolation is required. This part holds the low

profile pogo pins used for electrical connections to the sample. The sample is placed in between parts ii and iii, which are subsequently screwed together, hence creating permanent pressure upon the pogo pins for electrical contact and a sufficient thermal connection with the rest of the cryostat cold head. A second sample holder, depicted in figure 4.5(c), can be used for in-plane measurements and replaces part i in figure 4.5(b). Here, there now exists two mirrors each placed at 22.5° with respect to the sample normal. Upon reflection from such mirrors, the laser is deflected by 45° which is now suitable for longitudinal measurements. Parts ii and iii are identical for longitudinal and polar sample holders.

Room temperature measurements are considerably simpler as they do not require the laser to propagate through any dielectric components placed within an applied magnetic field. Instead, a sample holder akin to parts ii and iii is used. Here, low profile pogo pins allow for electrical connections to be made to the sample yet still allow for a laser to be incident upon the sample surface at 45°. In both room temperature and cryostat measurements, any voltage measurement will be susceptible to an induced voltage from the applied AC magnetic field. Although this is often reduced through common practices such as the use of twisted wire pairs, this is not possible in fixed connection situations such as the pogo pins displayed in figure 4.5(e). Instead, this induced voltage is removed post measurement. When taking a Hall measurement, two measurements are taken; one each with the current on and off. When the current is on, the Hall measurement is a sum of both the true Hall signal and the induced voltage from the AC magnetic field. The voltage measured with the current off solely measures the induced voltage and, therefore, can be subtracted from the Hall measurement to obtain the true Hall measurement.

4.3.3 Instrument control software

Instrument control was achieved through the development of custom user interface software using the programming language of Python. Two modules form the bulk of this program, `pyDAQmx` allows for the control of National Instruments DAQ cards and `wxpython` provides the user interface features. The program consists of a live view of the data along with extensive parameter control objects and a text panel for the display of system and error messages.

The basis of the data acquisition consists of two elements, a data array for the analogue output data and a sampling frequency. The DAQ device operates by iterating through the output data array at a rate defined by the sampling frequency. If the device is in finite sampling mode, the data array is repeated until the user defined total number of samples has been achieved. If the device is in continuous

sampling mode, which was typical for the standard measurement, the device repeats the output data array until it receives a user stop command. Therefore, if a continuous sine wave is required, the data array should consist of one period of a sinusoidal oscillation. The frequency of such wave is defined through the ratio of the output data array to the sampling frequency, for example, an output data array length of 10,000 elements and a sampling frequency of 20 kHz would produce a 2 Hz continuous sine wave.

Operating the DAQ card in finite acquisition mode allows for the possibility of more complex remote measurements. One can define an output array length that lasts of the order of minutes. This output can, for example, begin with a high positive magnetic field to ensure the sample is saturated in one chosen direction. After this saturation field, a measurement can be performed that requires the use of an AC magnetic field. It is this custom field profile that is not possible with MOKE systems powered by function generators which are limited to waveforms with time invariant

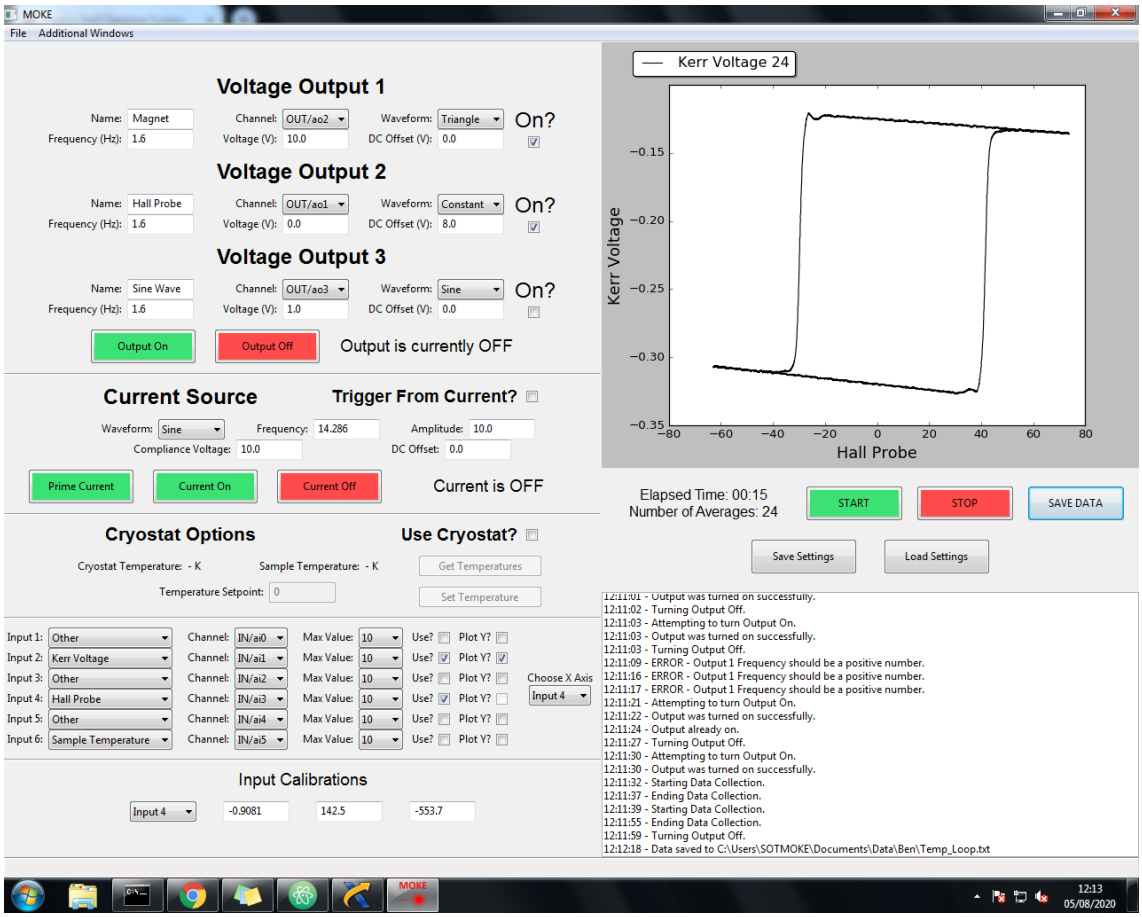

Figure 4.6: The custom Python user interface developed from the MOKE system. Input parameters are grouped by instrument on the left hand side and measurement output, including a live figure, is shown on the right hand side.

parameters. Even with the use of an arbitrary waveform function generator, the majority of these instruments allow for a custom period to be defined, yet it repeats this period and does not allow for a combined DC/AC output. It is this feature that made the work reported in the following chapter possible, which required an out-of-plane magnetic field to initialise the sample in a chosen orientation, before applying an in-plane magnetic field together with a charge current for the required measurement.

Figure 4.6 shows the main window for the MOKE program. The left panel is used for user editable variables, including the amplitude and frequency for the aforementioned output data array. Where appropriate, the variables are presented to the user in a friendly format instead of the format to which the program requires, for example, frequency is presented in Hz while the program converts this to a required data array length for a given sampling frequency. Variables such as the cryostat options shown can be disabled when not required to prevent the accidental modification of the wrong parameter. As this MOKE instrument is designed to be highly versatile, all parameters can be changed ranging from the physical input/output channels to the amplitudes and frequencies of waveforms. From top to bottom, these parameters are for three analogue voltage output channels, a current source for current-induced switching measurements, a cryostat, up to six input channels, and finally a calibration for voltage to magnetic field conversion.

Moving to the right hand side of the interface, a dynamically updating figure is used to display the measurement data. Below this are buttons to start, stop and save measurements along with two buttons for the saving and loading of variable settings allowing for quick access to predefined measurement sequences. Finally, a textbox which displays system and error messages is located at the bottom. It is this textbox which has become the most useful feature of this program over time. Here, the system tells the user both the current state of the program, for example if a measurement is currently running or not, as well as any error messages. These messages can be as simple as invalid parameter values or more complicated errors. For example, if checks for negative frequencies are not performed, then the program will crash when attempting to output such a waveform and require a restart, losing any settings or data that was not saved. Instead, checking for these errors allows for them to be caught before a crash occurs and a prompt can be sent to the user detailing the steps required to rectify the problem. This can be extended to more complicated issues, such as the program expecting to measure a certain amount of data points but only measuring a fraction of such amount, indicating a loss within the system possibly from a loose or missing physical connection. These problems

would not be obvious to the user if the program carried on regardless, hence as to why this debug interface has become important over the years. It is here in which a large amount of the development time is spent, however, the potential rewards in terms of usability and stability are high.

4.4 Initial build and trial measurements

4.4.1 Signal acquisition

There are many aspects to signal acquisition that affect both the accuracy and precision of a measurement, of which it is not possible to list all of them here. Instead, the example of signal ghosting is presented with the intention of demonstrating that it is possible to overcome problems which may seem significant at first through the understanding of the full experimental system. The problem and solutions presented here are specific to the equipment used and, therefore, may not necessarily be present in another system, in particular, they are relevant to devices employing a shared analogue to digital converter across multiple analogue inputs.

4.4.1.1 An example problem: what is signal ghosting?

Simply put, signal ghosting is the unwanted presence of one signal when measuring a second, nominally independent signal. This is different to the commonly misused term of 'crosstalk', the difference between which will be explained shortly. Figure 4.7 shows the consequences of signal ghosting graphically by way of measuring two signals, a DC 5 V signal and a sine wave centred on 0 V with 10 V amplitude. The signals are produced by a multi-channel analogue output computer PCI DAQ card and measured by a separate analogue input DAQ card. First, we measure the 5 V signal in isolation which shows no time dependence as expected. There exists a small yet consistent deviation from 5 V (1 mV below) for all measurements, however, the cause of which is not known and could be due to the source or acquisition device, losses over terminal connections or wires etc. As this test data aims to demonstrate signal ghosting, the accuracy of the calibrations for such analogue devices or any losses within the system are not important at this stage and this deviation is therefore ignored.

After measuring the expected DC 5 V signal in isolation, figure 4.7(b) shows the simultaneous measurements of the DC signal followed by the sine wave. At this point, it is worth clarifying what exactly is meant by 'simultaneous' and 'followed by'. Simultaneous measurements refer to measurements taken in parallel, i.e. collecting

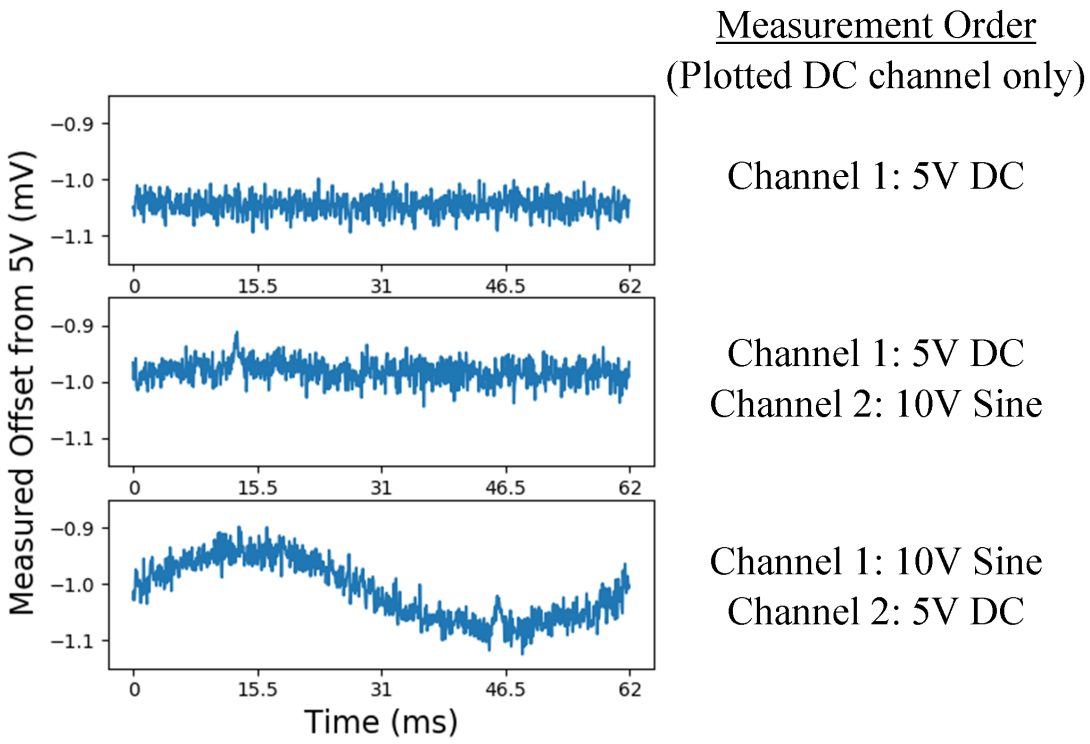

Figure 4.7: The effect of signal ghosting upon the measurement of DC 5 V signal in conjunction with a 16 Hz, 10 V amplitude sine wave. The importance of channel order is shown with the appearance of a ghost signal only when the measurement is performed immediately after a large AC signal.

the first data point of channel one and two, then moving on to the second data point of both channels etc. As will be shown in the following paragraphs, this does not necessarily mean that equivalent numbered data points (i.e. the first data point of each signal) are measured at exactly the same time. The term 'followed by' simply refers to which channel the signals are connected to. Any device with multiple inputs will have labels similar to 'Input 1, Input 2...' or 'Channel A, Channel B...'. In this example, the DC signal is connected to the primary input (Input 1 or Channel A) followed by the sine wave in the secondary channel (Input 2 and Channel B).

Now that the measurement setup has been strictly defined, one can inspect figure 4.7(b) for the presence of any ghost signals. Through comparison to figure 4.7(a) it is clear that the signal is near identical, barring some statistical noise fluctuations. Importantly, no obvious sine wave exists showing that there is no ghost signal from channel two present on channel one. Figure 4.7(c) shows the signals after reversing the connections such that the sine wave is connected to the primary channel and the DC signal to the secondary. A ghost signal is now present on top of the DC signal in the form of a 0.1 mV amplitude (0.001% of its true amplitude) sine wave.

Earlier it was stated that signal ghosting is often mislabelled as crosstalk without explanation. Crosstalk exists when two wires or circuits are coupled such that one circuit transmits a signal which is then received by the second wire or circuit. There exists no physical electrical connection between both circuits, instead, the signal is transmitted and received through the associated electromagnetic radiation. The measurement device used here has 16 input channels of equal specification, therefore, it is reasonable to assume near identical circuitry onboard the device. If the signal shown in figure 4.7(c) was a consequence of crosstalk, then it should be present in figure 4.7(b) as the coupling should be equal in both directions for the circuits corresponding to channels one and two. As this is not the case, the cause is determined to be signal ghosting.

4.4.1.2 What is causing this signal ghosting?

Signal ghosting is a consequence of more efficient circuit design often found in cheaper devices favouring fewer components shared across multiple channels. Broadly speaking, equipment such as oscilloscopes or high end DAQ cards are likely to have fully independent input channels, complete from physical input connection to digital voltage reading. Conversely, lower end devices will have independent components only where necessary, such as the physical input terminals, but may share internal circuitry such as analogue to digital circuits. For the relatively inexpensive DAQ device used here, the eight analogue input channels share one analogue to digital circuit, therefore, potentially saving 93 % of the cost required for this particular component.

Figure 4.8 shows a summarised circuit diagram for a 32 input analogue device with sources labelled 0 to 31. Each voltage source has a characteristic impedance, represented by R0 to R31, and is physically connected to terminals ai0 to ai31 respectively. At this point, a single multiplexer is connected to all channels. A multiplexer is a device used to switch between multiple inputs and forward a selected input to the output channel without modification. Finally, an analogue to digital circuit (ADC) measures the input voltage.

To achieve simultaneous measurements, as used in the previous discussion of figure 4.7, the multiplexer must switch between all inputs to be measured before waiting for the second data point in the series. This is shown graphically in figure 4.9 for a four channel measurement. Figure 4.9(a) shows the typical profile of measurement timings showing a small offset for each subsequent channel to allow for the previous channel to be measured and for the multiplexer to switch inputs. The device used here has a peak sample rate of 200 kS/s (thousand samples per second)

for eight differential inputs or 16 single ended. Assuming the highest sampling rate and all 16 single ended channels used, this corresponds to a multiplexer frequency of at least 1.6 MHz, or 625 ns between each individual multiplexer switch. Comparing the time differences between each individual measurement shown in figure 4.9(a), when switching from channels one through to four the interchannel delay time is multiplexer limited and is, therefore, less than or equal to 625 ns between measurements. After measuring channel four, the device waits a period of time before measuring channel one as to achieve the desired overall measurement frequency. A measurement frequency of 20 kHz (50 μs period) is the typical operating frequency for a measurement on this MOKE instrument. This creates a disparity in the system in which there exists different dwell times between subsequent measurements.

Armed with this knowledge, the impact of these measurement timing differences upon the measured signals can be investigated. Each signal source has an associated impedance, which when combined with the small internal capacitance of the ADC creates a low pass filter. This filter has a time constant, often referred to as the settling time, in which higher time constants require a longer amount of time for the voltage to stabilise at its true value. This means that after channel one has been measured, the multiplexer switches to channel two. For a short period of time, characterised by the time constant, the ADC has not stabilised to the true value of channel two. If the measurement of this channel is taken before such stabilisation has occurred, then a small remnant of signal one will still be present within the ADC and hence will be measured together with signal two, creating a ghost signal.

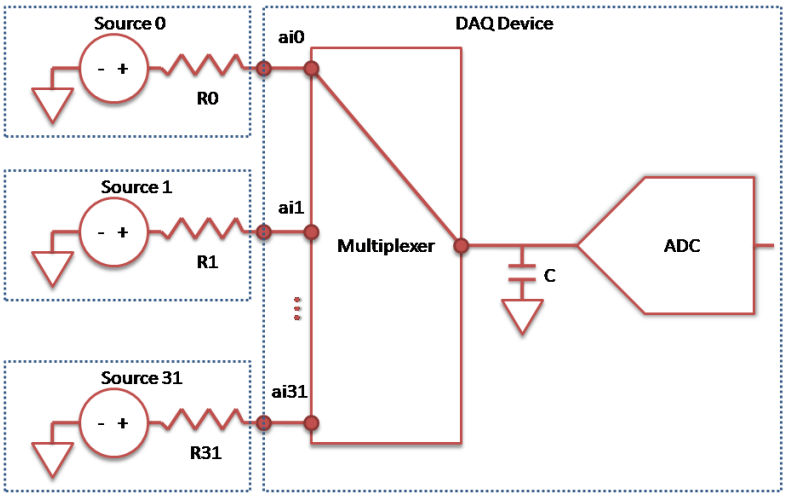

Figure 4.8: Reproduced from National Instruments support web pages [92]. A schematic representing a simplified analogue measurement device with multiple physical input connections (source 0 to 31) connected to a single multiplexer and analogue to digital converter.

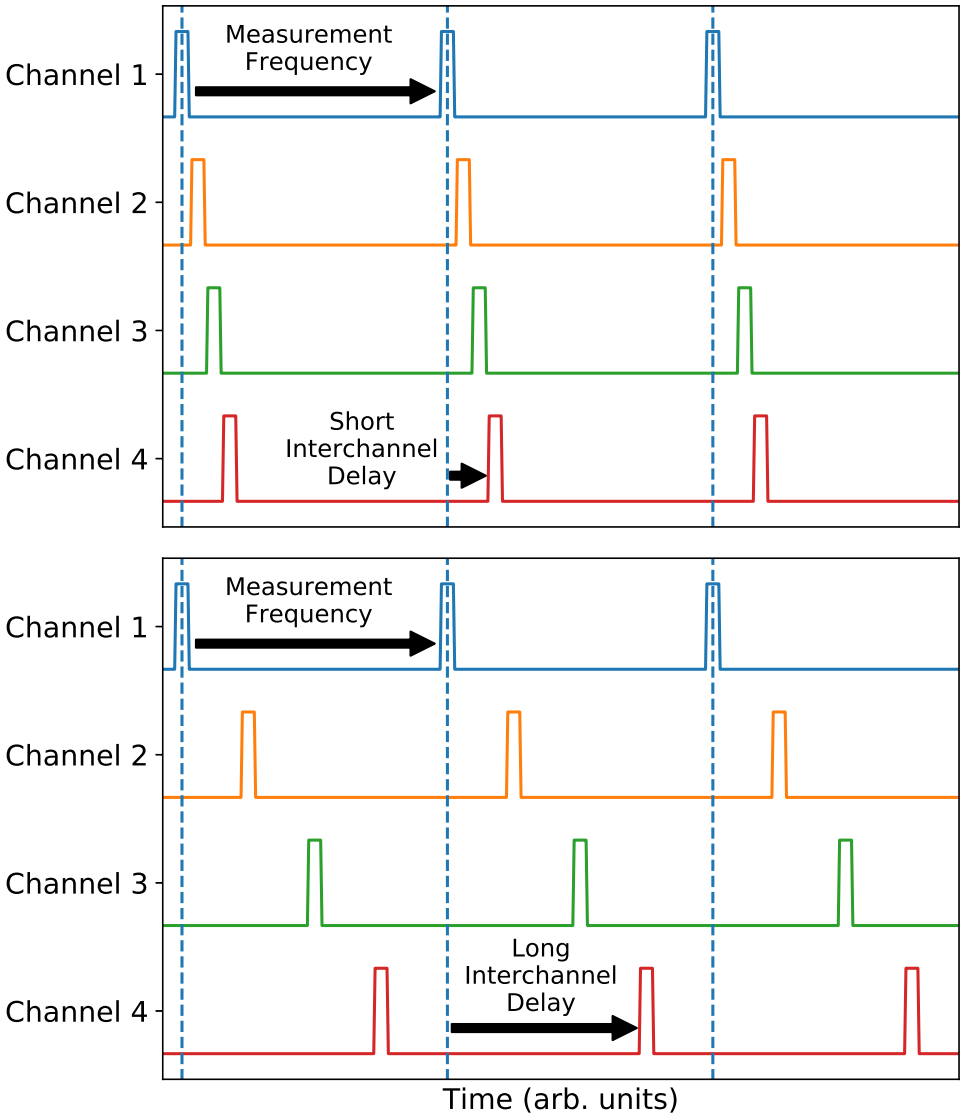

Figure 4.9: A visual display of the measurement timing within a multi-channel measurement. The desired measurement frequency dictates the time difference between subsequent measurements of the same channel, with device architecture (and occasionally device settings) dictating the interchannel measurement delay time.

If, however, a sufficient time period has passed (i.e. much greater than the time constant) then the ADC will have stabilised at the true value of channel two and no ghost signals will be present.

4.4.1.3 How do we manage signal ghosting?

As mentioned at the very beginning, this issue is specific to devices with shared components. Therefore, the simplest solution is to acquire a device with independent channels hence removing this problem at its source. In practice, these devices are

often more expensive and it is not always possible to acquire the budget for such replacements, therefore, a different solution is required. Fortunately, this is well known to device manufacturers and there exists two common approaches to manage signal ghosting.

First, the act of changing the source impedance changes the low pass filter characteristics including the time constant of each channel. High impedance sources correspond to a filter with a high time constant, hence lowering the source impedance reduces signal ghosting through decreased stabilisation times. The source impedance is often determined from the connected instrument, of which the user often does not get a choice in the value. The impedance as seen by the input device can be modified through the use of buffer circuits. The creation of such circuitry is not trivial to the average user and hence is a common feature within more expensive DAQ devices. Rather than upgrading to a higher end DAQ device or investing significant amounts of time developing custom circuitry replicating such features, there exists a second method which is more appropriate to the situation.

It is possible to modify the interchannel delay time, specifically to increase the value such that the ADC has time to stabilise no matter the value of the time constant. This can be done through software on certain devices, or by artificially creating delays through added measurements. Figure 4.9(b) graphically displays the results of such delay modifications. Contrary to figure 4.9(a), the interchannel time delay has been modified in figure 4.9(b) such that there is a consistent time between all measurements which is much greater than the most common time of less than 625 ns in figure 4.9(a).

Changing this interchannel delay time is the optimal solution, yet it requires software control of the multiplexer component and is, therefore, only available on devices with this feature implemented. As the sharing of ADC components is often used to make devices more affordable, features such as multiplexer control may be categorised as non essential and may be omitted. Thankfully, there exists an extension to this solution, albeit less optimal.

The second part to this solution artificially extends the interchannel delay time by introducing intermediate channels, to which the time taken to measure such channels acts as a delay between the surrounding channels. Returning to the previous measurement of two signals, a 10 V sine wave and 5 V DC signal, we can introduce a dummy signal in between such that the measurement order is now 1) sine wave, 2) dummy channel and 3) DC. Assuming the multiplexer limited interchannel delay of 625 ns, there is now 1250 ns between the measurement of the sine wave and the DC signal which allows for more time for ADC stabilisation, however, the possi-

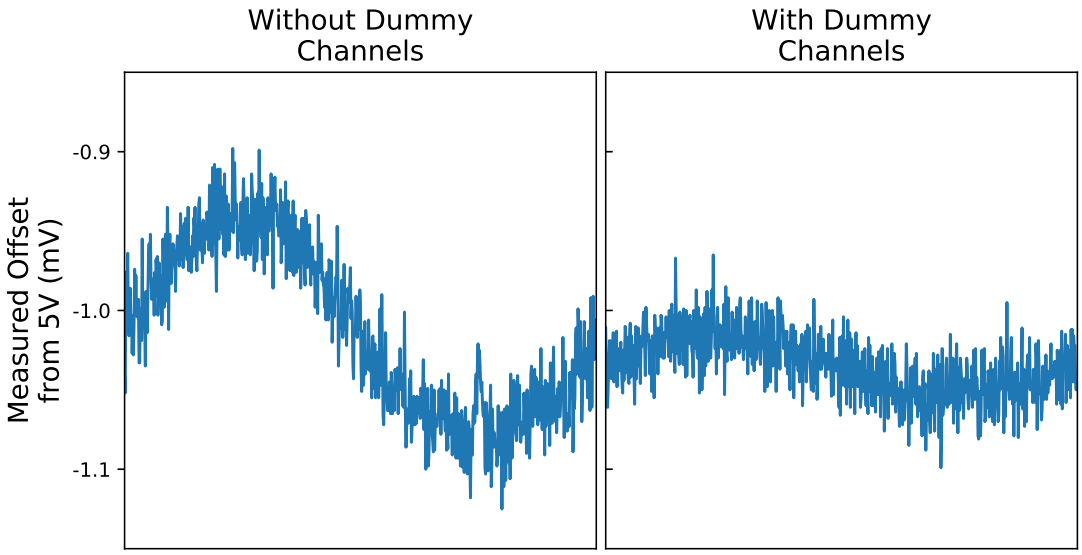

Figure 4.10: The reduction of signal ghosting when dummy channels are used (right) compared to without (left). Each measurement is performed twice, in the order A A B B C C... with the first of each identical measurement referred to as the dummy channel and the second measurement is the actual measurement.

bility of ghost signals from the dummy channel has been introduced. To combat this, we simply measure the same channel twice with the first measurement acting as the dummy channel, such that the order is now 1) sine wave, 2) DC (dummy) and 3) DC. The middle DC (dummy) measurement is still susceptible to the same magnitude of ghost signals as in the case of a two channel measurement, hence the data are ignored. The second DC measurement will have a reduced sine wave ghost signal due to the effective doubling of the interchannel delay time and no ghosting from the dummy DC channel as the signal is nominally identical. The effect of this is shown graphically in figure 4.10 by which a two signal measurement is performed on the left, namely a sine wave followed by a DC 5 V signal. A clear ghost signal is present in the measured DC signal. On the right, each signal was measured twice with the first acting as a dummy measurement and only the second measurement was saved. As is clearly evident, this has reduced the magnitude of the ghost signal by an approximate factor of three.

Adding more dummy channels will extend this interchannel delay further, however, it will produce diminishing returns. If we were to assume common trends observed in signal decays, then to reduce the ghost signal by a further factor of 3, the interchannel delay time would have to be double again, i.e. through the addition of two extra dummy channels. This would, however, rapidly take up all of the available channels for our device making multiple dummy channels undesirable.

4.4.1.4 Conclusion

Signal ghosting has been shown to exist in the measurement device through the presence of sine waves upon subsequently measured DC signals and the dependence upon measurement order and delay times has been investigated. For accurate signal measurement, the most important signal is to be measured first as there exists the longest delay time prior to this measurement. Failing this, dummy channels should be incorporated to artificially increase the delay time. Applying this to the MOKE instrument, the Kerr signal is to be measured first, followed by measurements such as the Hall probe. Secondly, dummy channels should be introduced as the device is capable of measuring eight inputs, whereas only two are currently utilised. For measurements with more signals, these dummy channels can be selectively omitted as to protect only the signals that require signal ghosting protection.

4.4.2 Measurement stability

The stability of a measurement can depend on many sources, of which the importance varies depending upon the nature of the instability and the intended use of the system. The most widely known source of instability is noise, random fluctuations in an otherwise constant value. Beyond this, other sources of instabilities include periodic oscillations, linear drifts and correlated noise. Across long timescales, correlated noise is akin to traditional noise with its random nature, yet on small timescales there exists local correlation. An example of each type of noise studied is shown in the left hand column of figure 4.11, together with its effect on single shot and averaged MOKE measurements.

The first row of figure 4.11 depicts an unmodified measurement, which shows that increased averaging increases the signal to noise ratio, however, the overall shape of the loop remains the same, as expected. The second row presents the effect of increased random noise, simulating, for example, a laser source of lower quality. In both cases, the measurement is the same shape as that of the single shot and averaged unmodified measurement, yet with increased noise. The noise can be continually averaged out over longer time periods with diminishing returns. The next row displays Perlin noise which is a commonly used algorithm to generate correlated noise. The effect on a single shot measurement is severe, with the results being inconsistent with the unmodified measurement. This measurement is not repeatable since a single shot measurement taken seconds later would exhibit a different form of Perlin noise and so would be modified in a different way. There exists a break in the presented data which represents the beginning and end of the

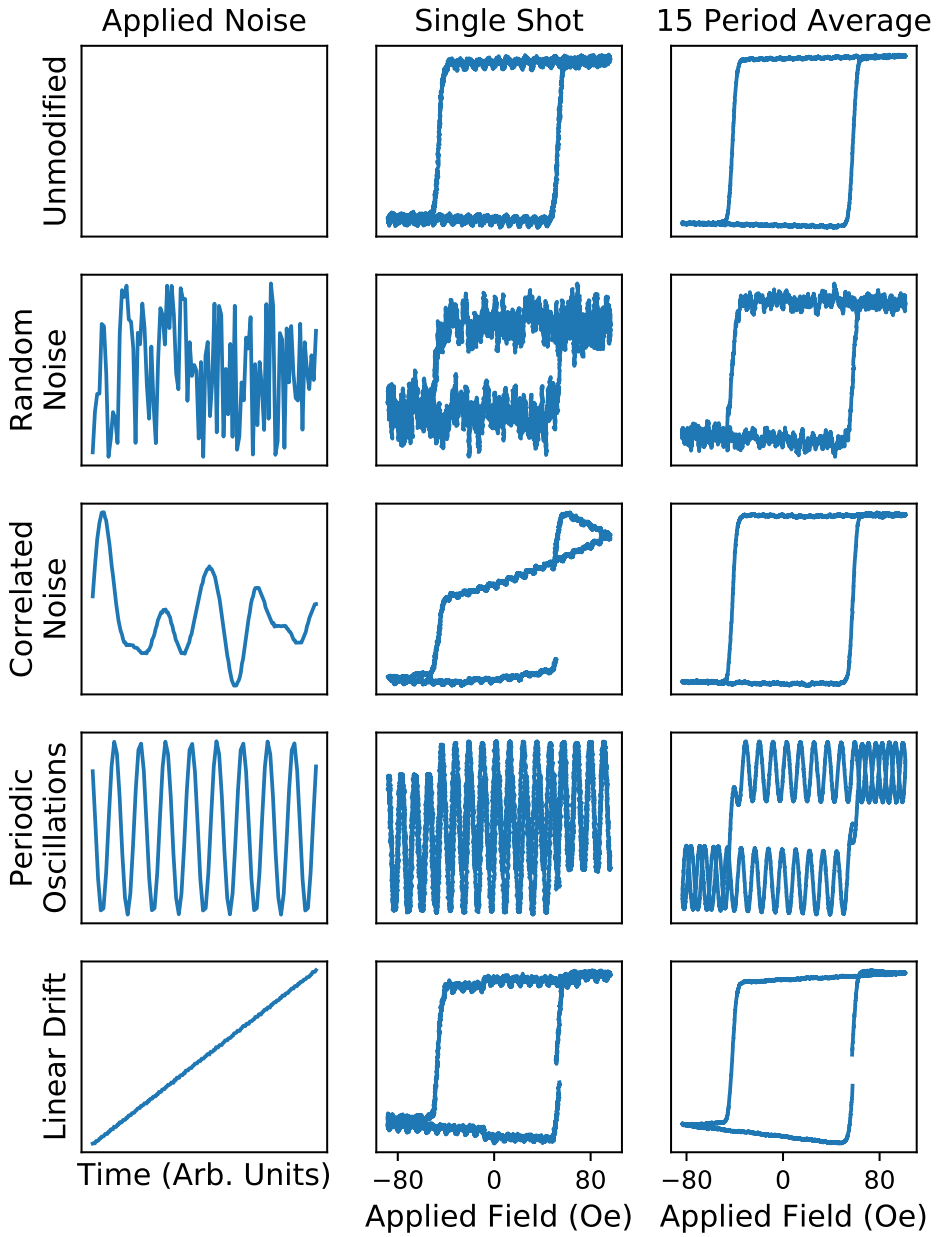

Figure 4.11: Four unique instability profiles and their associated effects upon single shot and averaged MOKE measurements. The amplitude of the applied noise is 3 % of the nominal laser diode current and the left hand column displays a one second snapshot of the artificially generated noise.

applied field period. A discontinuity here is caused by the ending intensity differing from the initial. Ultimately, Perlin noise is approximately a sum of oscillations at varying frequencies and amplitudes, therefore, time averaging the signal can remove these oscillations. This is shown within the 15 point average measurement which resembles that of the unmodified measurement. Penultimately, a regular periodic oscillation has been studied. The frequency of such oscillation was chosen such that it is a multiple of the applied field frequency. As this oscillation is on resonance with the measurement frequency it will not be averaged out, hence it has a severe effect on both the single shot and averaged measurement. Finally, a linear drift in laser diode current also effects both the single shot and averaged measurements. Small discontinuous steps can be observed in the single shot measurement which are attributed to the limited resolution when generating a linear diode current variation.

Analysis of measurement stability is dependent upon the system requirements. Here, the system is predominantly designed for use in current-induced magnetic reversal measurements. These measurements can heat up the sample over long periods of time, therefore, single shot measurements are preferred to those which require long averaging times. Figure 4.11 shows that the only acceptable instability is random noise, albeit not desirable. To reduce the random noise, dedicated high quality laser diode temperature and current controls were used. For generic thin film measurements, to which long averaging times are acceptable, correlated noise like instabilities are also acceptable. Along with increased random noise, these instabilities often come from lower quality laser diode controllers which can decrease the cost of the system, if that is desirable. The final two forms of instability, namely, periodic oscillations and linear drifts, are undesirable in both single shot and averaged measurements. Periodic instabilities can be caused by the likes of 50 Hz mains interference in unshielded components. The most common linear drift is observed immediately after turning the laser on, to which the diode is progressing towards thermal equilibrium. It is possible to correct for such noise sources through the use of a second photodiode. This photodiode is responsible for monitoring the time dependence of the laser intensity and does not include a Kerr component. This solution increases the measurement complexity, however, it can be a cheaper option when compared to the purchase of a more stable laser source. The increased complexity, both with increased alignment procedures and additional data analysis steps, is often undesirable in basic MOKE systems, yet is common in high accuracy systems.

The keen observer will note the presence of small, periodic oscillations within the unmodified measurements, particularly that of the single shot measurement. These

measurements are attributed to vibrations within the system particularly that of the sample stage. To reduce the effect of such vibrations, the measurement frequency of 1.6 Hz was chosen to be off resonance with the approximate natural frequency of such vibrations, hence allowing for such oscillations to be time averaged. Other factors, such as the use of a good quality optics table and rigid mounting devices, also contribute to the reduction of vibrations. Together with the use of high quality laser diode controls, the chosen setup is determined to be well suited for the single shot thin film measurements presented in this thesis.

4.4.3 Instrument timing

Two Devices: Input and Output DAQ Cards

Instrument timing is imperative to accurate measurements and, in many cases, is very simple to achieve. Oscilloscopes, and some modern DAQ cards, generally have a dedicated trigger channel. This channel receives a pulse when each period of an AC signal begins, hence providing a starting point for measurements. Here, the two DAQ boards chosen did not posses a dedicated trigger channel which caused the instrument timing to be more in-depth.

Generally, all timing is performed under the same concept in which there exists a controller device and one or more peripheral devices. The role of the controller is typically assigned to an output source. This principle is simple to understand with trigger signals, as one device acts as the controller and outputs a trigger signal to which all other devices in the system, which are called peripheral devices, read the trigger signal and act accordingly. The controller device has the power to stop the entire experiment by stopping the trigger signal output. Peripheral devices can only stop themselves as they can ignore the trigger signal, but cannot stop it being output by the controller device. When the option for using a trigger signal is not available, the same controller/peripheral principle can be applied to other modes of timing.

All AC devices have an internal clock which oscillates at a constant frequency which is used to determine the instrument timing. Unfortunately, all devices have a limited accuracy, therefore, one devices 5 MHz clock frequency can be seen as 5.001 MHz to a second. This limited accuracy causes a phase drift between different AC devices over time, as displayed graphically in figure 4.12. The MOKE measurement is of a thin film sample under identical conditions, yet with changes to the instrument timing. The blue dashed curves in both top and bottom figures were taken with the correct controller/peripheral instrument timing setup. The black solid curves were

taken when the instruments were timed independently through their own internal clocks, therefore, allowing a phase difference to occur between AC waveforms. The top graph shows that after four seconds there exists no observable difference between the two measurements. From this we can deduce that no phase shift has occurred within this time. When the measurement is averaged over a longer period of time, in this case four minutes, a significant difference becomes apparent. By adding a phase difference which increases with time, the signal is effectively being time averaged, hence features become broader and smoother. This is apparent in figure 4.12, as the switching behaviour for the incorrectly timed measurement has a much shallower gradient. When compared to the four second measurement, the correctly timed four minute measurement is identical.

To achieve correct instrument timing without a trigger signal, we must not use the internal clocks of all devices. Instead, one device acts as the controller and outputs a square wave at the desired sampling frequency based upon its own internal

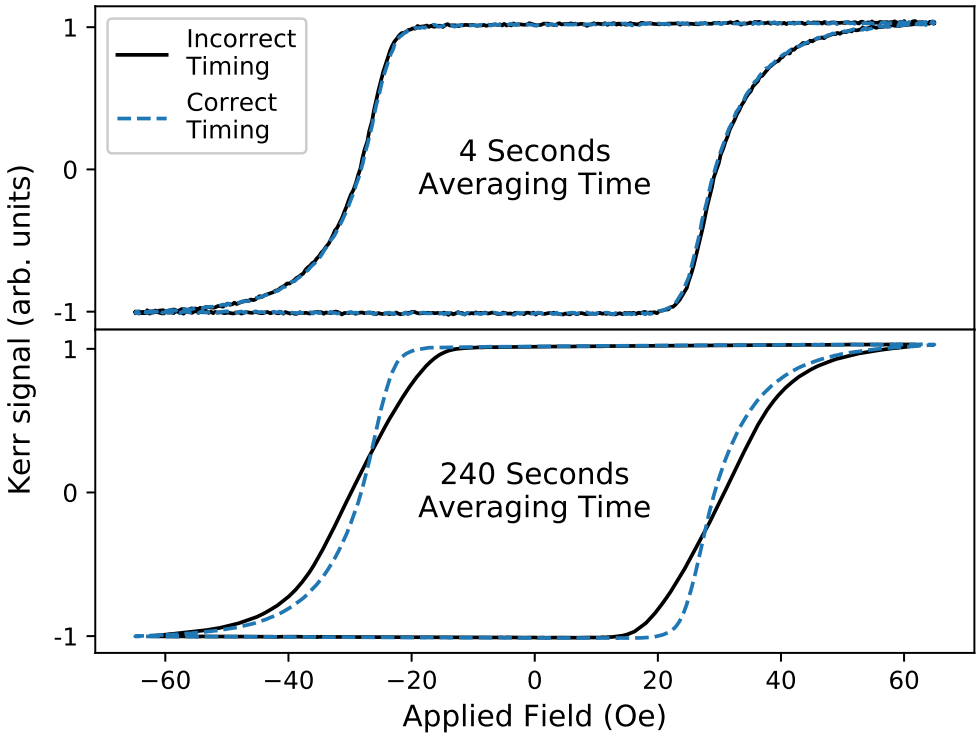

Figure 4.12: The difference in measured MOKE signal when using the correct instrument timing (blue, dashed) compared to independently timed instruments (black, solid). Both measurements are identical for short measurement times, yet for longer measurement times, the shape of the MOKE hysteresis loop is significantly affected.

clock. This square wave, of frequency 20 kHz for figure 4.12, is then fed into all devices, including the controller which it originated from. As all devices are now using the same source signal for the sampling rate, there exists no possibility of a phase difference between devices occurring. The controller device which outputs this square wave acts as both a controller and peripheral device in this setup as it both outputs a square wave based upon its internal clock, and determines the measurement sampling rate using this square wave.

A possible source of error is introduced with this method, yet it is relatively straightforward to monitor with appropriate software design. If the output device produces a square wave of 20 kHz, one should expect 20,000 readings to be made per second for the input device. If there exists a source of signal deterioration, possibly from a loose or missing connection, it is possible that some of this square wave is lost. This would mean that the input device may only see a fraction of the 20,000 expected pulses. As the frequency is set within the custom MOKE program, it is possible to monitor the actual number of measurements and compare such values to the expected number of measurements. If there exists a significant disparity, the measurement is stopped and the user is notified through the inbuilt text box designated for such error messages.

Three devices: two DAQ cards and a current source

The timing is complicated further when a third device is added, specifically a Keithley 6221 current source in this case. The previous solution of generating and using a continuous 20 kHz wave is not compatible with this current source as it is only able to be timed from its internal clock. Instead, a system is set up which emulates a traditional trigger source, yet still produces the required 20 kHz square wave for the DAQ card timings. First, the current source outputs an AC signal determined from its internal clock along with a separate trigger signal. This trigger signal is fed into the DAQ output card to trigger the 20 kHz square wave. This square wave is now of finite length, equal to one period, in contrast to the previous case for two devices in which it is a continuous wave. Each subsequent period of the current source wave outputs a new trigger pulse, which triggers a further finite period of square wave pulses. If the current source AC wave is continuous, this behaves like a continuous 20 kHz square when in fact it is stopped and restarted every period.

Here, we now have two interconnected controller/peripheral timing systems. First, we have the current source acting as a controller device by outputting a trigger signal. The DAQ output device then acts as a peripheral device and outputs a finite square wave each time it receives a trigger pulse. Secondly, this square wave can

be thought of as a controller signal that controls two peripheral devices, the same DAQ output card and also the DAQ input card. Although this may seem overly complicated, a quirk of the chosen DAQ devices means that this is the simplest attainable timing architecture. For example, one may ask why the trigger signal is used to trigger a 20 kHz wave instead of triggering the analogue output directly. Both of the chosen DAQ devices do not support triggerable analogue outputs, yet include programmable function input (PFI) lines which support triggering. These lines are typically dedicated for clock, trigger and synchronisation operations. The trigger signal is, therefore, input into one PFI line, to which the device responds by outputting a square wave on a second PFI line. This square wave is then input to a dedicated external clock port to control the analogue outputs. Therefore, by adding the PFI lines into the timing chain, we are able to emulate a trigger system for the analogue output channels without the feature being available on this particular device.

4.5 Conclusions

A MOKE instrument has been designed and built for general thin film magnetic hysteresis determination with the capabilities of both applied field and current driven reversal. It is capable of measuring samples patterned to micron dimensions in both out-of-plane and in-plane configurations. First, identification of suitable components consistent with the use of DAQ cards was performed. After the purchase and implementation of such parts, the MOKE instrument was rigorously tested for accuracy. This included the accuracy in measuring a particular voltage, susceptibility to various forms and sources of noise and the accuracy of instrument timing. Several issues were discovered and have been rectified through additional measurement control steps and/or the implementation of good measurement practices. Ultimately, the system is well suited to the intended use and as such is used throughout all results chapters within this thesis.

Chapter 5

Field-free magnetic reversal utilising the charge current Oersted field

5.1 Introduction

Spin-orbit torques (SOTs) offer a mechanism by which the electrical manipulation of magnetisation can be performed, including deterministic magnetic reversal [93, 94]. A common method for achieving such magnetic reversal is through the use of a heavy metal/ferromagnet bilayer [95–99]. An in-plane current within the heavy metal layer produces a transverse spin current as a consequence of the spin-orbit interaction [93, 94, 100]. This spin current can propagate into adjacent ferromagnetic layers exerting a torque upon the magnetisation. The origins of such torques, and their effect on magnetisation, are discussed in more detail in chapter 2.

For magnetic memory applications, structures which exhibit perpendicular magnetic anisotropy are desired for their increased sensitivity and lower wafer footprint [101]. Unfortunately, the SOTs produced by an in-plane electrical current cannot deterministically switch the magnetisation alone as they require further symmetry breaking [102]. Instead, the SOT drives the magnetisation towards the midpoint and effects such as thermal fluctuations can cause the magnetisation to relax to either the up or down state if they are strong enough. For deterministic switching, a symmetry breaking contribution to the effective field parallel to the applied electrical current is required for out-of-plane magnetised structures [96, 97].

The required symmetry breaking field has often been applied externally [96–99]. This is not practical for device applications and as such there has been work to develop external field-free switching devices. First, this was achieved by integrating structural variations in which an anisotropy gradient was created [103–105]. It was shown that creating wedge shaped ferromagnetic or adjacent oxide layers with

thickness gradients perpendicular to the applied current flow can give rise to an anisotropy field sufficient to break symmetry and induce deterministic switching.

Beyond this, further techniques have emerged for developing external field-free magnetic switching. Symmetry breaking techniques include the use of exchange biasing from antiferromagnets [106–108], piezoelectric substrates [109], tilted anisotropy from external wedges [110], spin currents with an out-of-plane component to the polarisation [23–26] and devices utilising SOT-driven domain wall motion [111].

All of these methods present potential avenues for SOT magnetic memory devices, each with their own advantages and disadvantages. The most common disadvantage is wafer uniformity and capacity. Taking wedge shaped structures as an example, achieving wafer scale homogeneity of wedge shape memory elements on the 10's of nm scale is extremely difficult [101]. The minimum feature size of memory element arrays is typically limited by the lithography technique which sets the benchmark for element density [112]. When introducing a new physical characteristic to each memory element, such as wedge shaped structures, there is potential for the minimum size of the wedge shaped magnetic element to be greater than that of the lithography technique, therefore, increasing the size of each element and decreasing the data storage density.

Here, a new method of field-free magnetic reversal is presented involving the electrical contact wire geometry. It is postulated that non-uniform current propagation through a conductor that undergoes a sharp reduction in size can produce a local magnetic field component which breaks the required symmetry for deterministic magnetic reversal. This local magnetic field can initiate magnetic reversal, which proceeds through domain wall propagation. This method shifts the structural requirement from the magnetic element itself to the connecting wires and surrounding infrastructure, creating the possibility to retain the minimum feature size as determined by the lithography technique.

This chapter first details the current-induced magnetic reversal expected from a heavy metal/ferromagnetic bilayer. Simultaneous bidirectional switching is then presented, by which half of a Hall bar switches from an up to down state, with the other half switching in an opposite direction during one single current application. By adjusting the position of the Hall bar with respect to the electrical contact pads, this switching ratio can be tuned to produce a greater Hall bar area switching in one direction relative to the other. Finally, the possible origins of such switching are discussed, including the most likely explanation of the Oersted field providing the symmetry breaking field.

5.2 Description of the samples investigated

Three samples have been investigated with a nominally identical thin film structure, but with differing photolithographic patterning. A Pt(1 nm)/Co(0.6 nm)/Pt(4 nm) Hall bar of 20 μm width and 140 μm length is positioned between two Cu(60 nm) electrical contact pads. The electrical contact pads are 60 μm wide and have a separation of 100 μm, creating an overlap of 20 μm at each end of the Hall bar. The three samples consist of the Hall bar positioned at the centre, edge and an intermediate offset position with respect to the electrical contacts, as shown in figure 5.1.

All layers were sputter deposited onto a Si wafer with a surface layer of 100 nm of thermally grown SiO_2. The thermally grown SiO_2 layer serves two purposes. First, it provides an insulating barrier between the semiconducting substrate and the thin film. Second, the surface roughness is lower than that of a Si layer with a natural oxide coating. The thin film deposition used a growth pressure of 1.3×10^{-3} Torr and a base pressure better than 8×10^{-8} Torr. During the Hall bar deposition, a second substrate was coated simultaneously without any photolithographic patterning for the purposes of XRR characterisation of the trilayer structure. Figure 5.2 shows a longitudinal and polar MOKE measurement of the trilayer investigated, indicating a clear perpendicular magnetic anisotropy and no magnetic reorientation and/or tilting for the in-plane field magnitudes used here.

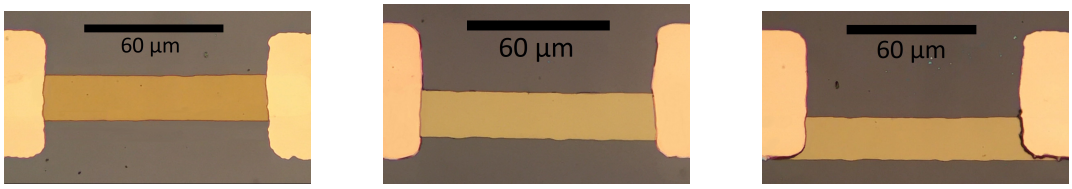

(a) Centred Hall Bar (b) Offset Hall Bar (c) Edge Hall Bar

Figure 5.1: Microscope images of three samples consisting of a Pt/Co/Pt Hall bar (centre, brown) with differing lateral offsets with respect to the two electrical contact pads (left and right, cream) upon a Si substrate (background, grey).

Hall bar position	Centre	Itermediate	Edge
XRR total thickness (nm)	5.0	5.1	5.0
Resistance (Ω)	340 $\pm$ 10	330 $\pm$ 10	350 $\pm$ 10
MOKE coercive field (Oe)	37 $\pm$ 2	45 $\pm$ 3	39 $\pm$ 2

Table 5.1: Sample parameters for each of the three samples used within this chapter. The following section details why only the total thickness can be obtained from XRR measurements, compared to the thickness of each individual layer.

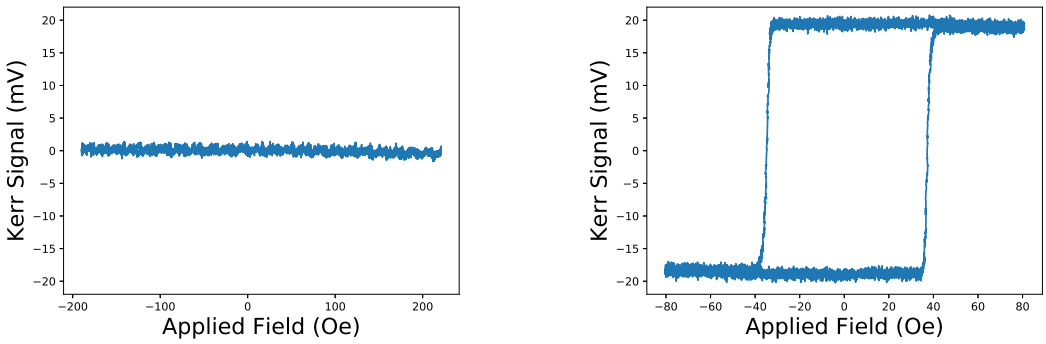

(a) Longitudinal MOKE Measurement (b) Polar MOKE Measurement

Figure 5.2: (a) Longitudinal and (b) Polar MOKE measurements showing hysteresis loops for the in-plane and out-of-plane applied fields respectively, demonstrating a clear perpendicular magnetic anisotropy resulting in an out-of-plane easy axis for the Pt/Co/Pt structure.

5.2.1 Structural characterisation - X-ray reflectivity

XRR measurements were performed on unpatterned samples using a Bede D1 reflectometer before being modeled using GenX, both of which are described in chapter 3. The interference pattern generated is a result of reflected waves from film interfaces and is suitable for thin film thicknesses above approximately 5 nm [113]. The sample used within this chapter has a total thickness of 5.6 nm with sublayers as thin as 0.6 nm. While the total thickness should be measurable, the sublayers are too thin to reliably measure the density profile. Nevertheless, the XRR measurement is presented in figure 5.3 together with four chosen models used for fitting.

First, a single layer model is used which produces a good quality fit. The associated scattering length density (SLD) profile shows a film with a density that is approximately equal to that of Pt and a total film thickness of 4.9 nm. Although slightly less than the expected 5.6 nm thickness, this small discrepancy can be attributed to growth rate calibration errors and is expected. Secondly, a bilayer model is presented which shows a marginally improved level of fit. A small decrease in SLD is observed between z = 0 - 2 nm which is consistent with the presence of Co, since the SLD for Co is half that of Pt. However, no clear Co layer is observed. Finally, moving to a three layer model, marginal fitting improvements are obtained, yet with increased ambiguity. This model provides evidence of the inverse phase problem, briefly discussed in chapter 3, whereby comparable fits have been obtained for two different SLD profiles, namely one with an increased SLD and a second with a decreased SLD in the region of 0 - 2 nm.

Overall, all fits provide an average total thickness of 5.0 nm at a SLD value

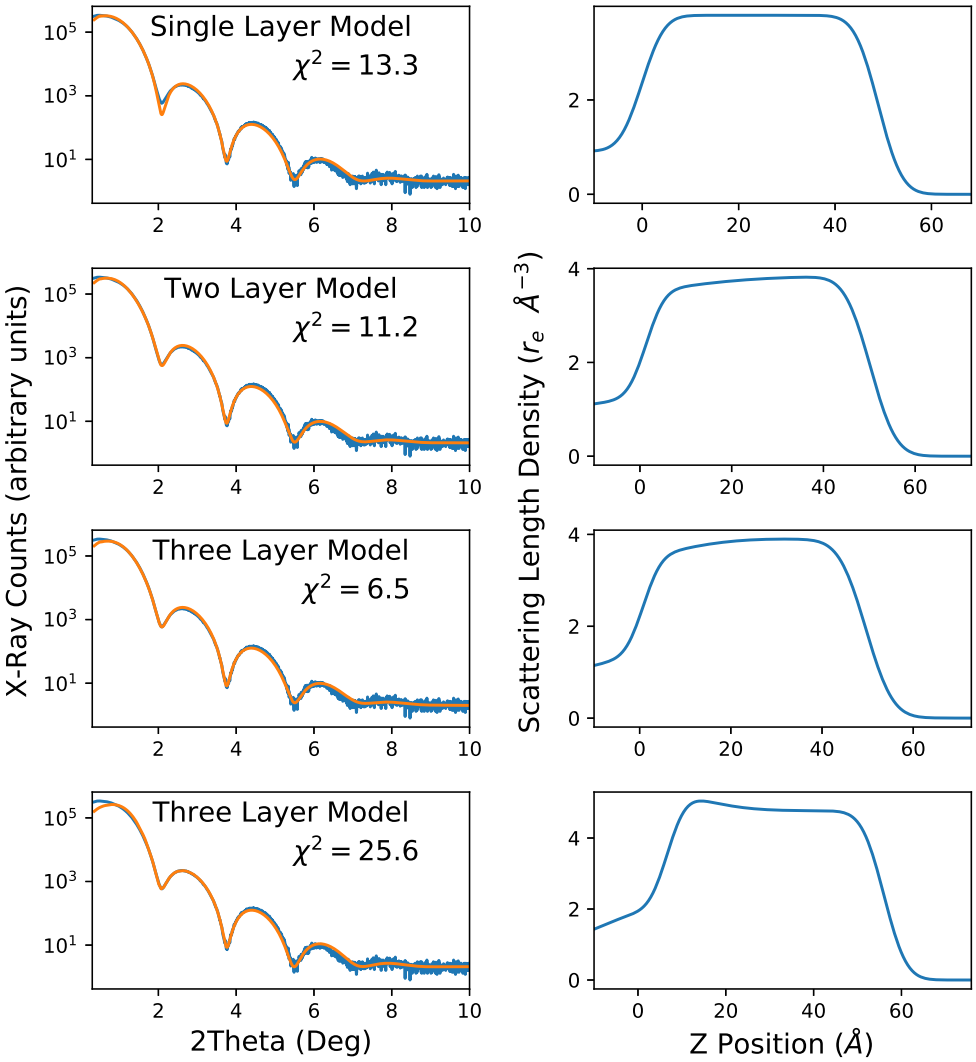

Figure 5.3: XRR data (blue, left) for the pt/Co/Pt structure, together with four unique models (orange, left) and their respective scattering length density profiles (right). From top to bottom, the models are; single layer, bilayer, trilayer with a density decrease and trilayer with a density increase. Reduced Chi squared values are presented for each fit, which are dominated by the discrepancies seen at high intensities (low angles).

comparable to that of pure Pt, along with evidence of small SLD variations at approximately where expected for the Co layer. As the samples also behave as expected magnetically, confidence can be placed in the trilayer structure.

5.2.2 Sample heating

Initial measurements were performed in order to estimate the experimental parameter limitations, including the maximum amplitude of the applied electrical current without causing irreversible damage. An identical sample to that shown in figure 5.1(a) was subject to repeated current applications of 70 mA ($J_c = 7 \times 10^{11}\mathrm{Am}^{-2}$) for 20 seconds, followed by a 1 second application some time later. The current is assumed to propagate uniformly throughout the Hall bar, hence, the cross section used for the conversion to current density is 20 μm $\times$ 5 nm. Optical reflectivity measurements were taken during the application of both current pulses. Sixty measurements were performed in total where the 1 second current pulse was delayed in multiples of 3 seconds with respect to the 20 second pulse, as shown in the lower frames of figure 5.4.

The data shown indicates that the reflectivity changes under the application of an electrical current, and when such current is turned off, that the reflectivity decays

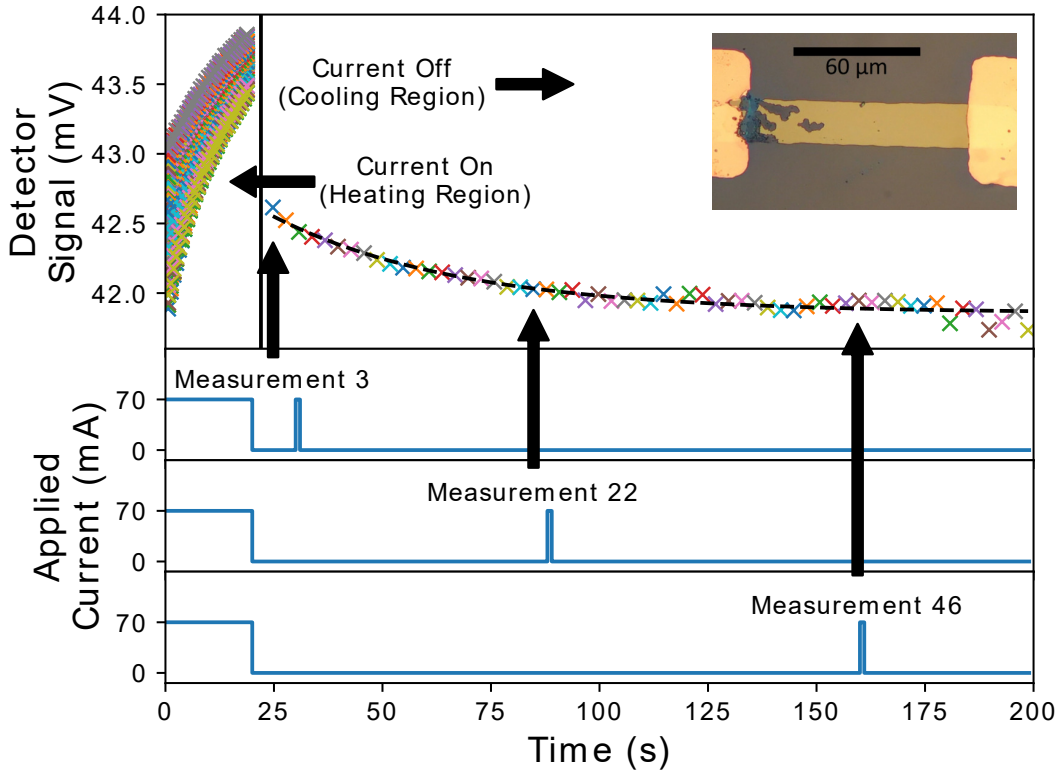

Figure 5.4: Laser reflectivity of a Hall bar element during a heating (0 - 20 seconds) and cooling (20+ seconds) cycle. The current was only applied during measurements, as displayed in the lower half of the figure. The inset shows a broken sample after the application of a high current density. During all measurements the laser spot was positioned centrally upon the Hall bar with a spot size of approximately 20 μm.

back to the original value. The MOKE system includes a photocurrent amplifier with the capability of applying a DC offset. As such, the zero photocurrent value for this measurement is 700 mV and increasing light values creates a more negative detector signal, before saturating at -4700 mV. Therefore, during the first 20 second current application, the detector signal change from 42.5 mV to 43.6 mV corresponds to a reflectivity reduction of 0.15 %.

Thermoreflectance is widely used for the development and testing of semiconductor devices [114–116]. For small temperature changes, the relationship between the fractional reflectivity change, $\Delta R/R$, and the temperature change, ΔT, is given by [117],

$$\frac{\Delta R}{R} = C_{\mathrm{TR}} \Delta T, \tag{5.1}$$

where C_{TR} is the thermoreflectance coefficient. For Pt at room temperature illuminated by light of wavelength 658 nm, $C_{\mathrm{TR}} \approx -5.5 \times 10^{-5}\ \mathrm{K}^{-1}$ [118].

The sample temperature decay profile can be estimated by modeling the temperature with Newton's law of cooling. This law states that the temperature, T, at a time t is,

$$T(t) = T_{\mathrm{env}} + (T(0) - T_{\mathrm{env}}) \exp \frac{-t}{\tau}, \tag{5.2}$$

where T_{env} is the temperature of the environment and τ is a time constant relating the mass, heat capacity, surface area and heat flow coefficient. Modifying this law to be in terms of reflectance, R, this becomes

$$R(t) = R_0 + \Delta R \exp \frac{-t}{\tau}. \tag{5.3}$$

This curve can be fit to the cooling region (time greater than 20 seconds) data presented in figure 5.4, which results in a value of $\Delta R = 1.9 \pm 0.2$ mV, or equivalently, a 0.27 % change in reflectivity. Using equation 5.1, this value of ΔR equates to a temperature change of 50 ± 5 K. The author notes that there is a rapid fall off in detector signal in the region of 15 to 20 seconds that is not accounted for within the model. This may be due to thermal equilibrium being reached within a three body model. The primary body may be the volume in the immediate vicinity of thin film, which is being directly Joule heated. This area may transfer heat to a secondary body, namely the remaining wafer volume. Finally, the wafer may lose heat to the

environment, including the sample holder. The rapid fall off may describe the heat exchange between the primary and secondary bodies, while the longer cooling region may describe the heat transfer to the environment. While this is only one possible explanation, presented without any experimental verification, the rapid fall off is noted and should be thought of as a source of error within the final result.

To further validate the temperature approximations, a second experiment upon this sample was undertaken with the application of a 90 mA current ($J_c = 9 \times 10^{11}\mathrm{Am}^{-2}$). Unfortunately, during this experiment the sample burnt out and is shown in the inset of figure 5.4. As thin films are regularly annealed at high temperatures without destruction [119–121], it is thought that the local temperature of the sample at the point of burn out would have been much greater than 50 K above room temperature. Therefore, the estimation of a 50 K temperature rise during the 70 mA application should be considered a lower bound. The cause of such a sample burn out may be due to electro-migration. This process occurs at high current densities and describes the momentum transfer from the electrons to the host atoms. If the momentum transfer is great enough, atoms can be displaced in the direction of the current flow. If enough atoms are displaced, this can create a void within the conductor, similar to that shown in the inset of figure 5.4. Electro-migration often comes with local heating due to the large current densities, however, it can occur at temperatures which are lower than the maximum possible annealing temperature.

Further validation of the temperature bound calculation comes from comparison to literature, whereby Torrejon *et al.* report a calculated temperature increase of between 50 K and 230 K within their investigation, albeit for smaller NiFe structures with nanosecond current pulses and higher current densities [122]. Nevertheless, a temperature increase of greater than 2.5 K/s under the application of 70mA is still significant and should be avoided where possible. This temperature increase is likely to be in-part localised to the metallic thin film, with significant heat flux into the substrate rather than laterally across the sample [123].

Taking these current amplitude and application time limits into account, the following section details the current-induced magnetic reversal results for a Hall bar situated in the centre of the electrical contact pads.

5.3 Hall bars with transverse structural symmetry

5.3.1 Field and current dependence of current-induced magnetic reversal

Current-induced magnetic reversal of an out-of-plane magnetised sample can be demonstrated through the use of an in-plane applied magnetic field together with a charge current. This in-plane field is parallel to the applied charge current. Experiments typically take one of two forms; measurement with DC field and pulsed charge-current, or DC field and continuous AC charge-current. Figure 5.5 shows the mean polar Kerr remanence as a function of DC magnetic field and applied AC charge current. This measurement was performed on a Hall bar sample situated in the centre of electrical contacts, as shown previously in figure 5.1(a). The charge current is varied from 0.83×10^{11} Am^{-2} to 3.75×10^{11} Am^{-2} (10 mA to 45 mA) and applied over a period of 8 seconds with 3 repeats at each point, totaling 38 repeat measurements. Following the previous sample heating discussion, it is estimated that the sample temperature rises by a minimum of 10 K above room temperature during each current application.

Prior to each individual in-plane applied field and charge current measurement (H_{app} and J_{c}), a polar field Kerr measurement is first performed in the absence of J_{c}. This measurement acts to determine the Kerr signal voltage corresponding to positive and negative magnetic saturation. Immediately after the polar measurement, both H_{app} and J_{c} were applied and the current-induced magnetic reversal Kerr measurement was recorded. Figure 5.5 then compares such measurements, producing a 2-D plot of the ratio of current-induced to polar field remanence (left) from each individual measurement (right).

Figure 5.5 shows the expected form of current-induced switching [124, 125]. In particular, no switching is observed below the sample specific threshold values (white), with deterministic switching being observed above such a threshold (red and blue areas). For positive (negative) remanence ratios, this threshold extends from approximately (-)200 Oe and 0.83×10^{11} Am^{-2} to (-)10 Oe and 2.00×10^{11} Am^{-2}. The boundary is approximately linear, consistent with other studies [124–126]. When the applied field direction is reversed, the acquired hysteresis loop is also reversed as a consequence of the deterministic switching.

It was noted that the width of the threshold region is on the order of 30 Oe for a constant current density. Although this is likely attributed to random fluctuations within the magnetic reversal process, there are suggestions to which this can be evidence for an intermediate switching state [126]. This state is a prod-

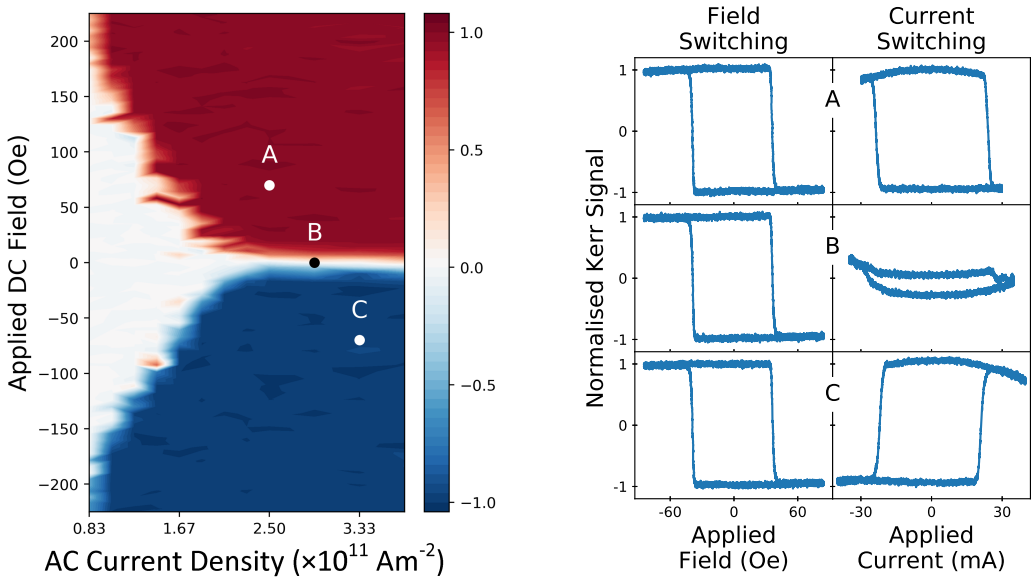

(a) 2D remanence Map

(b) Example hysteresis loops

Figure 5.5: (a) Switching map showing the dependence of Kerr hysteresis remanence values upon the AC current density amplitude and applied in-plane DC magnetic field. (b) Example hysteresis loops for the polar field switched Kerr measurement (left) taken immediately prior to each current-induced magnetic reversal measurement (right) at three points (A, B, C) within the switching map.

uct of non-zero Dzyaloshinskii-Moriya interaction and can produce textures such as chiral stripe domains and skyrmions. To investigate the threshold region further, the following section investigates any spatial dependence upon the current-induced magnetic reversal.

5.3.2 Position dependence, as measured by polar MOKE

The laser spot size for the MOKE instrument is approximately 15 μm in diameter at its best focus. Assuming that the laser spot intensity profile is approximately Gaussian, any measured MOKE signal is the summed response of a 15 μm diameter circle with a Gaussian spatially weighted distribution. Although the laser spot can be raster scanned across the sample at a much higher step-size resolution (less than 1 μm), the final resolution is ultimately dictated by the laser spot size. Nevertheless, modeling of such output can improve the effective spatial resolution and provide further insight into the domain structure.

Figure 5.6(a) shows a microscope image of the sample, which is also the sample used in the previous section. Figure 5.6(c) shows the average signal acquired during many raster scanned MOKE measurements which resembles that of figure 5.6(a),

albeit blurred due to the laser spot size. The remanence of standard polar field MOKE measurements is shown in figure 5.6(b) which shows uniform and unidirectional Kerr remanence. The spatial extent is approximately 20 μm by 100 μm, as expected from the Hall bar dimensions. From this, it is reasonable to conclude that the entire Hall bar is both ferromagnetic and exhibits spatially uniform perpendicular magnetic anisotropy. The coercive field is equal across the entire Hall bar (not shown), with hysteresis loops identical to that shown previously in figure 5.5.

At each raster scan position, a field-free current-induced magnetic reversal measurement was also performed with $J_c = 2.9 \times 10^{11}\,\mathrm{Am}^{-2}$ (35 mA). The remanence of

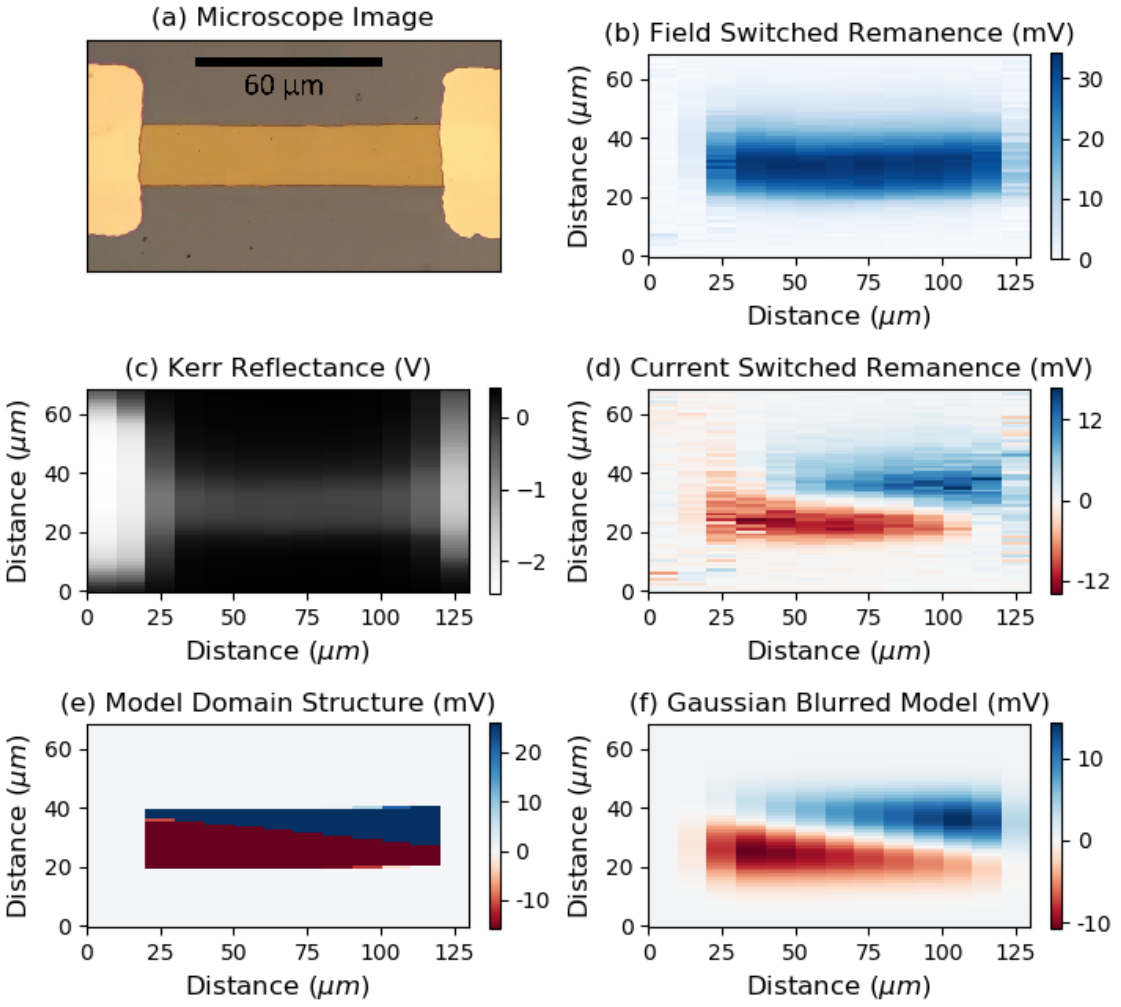

Figure 5.6: (a) Optical microscope image of the sample with a centred Hall bar. (b) The MOKE response from polar magnetic field-induced reversal. (c) The reflectance of the, showing the dullest part of the sample is the substrate, with the thin film structures being more reflective, as expected.(d) Field-free current-induced magnetic reversal, together with a higher resolution model of the remanence before (e) and after (f) induced Gaussian blurring due to the laser.

each measurement is shown in figure 5.6(d) and, contrary to the polar field MOKE measurements, bidirectional reversal with a spatial dependence is observed. These results are averaged over 64 charge current cycles and, therefore, are a result of deterministic switching rather than statistical fluctuations from the likes of thermal fluctuations and random domain nucleation. A best fit model was developed in order to fit a domain structure to the data presented in figure 5.6(d). The result of which is presented in figures 5.6(e) and 5.6(f) for the pre- and post-Gaussian blur models respectively.

Before analysing the result of the best fit model, it is worth stating that this model has some limitations. The presented model is limited to two domains with a linear domain boundary of infinitesimal width. The effects of domain walls, including the type of domain walls, are on length scales significantly beyond the resolution of this analysis and are, therefore, omitted. It is highly likely that many different domain structures can give a Gaussian blurred model that approximately matches the data. After a visual inspection of the raw data in figure 5.6(d) and considering Occam's razor, the model of two domains with a linear boundary has been employed over more complicated models at this stage. It is noted that the model Hall bar (figure 5.6(e)) has a small angular offset with respect to the reflectance (figure 5.6(c)). A model with a fixed angle of 0 degrees with respect to the horizontal was also employed, which more closely visually resembles the reflectance. This model produced remanence regions that were visually indistinguishable to those presented in figure 5.6(e), yet with a 3 % increase in the chi-squared metric. It is thought that the interplay between having a narrow remanence region in the top left/bottom right corners and the Gaussian blur creates a small preference in favour of an angled Hall bar when characterised by a chi-squared figure of merit. Nevertheless, as both the free and fixed angled models produce visibly indistinguishable solutions, this small angle is noted but ultimately neglected from further analysis.

The magnitude of the Kerr signal remanence within the model is -14 mV and 18 mV for the negative and positive domains respectively. This is significantly smaller than the field switched remanence of 30 mV, which is likely to be as a result from an incomplete model which lacks partial and/or inconsistent switching. For example, the model presents a uniform region with a positive remanence of 18 mV. This value can also be achieved with a multidomain model which consists of randomly spaced areas of 30 mV signal and -30 mV, with overall spatial proportions of 4:1 respectively. Assuming these regions are smaller than the laser spot size, this would spatially average to the constant 18 mV signal displayed by the model shown in figure 5.6(e). Also, an 18 mV signal can be achieved where switching only occurs

60 % of the time, where a 30 mV signal is observed when switching is complete and 0 mV otherwise.

While considering the limitations of the model, there are still some significant conclusions that can be drawn from this data. Firstly, field-free magnetic reversal has been shown within a sample that does not employ any of the reported approaches to symmetry breaking. Secondly, deterministic bidirectional reversal exists in a single Hall bar element. To probe the nature of such switching mechanism, it is useful to define the characteristics of the spatially-dependent remanence.

1. The structure can be reasonably modelled by two regions which exhibit deterministic switching in opposite directions.

2. There exists a dominant, approximately diagonal domain boundary along the length of the Hall bar.

The next section seeks to confirm this bidirectional switching using Kerr microscopy and further build a defining set of characteristics for the field-free magnetic reversal.

5.3.3 Position dependence, as measured by Kerr microscopy

To confirm the results shown in the previous section, Kerr microscopy was performed upon the same sample. Figure 5.7(a) shows the sample under a uniform, positive DC out-of-plane saturating field. After reversing the magnetic field in figure 5.7(b), the contrast of the image changes to indicate the entire Hall bar has reversed magnetisation, as previously shown with the field switched Kerr remanence.

The Hall bar is then returned to a saturated positive state before being subject to a 2 second pulse of 35 mA ($2.9 \times 10^{11}\mathrm{Am}^{-2}$). The resulting magnetic domains, shown in figure 5.7(c) and (d) for opposite charge current directions, are consistent with the previous results in that they show partial switching. In both cases, the domain wall appears to be approximately linear with endpoints in the middle of one end of the Hall bar and the corner of the opposing end.

Experiments were also performed starting from a negative saturation state. These results (not shown) are qualitatively similar to those in figure 5.6, yet with opposite polarity. A positive current now switches a region in the top right, akin to figure 5.6(d) yet with magnetic reversal in the opposite direction. A negative current switches a region in the bottom left, akin to figure 5.6(c), also with opposing direction.

These results give further insight into the possible domain structure during current-induced magnetic reversal. There exists a diagonal region along the length

of the Hall bar that appears to be unmodified by any charge current. In figure 5.7, this region is approximately defined by the area inside the four Hall bar positions marked with black dots.

Using this knowledge, we can add a third characteristic that any possible theory must satisfy.

1. The structure can be reasonably modelled by two regions which exhibit deterministic switching in opposite directions.

2. There exists a dominant, approximately diagonal domain boundary along the length of the Hall bar.

3. A diagonal stripe across the length of the Hall bar may not undergo magnetic reversal.

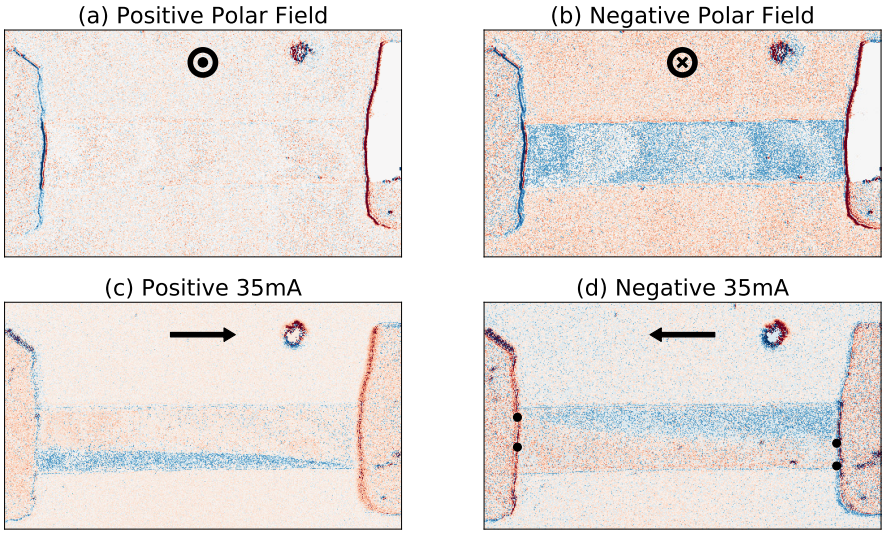

Figure 5.7: Kerr microscopy images for polar field-induced magnetic reversal (top) and field-free current-induced magnetic reversal (bottom). Blue and red contrast indicate domains of opposite polarity. A region that does not undergo magnetic reversal under either positive or negative currents is highlighted with 4 dots within the negative 35 mA image. Due to small misalignment's of the image between measurements, edges, such as those around the electrical contacts, falsely show a small amount of red/blue contrast. This contrast is not a magnetic effect and could be removed with a more rigid microscopy setup.

5.3.4 Further position dependence modelling

Previously, a model consisting of two remanence regions was used to reproduce MOKE data under the argument of Occam's razor, which provided a good level of fit. After the previous Kerr microscopy results, it is now worth returning to this model with the addition of a neutral region. Figure 5.8 shows such a model, where a region of zero remanence is inserted in-between the positive and negative remanence regions. The Gaussian blurred model is visually indistinguishable to the previous two region model, yet the base model shows a significant zero remanence region. In addition to the magnitude of each remanence region, the position of both the upper and lower boundary of the zero remanence region is a free parameter within the fitting process. This allows the size and orientation of the zero remanence region

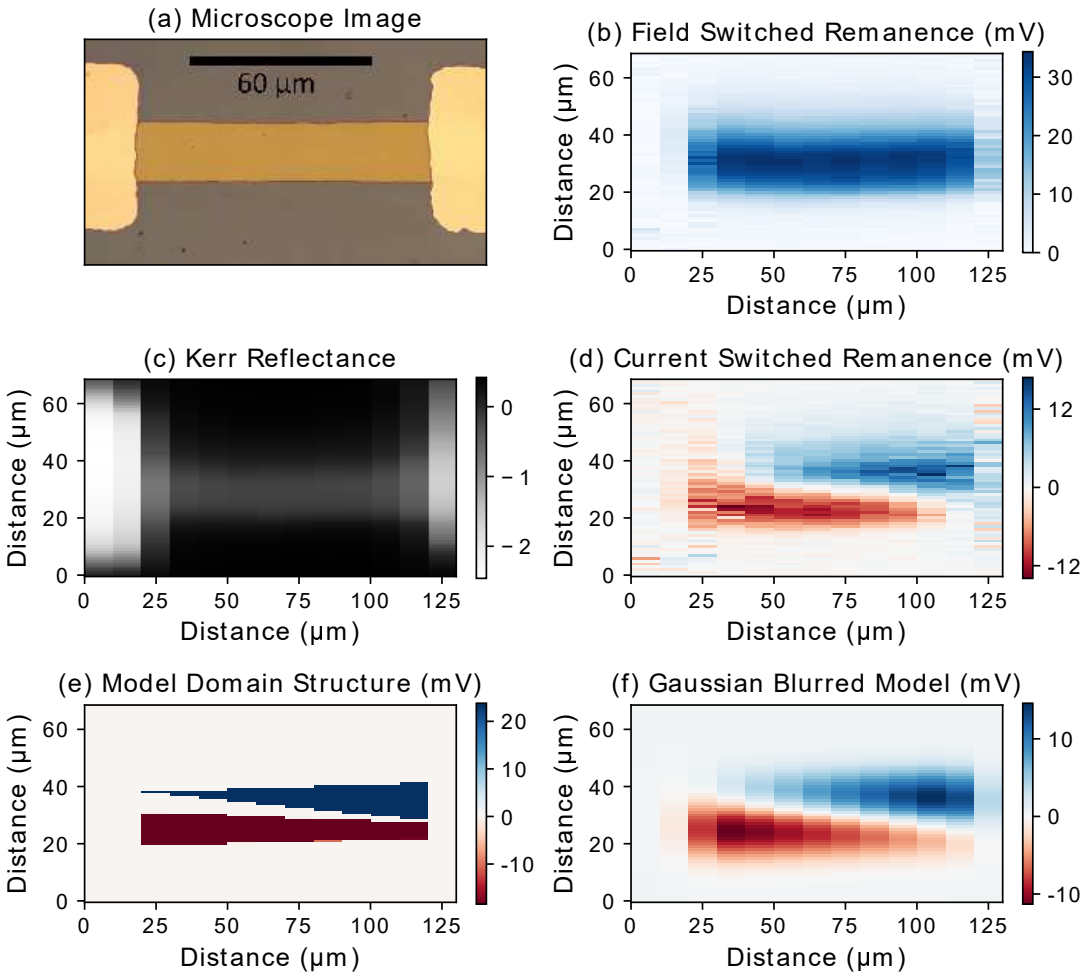

Figure 5.8: (a) and (c) Images of the centred Hall bar structure. MOKE remanence measurements, (b) and (d), together with an advanced model of two remanence regions of opposite polarity separated by a region of zero remanence (e) and (f).

to be optimised in order to minimise the figure of merit. After such optimisation process, the results are fairly consistent with the Kerr microscopy data. The positive remanence region (blue) has vertices at the Hall bar corner on the left hand side, and approximately the Hall bar midpoint on the right hand side. The negative region (red) also has a vertex on the Hall bar midpoint (left hand side), yet the opposing vertex is displaced from the Hall bar corner. Again, it is worth noting that the model resolution is significantly higher than that of the data, therefore, some discrepancies are to be expected during fitting procedures.

Both the original and improved models replicate the data well, therefore, both should be retained as possible explanations. The Kerr microscopy results, however, are more consistent with the improved model, hence this model should be preferred. As this model only corroborates the previous characteristics and does not necessarily show anything new in comparison, a fourth characteristic defining the behaviour cannot be added. The following section investigates the effect of lateral Hall bar translations upon the field-free magnetic reversal.

5.4 Hall bars with transverse structural asymmetry

5.4.1 Small (10 μm) lateral displacement

Other studies of similar materials and Hall bar geometries have generally included electrical contacts of comparable dimensions to the Hall bar [96, 97, 103–105]. Here, the electrical contacts are three times wider, hence they may have an involvement in the observed field-free magnetic reversal that would otherwise be absent in other studies. To investigate this, the Hall bar was displaced laterally by 10 μm with respect to the electrical contacts, as shown in figure 5.9(a). An identical MOKE raster scan procedure was employed to that previously, for which the results are shown in figures 5.9(b) to (f). The field switched remanence and Kerr reflectance both indicate that the Hall bar is complete and has uniform magnetic parameters. The remanence value of 16 mV is lower than the 30 mV value measured for the previous, centred Hall bar. This is thought to be a consequence of slight differences in the optical laser beam path, which is common in MOKE instruments, rather than any significant sample parameter changes. Hysteresis loop coercivity values are approximately 40 Oe, equal to that of the centred Hall bar.

Figure 5.9(d) shows the field-free current-induced magnetic reversal remanence, which shows a distinct region in which there is a non zero remanence. This region is much thinner than that observed for field-induced switching, indicating that the Hall bar only partially reverses. Modeling this data indicates that the top 50 % of

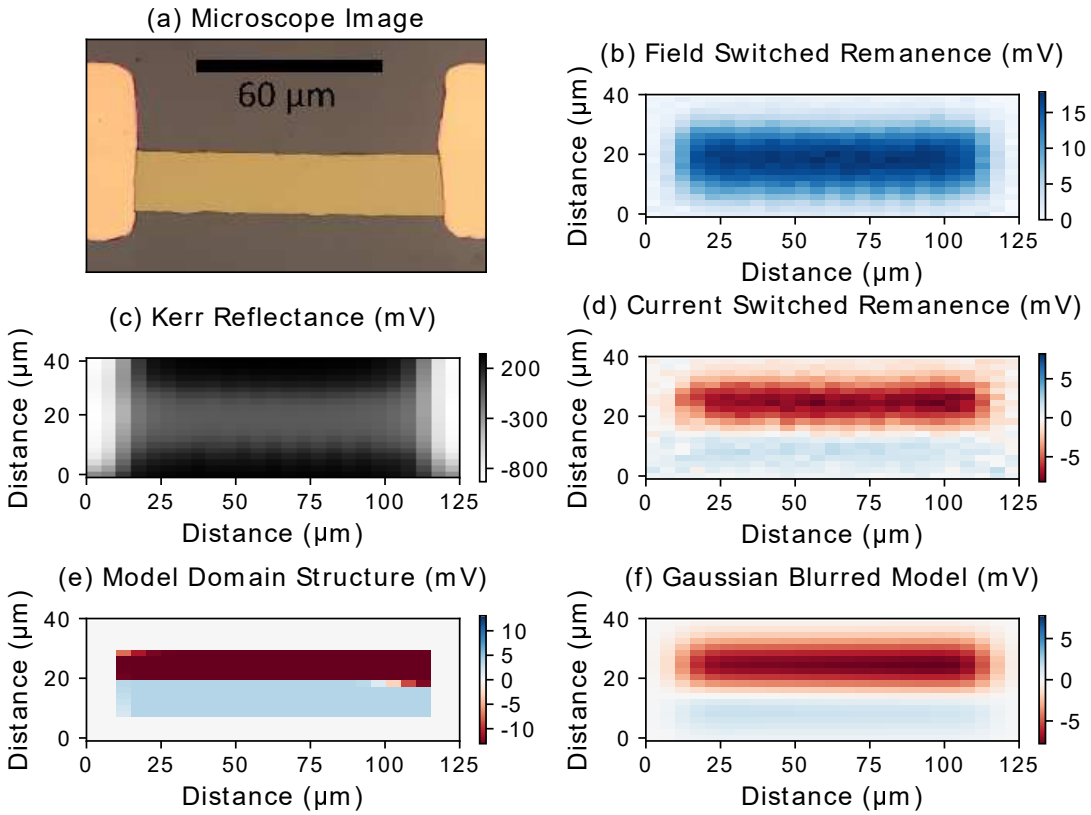

Figure 5.9: (a) and (c) Images of the Hall bar with a small lateral displacement with respect to the electrical contact pads. MOKE remanence data for polar field-induced reversal (b) and field-free current-induced magnetic reversal (d), together with the associated best fit model (e) and (f).

the Hall bar has a negative remanence of 13 mV, marginally smaller in magnitude than the average value of 16 mV for the field-induced reversal. There exists a significant asymmetry between positive and negative remanence regions, with the positive (blue) region showing a Kerr signal voltage of 3.8 mV. As this data is averaged over 64 field cycles, it is not possible to distinguish between the causes of this disparity, in particular if this is from complete yet inconsistent switching, or incomplete but consistent switching.

Interestingly, the boundary between positive and negative remanence regions is parallel to the Hall bar edges, compared to diagonal in the case of centred Hall bar. The model also predicts a negligible zero remanence region, although, due to the reduced magnitude and limited spatial extent of the positive remanence signal within the data, this feature is particularly susceptible to noise and is, therefore, potentially unreliable. The previously introduced characteristics that any explanation must satisfy can now be modified to include such changes.

1. The structure can be reasonably modelled by two regions which exhibit deterministic switching in opposite directions.

2. These regions may differ in magnitude, with the region closest to the electrical contact midpoint favouring larger magnitudes.

3. There exists a dominant domain boundary, possibly parallel or diagonal, along the length of the Hall bar.

4. There may be a portion of the Hall bar, situated between positive and negative remanence regions, that does not undergo magnetic reversal.

5.4.2 Large (20 μm) lateral displacement

Finally, a sample with the Hall bar situated at the very edge of the electrical contacts has been investigated using an identical raster scanning MOKE approach. The results shown in figure 5.10 are very similar to those presented previously for the Hall bar with a small lateral displacement. In particular, a region of greater remanence magnitude is shown in the upper portion of the Hall bar, with the lower portion displaying a weak remanence signal of opposite polarity. These regions are also separated by a linear boundary parallel to the Hall bar edges, with a negligible zero remanence region in between.

Uniquely, the larger region of negative remanence now covers approximately 75 % of the Hall bar, compared to 50 % or lower previously. The average remanence value is -7.2 mV, compared to 3.4 mV for the smaller (blue) positive remanence region, providing further evidence of a dominant magnetic reversal region closest to the electrical contact midpoint. As is now consistent across all Hall bar structures, the magnitude of current-induced switching remanence is below the field-induced remanence value of 13 mV.

The characteristics that any theory must describe are now complete, with the new addition of remanence region size.

1. The structure can be reasonably modelled by two regions which exhibit deterministic switching in opposite directions,

2. These regions may differ in magnitude *and size*, with the region closest to the electrical contact midpoint favouring larger magnitudes/greater size,

3. There exists a dominant domain boundary, possibly parallel or diagonal, along the length of the Hall bar,

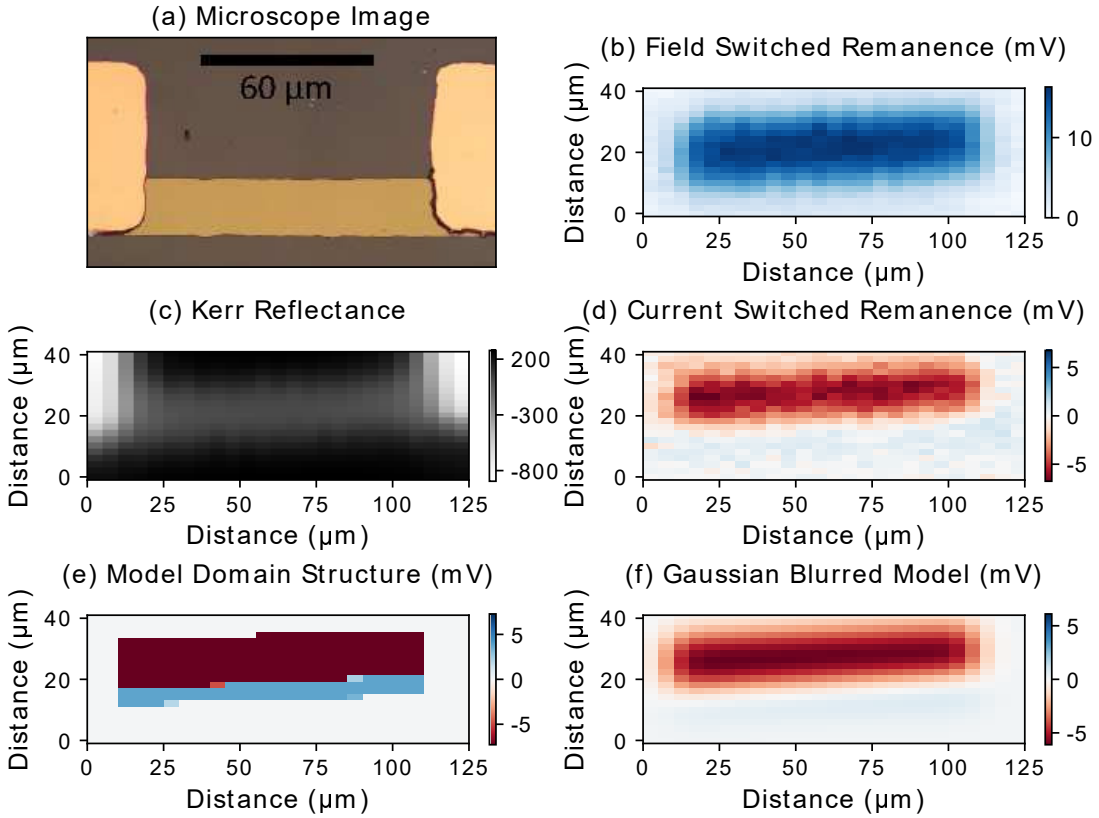

Figure 5.10: (a) and (c) Images of the Hall bar with a large lateral displacement with respect to the electrical contact pads. MOKE remanence data for polar field-induced reversal (b) and field-free current-induced magnetic reversal (d), together with the associated best fit model (e) and (f). The microscopy image (a) was taken using a separate instrument, hence, any angular offset between figure (a) and the remaining figures is due to different mounting angles.

4. There may be a portion of the Hall bar, situated between positive and negative remanence regions, that does not undergo magnetic reversal.

In the following sections, several explanations for the above results are explored and measured against the defined criteria. These include mechanisms that have been previously documented in the literature, together with new theories.

5.5 Interpretation of the electrical contact dependency

For external field-free magnetic reversal of perpendicularly magnetised ferromagnetic layers, there must exist some form of symmetry breaking to allow for deterministic

switching [102]. There exists a number of methods that have already achieved this, some of which can be excluded immediately, in particular the methods of biased antiferromagnets and piezoelectric substrates. A third method of spin currents with out-of-plane polarisation can also be discounted. However, it should be noted that this method is beyond the current understanding of spin-orbit torques [23]. To achieve magnetic reversal with spin currents of out-of-plane polarisation, three approaches have been followed including the use of ferromagnetic/heavy metal bilayers [25, 26], heavy metal/heavy metal bilayers of opposing spin Hall angles [23] and materials with broken lateral surface symmetries [24]. As the Pt/Co/Pt trilayer studied here bears no resemblance to these three methodologies, and it has been widely studied in literature with no mention of out-of-plane spin currents [96, 97, 99, 100], out-of-plane spin currents can be ruled out as the cause of the aforementioned results.

Excluding these three methods leaves the possibility of structural gradients, SOT-driven domain wall motion or a new explanation. The following pages aim to explore the remaining two methods and introduce a possible new method involving current crowding and the Oersted field. These methods are measured for consistency with the results shown by way of comparison to the four previously determined characteristics.

1. The structure can be reasonably modelled by two regions which exhibit deterministic switching in opposite directions.

2. These regions may differ in magnitude and size, with the region closest to the electrical contact midpoint favouring larger magnitudes/greater size.

3. There exists a dominant domain boundary, possibly parallel or diagonal, along the length of the Hall bar.

4. There may be a portion of the Hall bar, situated between positive and negative remanence regions, that does not undergo magnetic reversal.

5.5.1 Structural gradients

There exists two types of structure consisting of some form of gradient, referred to as structures with internal or external gradients. External gradients consist of structures in which layers have differing lateral extents. For example, You *et al.* use a trilayer structure of Ta/CoFeB/MgO, yet the top MgO layer does not completely cover the CoFeB layer, therefore, leaving a region of Ta/CoFeB bilayer [110]. Internal gradients describe structures which have consistent lateral dimensions across all layers, yet vary in thickness, or another parameter, across the layer.

All samples were fabricated on separate wafers. When depositing the structure, the wafer substrate table was rotated throughout deposition in order to remove any directional dependence with respect to the sputtering source. The samples were mounted onto the substrate table approximately 1 cm apart, which is much smaller than the nominal uniform deposition region for this particular system of 5 cm diameter.

External gradients

The Hall bar was produced through a standard deposition and lift-off lithographic process. A single layer resist was used, for which vertical walls and no undercutting was expected. After lithographic patterning, the entire trilayer structure was deposited sequentially, without breaking the vacuum of the deposition system or performing any intermediate lithographic steps. It is then reasonable to expect a clean Hall bar edge, as opposed to a shallow gradient that would be consistent with undercutting. This is consistent with the optical microscope images, Kerr microscope images and out-of-plane field-induced MOKE measurements. Figures 5.6, 5.7, 5.9 and 5.10 all show Hall bar structures with defined edges of equal dimensions to the Hall bar (20 μm by 100 μm), together with a uniform perpendicular magnetic anisotropy. This allows for the explanation of external gradients to be discounted.

Internal gradients

It has been shown that the combination of structural gradients and charge current direction can uniquely determine the magnetisation direction [103–105]. To achieve the bi-directional switching observed here during a single charge current application, there must exist two structural gradients of opposing directions. Figure 5.11a shows the gradients required to produce the previous results for the centred Hall bar (top) and those with small (middle) and large (bottom) lateral displacements.

Figure 5.11b shows the coercivity as a function of distance across the bar width for the Hall bar with a small lateral displacement. Although the coercivity is not a direct measure of the anisotropy, it is influenced by the anisotropy, therefore, it can be used as an indicator for any underlying anisotropy changes [127]. The maximum coercivity change of 3 Oe across the width of the Hall bar does not suggest a significant anisotropy change, but rather statistical fluctuations over an isotropic Hall bar. The coercivity profile also does not match what is expected of the structural gradient in figure 5.11a, assuming any anisotropy gradient would produce a similar coercivity gradient [104, 105].

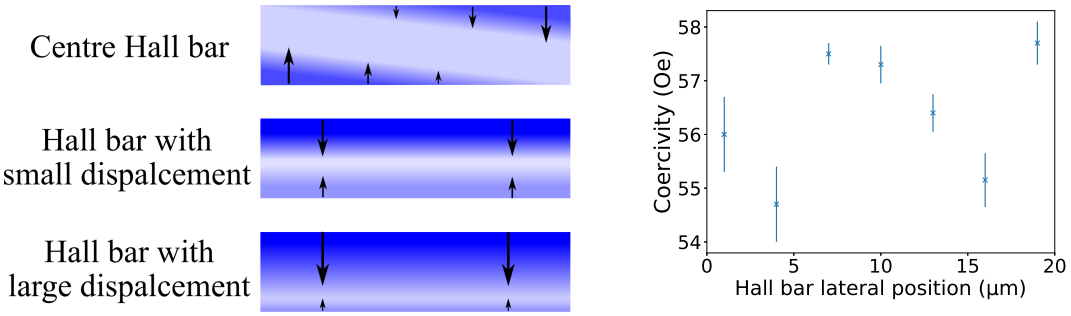

(a) Required structural gradients (b) Coercivity spatial dependence

Figure 5.11: (a) The structural gradients required to reproduce the results shown within this chapter for three Hall bars with different electrical contact positions. Colour and arrow size/direction indicate structural gradients. (b) The average coercivity across the Hall bar with a small lateral displacement, indicating no clear coercivity variations.

Separate XRR studies of larger samples have also been performed with the aim of exploring the consistency of deposition across the substrate. Figure 5.12(a) shows the data and model for a 10 nm Pt thin film on a substrate of 2 cm by 2 cm. A single layer model of 10 nm produces an excellent fit, with a surface roughness of 0.5 nm, typical of sputter deposited thin films on silicon substrates [128]. If there was a wedge present, the specular reflection profile would have a wafer position dependency. To highlight what this would look like, figure 5.12(b) shows the same 10 nm Pt data, yet with a model of 10.5 nm in thickness (all other parameters remain unchanged). Any XRR measurement of a wedge would consist of an average of all of the thicknesses present, which would appear as an increased surface roughness within the model. The model presented in figure 5.12(c) has an additional 0.5 nm of surface roughness compared to the best fit model in figure 5.12(a) (10 nm thickness). As can be seen, wedges consisting of small thickness and/or roughness changes, comparable to what might be anticipated in order to produce field-free magnetic reversal [103–105], would be clearly evident in the measured data, if they were to be present.

As no coercivity variation across the Hall bars, or any structural variations across the Hall bars and/or larger samples were observed, the only remaining possibility is of a local structural (and hence anisotropy) variation that does not impact on the coercivity or long range reflectivity profile. The structure of the sample could vary such that overall the film is of uniform thickness, yet it has local gradient which leaves the coercivity unchanged. Although this cannot be entirely discounted, it is highly unlikely. There was no preference of Hall bar direction during the initial photolithographic patterning with respect to the substrate, hence to obtain structural variations with an axis along the Hall bar in each case is of very low probability.

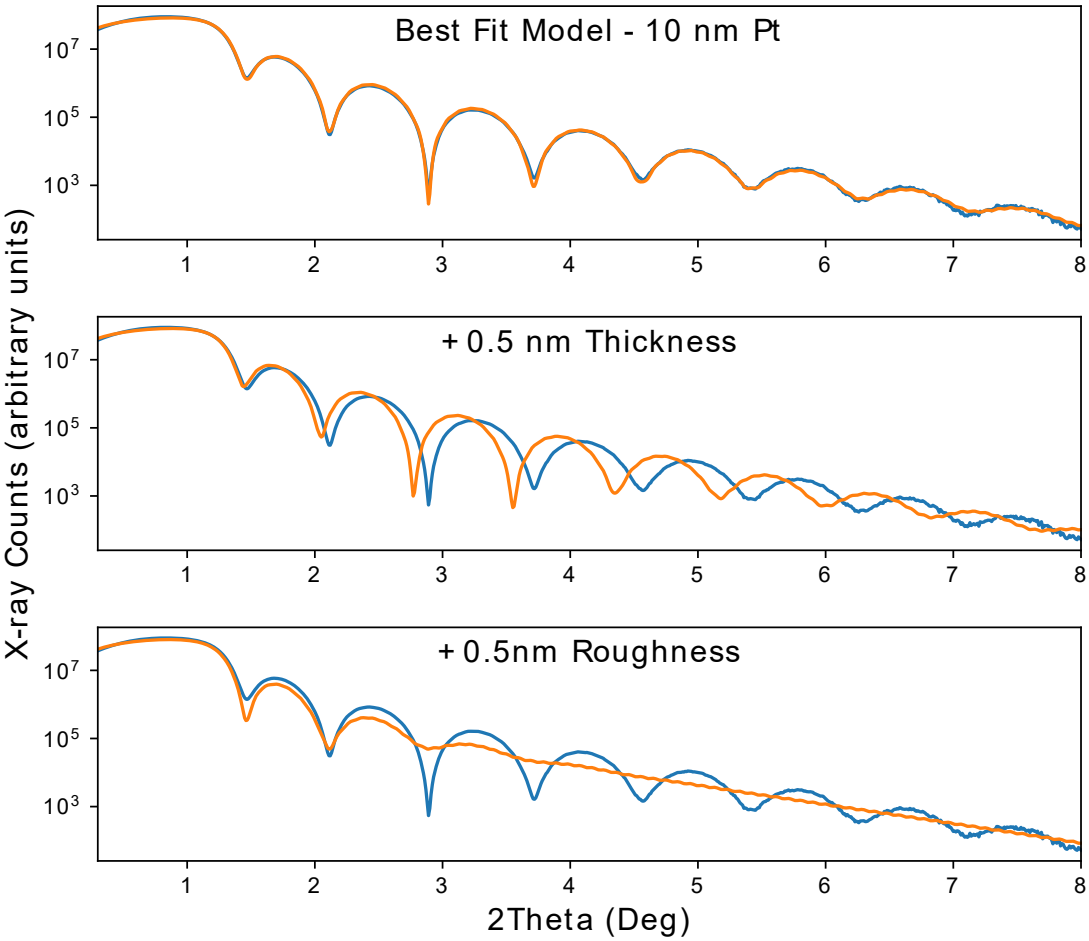

Figure 5.12: XRR data of a 10 nm Pt thin film (blue), together with three models representing the best fit model of 10 nm in thickness and 0.5 nm surface roughness (top), 10.5 nm thickness and 0.5 nm roughness (middle) and 10 nm thickness and 1 nm roughness (bottom).

The presence of exactly two structural variations in opposite directions is again of very low probability.

Another possibility is that of thermal gradients. Thermal gradients can cause variations in strain across the sample, which can influence the magnetic behaviour through magnetostriction. This possibility is discounted for two reasons. First, there is a lack of evidence of significant thermal gradients within Hall bars of similar sizes as to those used here. Instead, it is highly likely that the Hall bar is in thermal equilibrium across its entirety due to the good thermal conductivity of metals and the small overall volume of the Hall bar. Second, Gusev *et al.* conclude that strain only has a minor effect on perpendicularly magnetised Pt/Co/Pt multilayers, unless the Co thickness is chosen to be near the thickness required to transition from in-plane to out-of-plane magnetic anisotropy [129]. If this were true for the samples

used here, the strain induced anisotropy variation would also be present in the conventional switching map shown earlier (figure 5.5). If the magnetic anisotropy, and hence the magnetisation, rotated in-plane due to strain, the direction of the symmetry breaking applied magnetic field would not be correct and no magnetic reversal would be observed. As this is not the case, it can be inferred that no strain induced magnetic anisotropy reorientation is present. These probabilities, together with no evidence of coercivity variations or large scale structural variations, allow for structural variations to be ruled out as the cause of the observed field-free magnetic reversal.

5.5.2 Geometrical domain wall motion

It has been shown that a domain wall motion can be achieved under the application of a charge current [130, 131]. Lee *et al.* have shown that this can produce field-free spin-orbit torque switching [111]. However, as the sample always exists within a multidomain state, a more accurate description is field-free spin-orbit torque domain wall motion. This methodology requires two antiparallel domains, deliberately initialised at opposing bar edges with geometrical domain wall pinning sites, with the domain-wall propagated between such pinning sites when a charge current is applied, creating a central region which switches magnetic states.

As this methodology relies on domain wall motion, it does not work if the sample is initialised in a saturated state. Instead, the sample is initialised in a multidomain state by either advanced sample fabrication techniques [132] or simultaneous current and field applications [111]. The sample fabrication techniques involve creating a bar with differing magnetic properties at each end, allowing for magnetic reversal at only one end under specific conditions. The second method involves applying a DC magnetic field and an increasing current until the sample exhibits a multidomain state, at which point the current and field are removed. The applied field is almost parallel to the charge current, but is tilted out-of-plane by a few degrees.

The Hall bar used here is a conventional rectangular Hall bar and is not designed to display any significant domain wall pinning sites. Before each current-induced magnetic reversal measurement, the Hall bar is initialised in either a positively or negatively saturated magnetic state by a polar magnetic field and no current is applied during this time. This is confirmed by MOKE and Kerr microscopy measurements, indicating a uniform initial state. These observations, combined with the previous section which refutes the possibility of magnetic property gradients, suggest that it is highly unlikely that the magnetic reversal results presented here are as a result of domain wall motion alone. Instead, it is likely that after an

initial domain is nucleated through a different mechanism, switching can continue by domain wall motion. As domain wall motion alone cannot explain the initial change from uniform magnetisation to multidomain, another explanation is needed.

5.5.3 Current crowding and Oersted fields

As the previous discussions of known methodologies for field-free magnetic reversal did not match the presented results, a new theory is required. It is proposed that the Oersted field is the cause of the initial magnetic reversal, made possible by current crowding in the electrical contacts. It is thought that, as the charge current transitions from electrical contact to Hall bar, the current distribution can create a magnetic field that is both strong enough and is in a direction as required to break the symmetry, allowing for deterministic reversal. After the initial reversal, domain expansion occurs via current-induced domain wall motion.

While the charge current spatial profile has not been explored in a spin-orbit torque context within the literature, it has been widely studied in other fields [133–137]. Studies have been performed on generic thin film contacts, to which the resultant current profile depends upon a variety of parameters, including contact and Hall bar thickness and resistivity, along with the interface area and resistivity [134]. To compare results with our system, the conductivities of various elements need to be estimated. To a first approximation, the Hall bar can be thought of as a 5.5 nm thick Pt thin film, for which the resistivity is expected to be around 40 $\mu\Omega$ cm [138]. Using a length and thickness of 100 μm and 5.5 nm respectively, this equates to a resistance of 360 Ω. For the copper electrical contacts, the resistivity at 50 nm is approximately 3 $\mu\Omega$ cm [139], corresponding to 4.8 Ω for our electrical contact configuration. The total, Hall bar dominated, expected resistance of 368 Ω is in good agreement to the measured value of 340 $\pm$ 10 Ω for the centred Hall bar.

Zhang *et al.* provide various examples of the effect of varying individual parameters on the current profile [134]. Two simulations, which are most appropriate to the sample parameters here, are reproduced in figure 5.13(a,b). Zhang *et al.* conclude that increased current crowding can be a consequence of a decrease in contact/Hall bar interface resistance, contact thickness or contact resistivity. As Pt films do not readily oxidise, the interface resistance between the Pt Hall bar top and the Cu contact is expected to be no greater than the adjacent Pt and Cu thin film layers. This, together with the fact that the resistivity of the Cu contact is an order of magnitude lower than that of the Hall bar, suggests there is a significant probability of current crowding occurring within the sample used here. It is also reasonable to suggest that the locally increased current density contributes to increased Joule heating at this

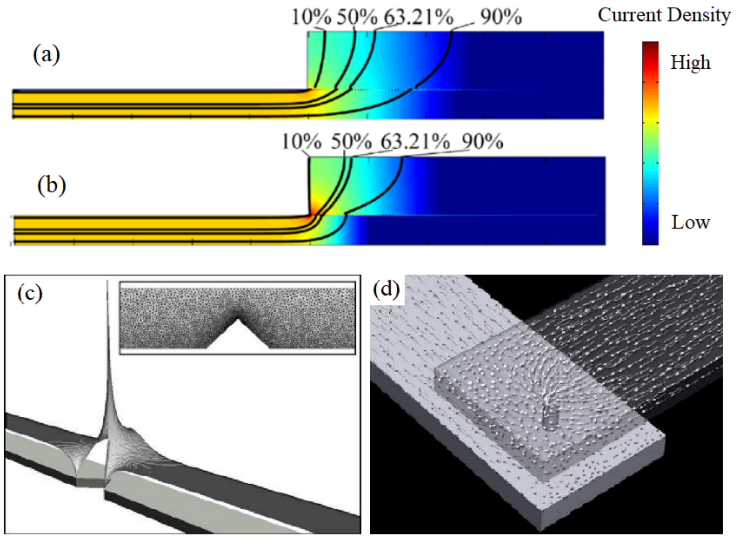

Figure 5.13: Simulations of current crowding in vertical slices of electrical contact geometries with moderate interface resistance (a) and zero interface resistance (b), both reproduced from [134]. Finite element simulations of the current density distribution for a notch within an otherwise uniform wire (c) and two rectangular contacts separated by a nanopillar (d), both reproduced from [133]. The height within the main figure, together with the dot density within the inset indicate the magnitude of current density within (c).

point. Inspection of the sample presented previously, which was destroyed during initial parameter testing (inset of figure 5.4), reveals that the sample broke along the junction between Hall bar and electrical contact. This area is precisely where current crowding predicts increased Joule heating.

So far, the current crowding has only considered the vertical slice through the Hall bar/contact assembly and has not considered the lateral dimensions. Hertel has shown that the current density is not uniform under lateral dimension changes, namely a notch within an otherwise uniform wire (figure 5.13(c)) and a nanopillar separating two, larger contacts (figure 5.13(d)) [133]. For a notch within a wire, the current density at the apex of the notch is a factor of 3 greater than the point equidistant along the wire to the notch, yet on the notch free side. For a nanopillar, current enters the pillar radially through the adjacent rectangular contact with a preference for greater current from the bulk contact direction.

Detailed simulations such as those reported by Zhang *et al.*, and Hertel, require complex modelling approaches which are beyond the scope of this thesis. Nevertheless, the general form of the simulated results can be applied to the samples presented here. The postulated top down view of current flow is shown in figure 5.14 for the centre and edge Hall bars. In both the bulk contact and bulk Hall bar, the current density is uniform across the full thin film width with its direction ori-

entated parallel to the electrical contact/Hall bar edge. In the intermediate region, there exists a current funnel. Here, the local current density is chosen such that the total current in any vertical slice of figure 5.14 is constant to ensure continuity. The direction of the current density within the funnel region is determined by straight lines connecting two points of equal ratio along the opposing funnel edges. Using figure 5.14(b) as an example, the current at the top edge of the electrical contact ($[x, y] = [20\ \mu\text{m}, 60\ \mu\text{m}]$) flows along a straight line to the top edge of the Hall bar ($[x, y] = [40\ \mu\text{m}, 20\ \mu\text{m}]$). At any point within the funnel, an equivalent argument is made. For current that originates from the point $[x, y] = [20\ \mu\text{m}, 48\ \mu\text{m}]$ (80 % of the local width), the current within the funnel travels along a straight line to the point $[x, y] = [40\ \mu\text{m}, 16\ \mu\text{m}]$ (80 % of the local width). During the current funnel region, the local current density is, therefore, inversely proportional to the funnel width. This funnel does not fully encompass the electrical contact corners, owing to the preference of higher current densities from the bulk contact direction in figures 5.13(c) and (d). Not shown is any increased local current densities due to the notch-like structure of the sample at positions [35 μm, 20 μm] and [35 μm, 40 μm] in figure 5.14a. As this is not strictly a notch within an otherwise uniform wire, it is unclear as to if there will be an increase, similar to figure 5.13(c), and if so to what extent. As this is a top down view, the vertical component of the current flow due to current crowding at the contact/Hall bar interface is also not shown.

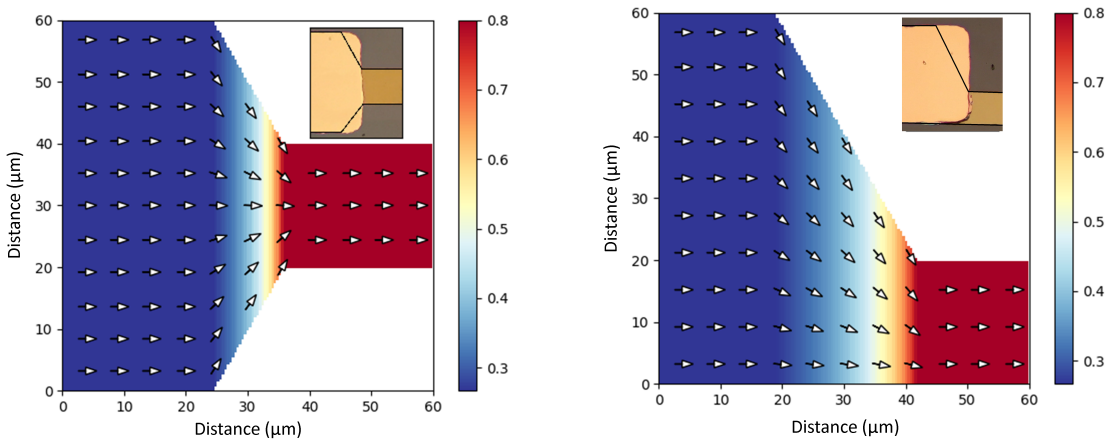

(a) Centred Hall Bar (b) Edge Hall Bar

Figure 5.14: The proposed top down current densities for a 20 μm wide Hall bar at the centre (a) and edge (b) of a 60 μm electrical contact. Any current crowding effects that produce a vertical component to the current density, together with any enhancements due to the notch-like corners are not shown within this simplified view. As the vertical component is neglected, no contact/Hall bar overlap has been included.

Approximate calculations can be made for the Oersted field using the current distributions outlined in figure 5.14. The sample can be discretised into elements of 200 nm by 200 nm and the Oersted field from each element can be summed resulting in the magnetic field distribution across the sample. Figure 5.15 shows the Oersted field for each cartesian direction. It is presented without numerical scales due to the values having a strong dependence on the local current density value which can only be stated with confidence after complex finite element calculations. This value is not expected to change the general form of the magnetic field.

While numerical values cannot be reliably presented in figure 5.15, the Oersted field within the bulk Hall bar and electrical contact can be compared to estimate the magnitude of fields involved. The transverse magnetic field within a uniform current carrying thin film of infinite length and width can be approximated by [140],

$$H_{\mathrm{Oe}} = \frac{2\pi J_{\mathrm{c}}}{10^3}\left(\left|z - \frac{l_z}{2}\right| - \left|z + \frac{l_z}{2}\right|\right) \tag{5.4}$$

where H_{Oe} is in Oersteds, z is the distance from the centre of the wire and l_z is the thickness of the wire. For the Hall bar of Pt(0.9 nm)/Co(0.5 nm)/Pt(3.6 nm), $|H_{\mathrm{Oe}}| = 5.5$ Oe at the location of the Co layer. Under the electrical contact pad, $|H_{\mathrm{Oe}}| = 10.6$ Oe for the structure Pt(0.9 nm)/Co(0.5 nm)/Pt(3.6 nm)/Cu(60 nm). This calculation is based upon a uniform current distribution within the wire. However, this is likely to only be a simplified case due to the aforementioned current crowding. It is, therefore, likely that local Oersted fields exceed the calculations of between 5 Oe and 10 Oe. Inspection of figure 5.5 reveals that current-induced magnetic reversal can occur at fields as low as 5 - 10 Oe within this sample, indicating that, if the direction of symmetry breaking is correct, Oersted fields are of the correct order of magnitude to allow for current-induced magnetic reversal.

There are two main conclusions to draw from the simulations presented in figure 5.15; (a) there exists a non-zero x- and z-component of the magnetic field and (b) the magnetic fields are in opposite directions for the upper and lower portions of the Hall bar. The Oersted field profiles show a non-zero field along both the x- and z- axes along the junction between contact and Hall bar. This magnetic field is expected to increase if current crowding is included. The simulations also show a spatial dependence of the polarity in both fields aligned along the x- and z-axes. As the magnetic reversal depends upon the polarity of both the charge current and symmetry breaking field, the opposing field polarities produced by a charge current of singular polarity will allow for simultaneous magnetic reversal in opposite directions. This is consistent with the bidirectional switching observed in all Hall

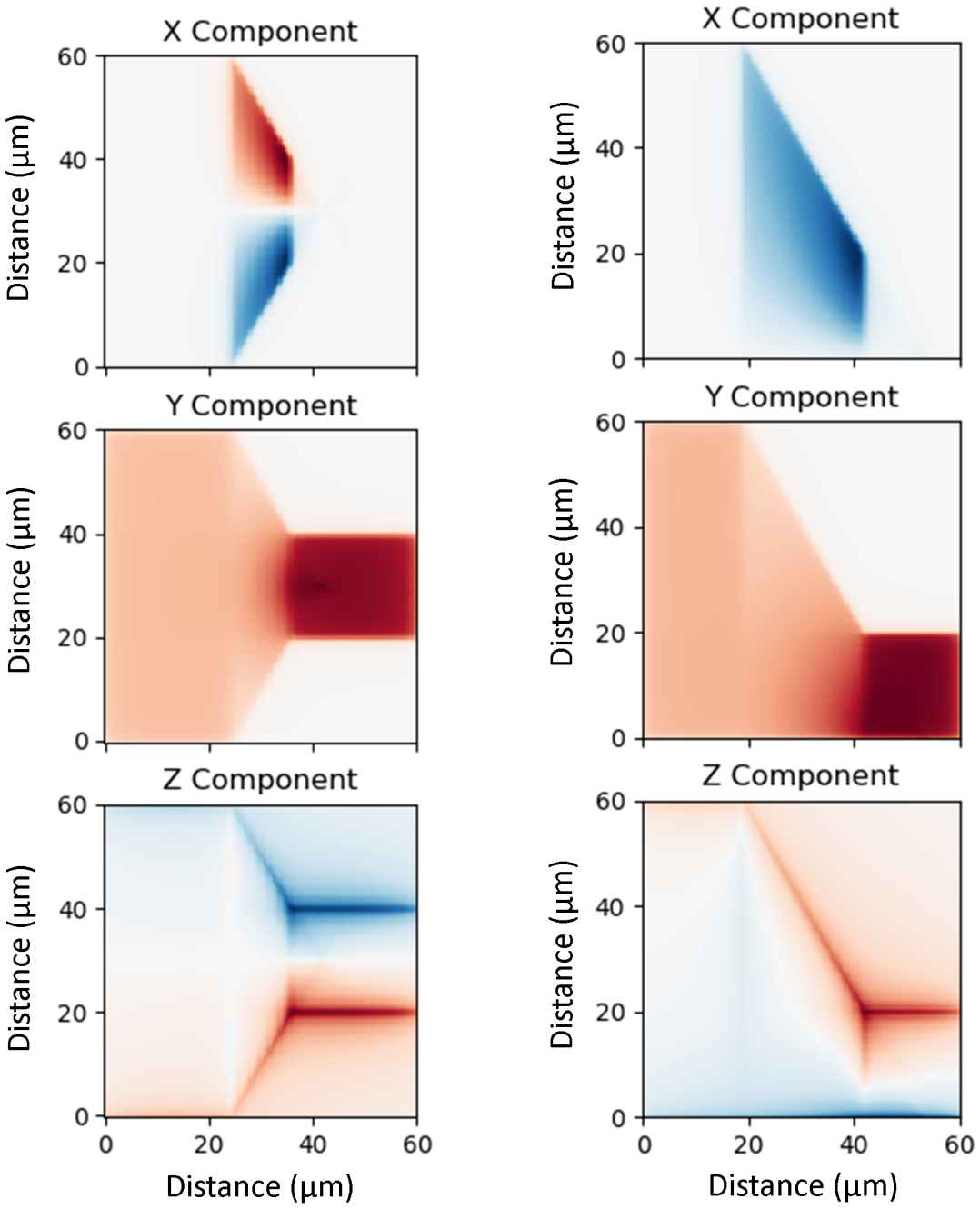

(a) Centred Hall Bar

(b) Edge Hall Bar

Figure 5.15: Calculated Oersted field distributions for the current density configurations presented in figure 5.14. Red and blue indicate Oersted fields of positive and negative polarity respectively, with directions indicated by the coloured arrows. As current crowding effects have been omitted, together with the fact that the numerical field values are sensitive to factors such as the height within the structure to which they are evaluated at, all numerical values have been omitted from the figure. An estimate of the Oersted field magnitude within the uniform Hall bar is presented earlier in this chapter using equation 5.4. The key result of these simulations is the spatial dependence of the direction of the Oersted field, rather than its magnitude.

bar samples. As well as the opposite polarity, the magnetic fields for the Hall bar aligned to the centre of the electrical contacts show that the x- and z-components extend half way into the Hall bar. Again, this is consistent with the experimental observations presented in figures 5.7 and 5.8.

As the Hall bar is offset towards the edge of the electrical contact, the magnetic fields show a different picture. There now exists a significant x- and z-magnetic field only on the side away from the edge of the electrical contact, with the side at the electrical contact edge showing only a y-magnetic field. The x- and z-magnetic fields shown also extend beyond the midpoint of the Hall bar, encompassing approximately 75 % of the width of the Hall bar. Comparing this to figures 5.9 and 5.10, the experimental data show an increased switching region size as the Hall bar is placed towards the edge of the electrical contact, consistent with the calculated Oersted field profiles.

To complete this explanation, a process of current-induced domain expansion is required, akin to that presented within the previous section regarding geometrical domain wall motion. Instead of domain pinning sites being present at each side of the sample, the symmetry breaking field due to current crowding allows for magnetic reversal at the boundary of electrical contact and Hall bar. This newly formed domain expands along the length of the Hall bar under current-induced domain wall motion as presented in [111]

Overall, the theory can be checked against the experimentally determined criteria which were determined earlier in this chapter:

1. The structure can be reasonably modelled by two regions which exhibit deterministic switching in opposite directions.
    - This is achieved through the spatial dependence of the magnetic field polarity within the Oersted field calculations.
2. These regions may differ in magnitude and size, with the region closest to the electrical contact midpoint favouring larger magnitudes/greater size.
    - As the Hall bar position is changed with respect to the electrical contact, the differing current distribution at the end of the electrical contact produces spatial changes to the Oersted field which are consistent with observed switching regions.
3. There exists a dominant domain boundary, possibly parallel or diagonal, along the length of the Hall bar.

- Although the cause of the parallel or diagonal boundary shape is inconclusive, the initial boundary is formed at the zero point of the Oersted field at the Hall bar boundary and propagates along the Hall bar due to current-induced domain wall motion.

4. There may be a portion of the Hall bar, situated between positive and negative remanence regions, that does not undergo magnetic reversal.

    - As the Oersted field is relatively weak, and the exact value of the fields presented in figure 5.15 require detailed parameter measurements, there may exist a region to which the Oersted field is not strong enough to induce reversal, hence creating a region that does not undergo magnetic reversal.

5.6 Conclusions

This investigation studied the field-free magnetic reversal of three Pt/Co/Pt Hall bars with differing electrical contact configurations. The 20 μm wide Hall bar positions were varied between the centre and edge of a 60 μm wide Cu electrical contact. Raster scanned MOKE and Kerr effect microscopy were used to study the spatial distribution of the hysteresis loop remanence.

The Hall bar situated within the centre of the electrical contacts exhibited bidirectional switching under the application of a charge current and in the absence of an applied magnetic field. These regions of positive and negative remanence were approximately equal in size and magnitude, with the Kerr voltage signal slightly less than that of the polar field hysteresis loops. Modelling the current-induced remanence data showed the presence of two regions of opposite polarity, with the possibility of a neutral region in-between. These results, including the central neutral remanence region, were confirmed by Kerr effect microscopy.

Two more Hall bars were investigated, where their position was varied laterally with respect to the electrical contacts. Again, these Hall bars displayed bidirectional field-free magnetic reversal, yet of differing characteristics to the centred Hall bar. The spatial dependence of the hysteresis remanence for both small and large lateral Hall bar displacements consisted of a larger, higher magnitude region upon the side closer to the electric contact centre. On the opposite side, there exists weak or no magnetic reversal.

It has been shown that the presented data does not match any reported mechanism for field-free magnetic reversal. Structural gradients were ruled out after XRR

and coercivity investigations lacked any of the expected signatures of structural variations. The final method of domain wall motion was excluded due to both the lack of typical domain wall pinning sites, together with the adopted experimental method which promoted an initial saturation state, compared to the required multidomain state.

Finally, the new method of current crowding and Oersted fields was detailed. This method consists of non-uniform local current densities due to factors such as structure sizes, resistivities and interface qualities. It is expected that the current propagates using the full 60 μm width of the electrical contact until very near to the end, for which the current funnels towards the 20 μm wide Hall bar. As the resistance of the Cu contact is an order of magnitude lower than that of the Pt Hall bar, the charge current largely travels through the Cu within the overlap region. The current crowding effect causes the current to predominantly enter the Hall bar at the very end of the overlapping region, rather than uniformly over such region. Oersted field calculations which use a basic model of such current crowding have shown a magnetic field along both the x- and z-axes. These magnetic fields match the spatial signatures observed within the Kerr remanence data. Therefore, it is thought that a new method of field-free magnetic reversal has been presented. This method involves the nucleation of a domain where the symmetry breaking occurs due to Oersted fields and current crowding effects, before propagating along the length of the Hall bar through spin torque-induced domain wall motion. This work can be expanded with the addition of time-resolved Kerr microscopy data to verify the magnetic reversal nucleation point. In addition, electrical contact structures specifically designed to induce various levels of funneling would be of great interest.

Chapter 6

Spin-orbit torques - Influence of Current-Induced magnetic reversal on effective field measurements

6.1 Introduction

Much like all areas of physics, there is a desire to simplify any observed phenomena into the smallest set of parameters for easier quantitative comparisons between studies. In terms of SOTs, the most widely used parameters are the spin Hall angle and the spin diffusion length [34, 141–143]. The spin Hall angle represents the efficiency of conversion between charge currents and transverse spin currents [33] and the spin diffusion length describes the decay of pure spin currents during propagation [144].

There are several techniques available to determine these parameters, each with their own advantages and disadvantages. A common theme between some of these techniques is the requirement for the magnetic moments to tilt uniformly across the sample and for there to be no current-induced magnetic reversal [30, 32, 145, 146]. While many publications state that this is true for the particular setup in use, evidence of this statement is often missing. Meanwhile, there has been a discrepancy of measured spin Hall angles and spin diffusion lengths of over an order of magnitude with many plausible explanations for this variation [57, 59, 147]. Over time, the community now generally agrees on the typical values of these parameters, however, while some work has been done to understand the variance of these values, some doubt still remains.

This chapter serves to investigate the approximation that is fundamental to many of the spin Hall angle measurement techniques, that the moments within the sample tilt uniformly and no magnetic reversal is present. In particular, this chapter

aims to quantify the unwanted contribution to effective field measurements from current-induced magnetic reversal. The chapter begins by describing a selection of the various techniques available while highlighting why this approximation is important. The modified technique of MOKE determination is then used throughout this chapter to quantify the maximum contribution of current-induced magnetic reversal to the effective field measurements.

6.1.1 Measurement configuration

The methodology employed within this chapter involves several symmetry arguments and specific experimental configurations to orientate the magnetisation in the desired direction. To facilitate this, the nomenclature needs to be clearly defined. Figure 6.1 shows the cartesian axes with respect to the sample. The x axis is parallel to the long axis of the Hall bar and the applied current is always parallel to this axis. The azimuthal angle is defined as the angle subtended by a vector and the x axis while remaining in the xy plane, with the polar angle defined as the angle between the vector and the film normal. $\theta = \phi = 0$ are defined along the x axis.

Throughout this chapter, there are many experimental configurations which vary the azimuthal angle of the applied magnetic field. For measurements involving charge currents, the applied magnetic field will always be within the sample plane ($\phi = 0$).

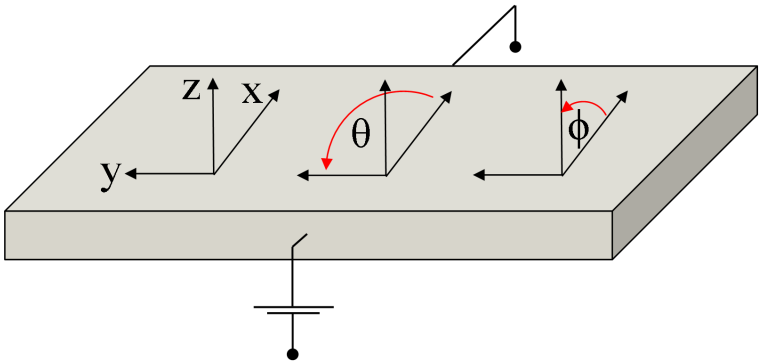

Figure 6.1: Definition of the Cartesian axes, azimuthal (θ) and polar angles (ϕ). The Hall bar has its long axis directed along the x axis and its short axis directed along the y axis. In the following section, the charge current is applied along the x direction.

6.2 Spin-orbit torque effective field measurement techniques

The effective fields due to SOTs can be measured using an electrical [29–31, 148] or optical approach [32, 149]. The electrical option utilises the Hall effect and the optical approach is based upon the Kerr effect. Both techniques have been documented in the literature and come with their own advantages and disadvantages.

The electrical approach to measuring the SOT effective field strength involves measuring the second harmonic Hall effect signal [29, 30, 150, 151]. This measurement includes several unwanted contributions. First, sample fabrication errors such as misaligned voltage probes can cause a fraction of the longitudinal voltage to be present within the transverse Hall voltage measurements. Secondly, other contributions need to be isolated, such as the anomalous Nernst-Ettinghausen effect (ANE) [30, 152]. The ANE produces non-zero voltage contributions if there exists temperature gradients within the sample due to sources such as Joule heating [153, 154]. Once these artefacts have been removed from the measured signal, the resulting signal is a summation of contributions from the planar Hall effect and the anomalous Hall effect. These contributions can be separated by simultaneously modelling data taken with applied magnetic fields at various angles with respect to the applied charge current [30].

The method of electrical determination requires sensitive instruments and detailed signal analysis. As an alternative to this, an optical approach can be used by which the SOT information is present within the first harmonic Kerr signal and is, therefore, a stronger signal [32, 149]. The optical approach has the secondary benefit of not containing voltage signal artefacts such as those from the ANE or longitudinal resistance. The following section details the optical method utilised within this chapter.

6.2.1 The AC effective field method

The technique used within this chapter aims to measure the alternating effective fields produced by AC charge currents with the use of a polar MOKE instrument. This instrumental setup has been described previously in chapter 4, in particular figure 4.3. The only addition to the displayed setup is the inclusion of a current source connected directly to the sample through the use of a sample holder with low profile pogo pins, as detailed in the sample environment section 4.3.2.

When the measurement frequency is much lower than the precessional frequency of the magnetisation, the effects of SOTs can be considered in terms of effective

fields. There exists two effective fields, a field-like effective field (H_{FL}) proportional to $\vec{z}\times\vec{j_c}$ and a damping-like effective field (H_{DL}) proportional to $\vec{m}\times(\vec{z}\times\vec{j_c})$, where $\vec{m}$ represents the magnetic moment. For structures which display perpendicular magnetic anisotropy, the direction of the effective fields are shown in figure 6.2. The polarity of the effective field depends upon the order of the sample layers and the materials used. In the absence of external magnetic fields, an AC charge current of frequency f causes the magnetisation to oscillate about its equilibrium axis ($\phi = 90°$). When measured with a polar MOKE instrument, the Kerr signal oscillates at frequency $2f$ due to the fact that the polar MOKE is only sensitive to moments along the z axis.

Applying an external magnetic field parallel to the applied charge current causes the magnetisation to tilt in the same direction as the damping-like effective field. This breaks the yz symmetry of any damping-like oscillations as a negative damping-like effective field will drive the magnetisation back to the polar axis and a positive effective field will drive the magnetisation further away from the polar axis. This produces a polar Kerr signal oscillation at a frequency f with an amplitude that is proportional to the effective field strength. In this tilted configuration, the field-like effective field produces negligible changes in the magnetisation resolved along the z axis. This is shown graphically in figure 6.2(b). An identical argument can be made for when the applied field is perpendicular to the charge current. Here, the sensitivity has been reversed such that Kerr signal is sensitive to the field-like effective field only, as shown in figure 6.2(c).

Details of the expected Kerr signals are shown in figure 6.3. Figure 6.3(a) shows the Kerr signal measured under the application of an AC charge current and in the absence of an externally applied magnetic field. The charge current has a sinusoidal waveform of frequency f, as shown in figure 6.3(c). The magnetisation returns to the polar axis in the absence of a charge current regardless of the charge current phase (0 or π), hence, the observed Kerr signal in figure 6.3(a) is at a frequency of $2f$. Figure 6.3(b) shows the same measurement but now with an externally applied magnetic field. The alternating effective field which is parallel to the applied field creates oscillations in the Kerr signal which are at the same frequency as the charge current. The sign of the spin Hall angle is encoded into the phase of the oscillations, with an opposite spin Hall angle producing a phase shift of 180°. The amplitude of the oscillations is proportional to the effective field strength.

The relationship between the measured Kerr signal and the effective field strength is given by [32],

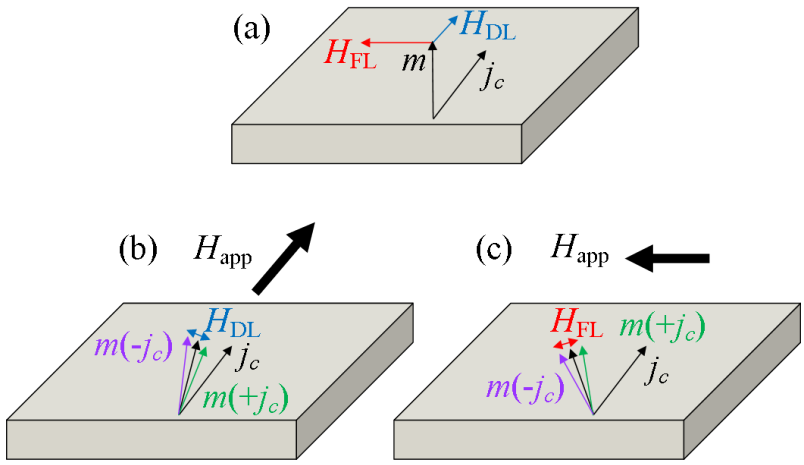

Figure 6.2: (a) Schematic showing the direction of the charge current density j_c, magnetisation m, damping-like effective field H_{DL} and field-like effective field H_{FL} in the absence of an external magnetic field H_{app}. (b) When an external field is applied parallel to the AC charge current, the magnetisation is tilted (black vector) in the direction of the applied field with positive and negative modulations (green and purple vectors) occurring due to the positive and negative damping-like effective fields. (c) When the applied field is perpendicular to the charge current, the resulting oscillations are caused by the field-like effective field.

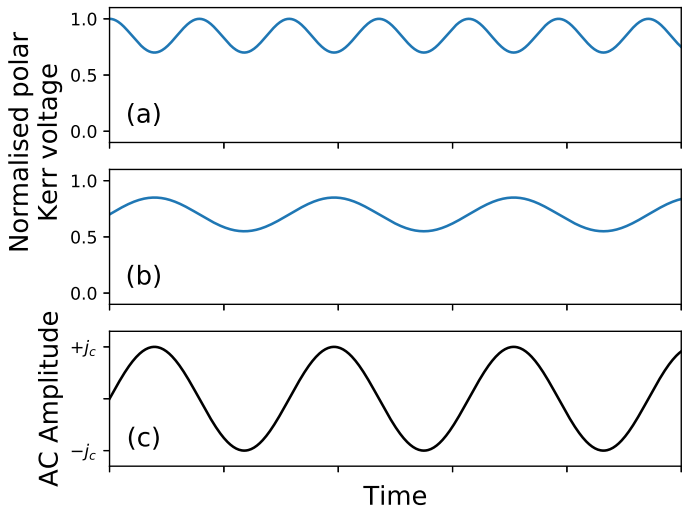

Figure 6.3: The expected Kerr signal oscillations due to the effective field modulations presented in figure 6.2. (a) Kerr signal oscillations in the absence of an external applied magnetic field create a signal at twice the frequency of the charge current modulation. (b) When an external field is applied, the Kerr signal oscillates at the same frequency as the charge current modulation, as shown in (c).

$$\frac{C_\omega}{C_0} = \frac{H_{\mathrm{DL(FL)}}}{H_k^2} H_{\parallel(\perp)}, \tag{6.1}$$

where C_ω is the first harmonic Kerr voltage, C_0 is the Kerr voltage at magnetic saturation, H_k is the effective anisotropy field and $H_{\parallel(\perp)}$ is the applied field parallel (perpendicular) to the charge current. This equation is valid for small applied magnetic fields. C_0 is obtained my measuring a standard polar field MOKE hysteresis loop and calculating half of the difference between positively and negatively saturated Kerr signals. The left hand side of this equation appears in various forms within the literature as it merely represents the fraction of the polar magnetisation change due to the effective field oscillations. Equation 6.1 is only valid for small oscillations.

There are three different ways in which the effective fields can be probed through equation 6.2; one can vary the applied field magnitude, charge current magnitude (which is proportional to $H_{\mathrm{DL(FL)}}$) and varying H_k (for example, through the application of external polar magnetic fields). The results of this chapter are generated through investigations which vary the applied field magnitude and direction along with the charge current magnitude. The applied field is always within the plane of the sample ($\phi = 0°$) as to leave H_k unmodified. The following section probes the effect of current-induced magnetic reversal upon this method of effective field determination and identifies how such a method can be modified to isolate the contributions of current-induced magnetic reversal.

6.2.2 The impact of current-induced magnetic reversal

The method of effective field determination through the modulation of the polar Kerr signal assumes coherent magnetisation rotation and, therefore, current-induced magnetic reversal is undesired. As the following sections will show, current-induced magnetic reversal is possible through the use of an AC charge current and an external magnetic field with a non-zero component parallel to the charge current. Comparing this to the setup described in the previous section for damping-like effective field measurements, the experimental configuration is identical. For field-like effective field measurements the external magnetic field is applied perpendicular to the charge current, hence, there exists no component of the field parallel to the charge current. As the required symmetry breaking for magnetic reversal has not been satisfied in this case, no current-induced magnetic reversal is expected. It is, therefore, expected that current-induced magnetic reversal should only affect damping-like effective field

measurements.

To isolate the contribution of current-induced magnetic reversal to the effective field measurements, a modification of equation 6.1 is required. Rather than measuring C_ω/C_0, this can be replaced by the hysteresis loop remanence fraction,

$$\frac{R_\omega}{R_0} = \frac{H_{\mathrm{DL(FL)}}}{H_k^2} H_{\parallel(\perp)}, \tag{6.2}$$

where R_ω is the remanence of the AC charge current hysteresis loop and R_0 is the remanence of a standard AC field polar MOKE hysteresis loop. Since the remnant Kerr signal represents the amount of polar magnetisation remaining at zero applied AC charge current, the effective fields at this point are zero. The remanence also provides a measure for the net amount of magnetic reversal which has occurred within the previous half period of the applied charge current. If no current-induced magnetic reversal has occurred then $R_\omega = 0$ and $H_{\mathrm{DL(FL)}} = 0$. Contrary, if magnetic reversal is present, $R_\omega \neq 0$ and a non-zero value for the measured effective field is observed.

While this methodology shows that it is possible for current-induced magnetic reversal to occur within the same experimental configuration as that of damping-like effective field measurements, the symmetry of both systems should be compared. As the effective field is proportional to the applied charge current, retaining a fixed charge current magnitude while sweeping the applied field should result in a linear relationship which passes through the origin. The following section details the sample investigated.

6.3 Description of the samples investigated

The sample used within this chapter consists of a Hall bar which has a nominal structure of Pt(1 nm)/Co(0.6 nm)/Pt(4.4 nm) with Cu(50 nm) electrical contacts. The first stage of sample fabrication involved the creation of a 20 μm by 100 μm Hall bar by method of photolithography. The Hall bar structure was sputter deposited onto a Si/SiO_2 substrate with a base pressure better than 6×10^{-8} Torr. A second photolithography and sputter deposition stage was performed to fabricate the electrical contact pads. The combined resistance of the Hall bar and electrical contacts was $340 \pm 10\ \Omega$.

Figure 6.4 shows a polar MOKE measurement of the sample along with the the Kerr signal obtained during a longitudinal field sweep. The polar MOKE measurement shows a clear perpendicular magnetic anisotropy with a coercive field of

19.6 ± 0.3 Oe. The anisotropy field, H_k, can be estimated by fitting the Stoner-Wohlfarth model to the longitudinal field Kerr signal [149],

$$\frac{M_z}{M_s} = \cos\left(\arcsin\left(\frac{H_{\text{app}}}{H_k}\right)\right), \tag{6.3}$$

where M_z is the component of the magnetisation along the z axis, M_s is the saturation magnetisation, H_{app} is the applied longitudinal magnetic field and H_k is the anisotropy field. The value obtained by fitting equation 6.3 to the data in figure 6.4 is 1490 ± 40 Oe, which is similar to comparable structures in the literature [149, 155]. This value indicates that the perpendicular magnetic anisotropy is weak, allowing for easier determination of the effective fields from equation 6.2.

The sample structure was chosen as to minimise the field-like effective field while giving a sizeable damping-like effective field. The presence of Pt at both the top and bottom interface of the Co layer minimises the Rashba effect (and hence the field-like component) by way of inducing structural inversion symmetry at the interfaces. The Pt layer thicknesses were chosen such that the seed layer is below the spin diffusion length of Pt (1-2 nm) and would, therefore, have only a minor contribution to the total spin current entering the Co layer. The majority of the spin current will originate from the top Pt layer as the thickness is much greater than the spin diffusion length. The following section presents the first current-induced magnetic reversal results whereby the external field is applied parallel to the charge current.

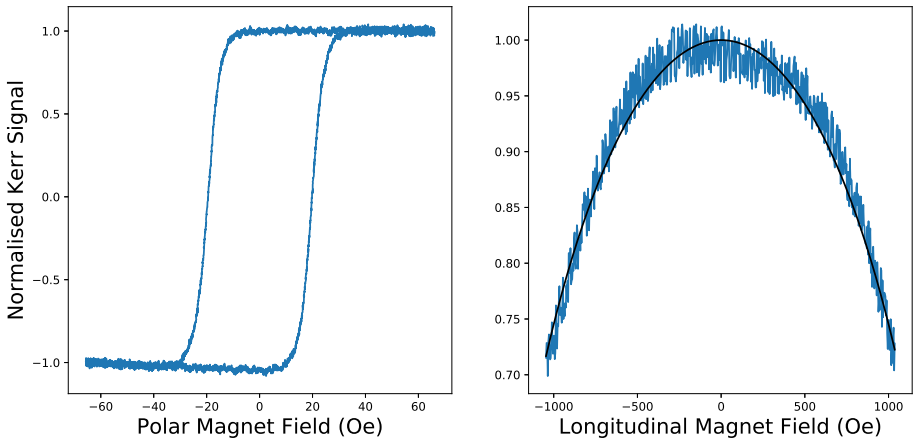

Figure 6.4: The MOKE response of the sample under the application of an AC polar magnetic field and an AC longitudinal magnetic field (left). The sample displays a clear perpendicular magnetic anisotropy within the polar hysteresis loop, whereby the anisotropy strength can be quantified by fitting equation 6.3 to the longitudinal field sweep data (right).

6.4 Investigating the effect of magnetic reversal upon effective field measurements

6.4.1 Magnetic fields parallel to the charge current

An investigation into the magnetic reversal of the Pt/Co/Pt structure under the application of a DC magnetic field and AC charge current was performed. Here, the applied magnetic fields were in the range of -240 Oe to 240 Oe and were applied (anti)parallel to the charge current. The charge current was in the form of a three second pulse and its amplitude ranged from -45 mA to 45 mA ($\pm 3.75 \times 10^{11}$ A/mm^2). The magnetic state was measured by the polar Kerr effect before and after the pulse with figure 6.5 showing the change in Kerr signal within the 2D parameter space. A value of 1 within figure 6.5 indicates that the magnetisation has switched completely from a negative to positive saturation state. Similarly, a value of -1 indicates reversal

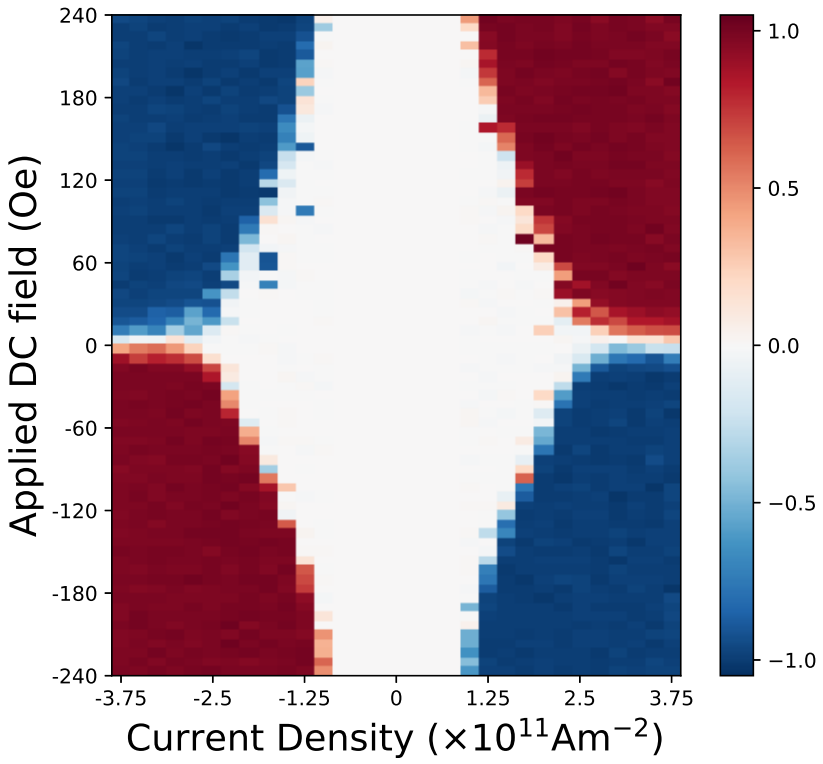

Figure 6.5: Four quadrant magnetic switching map showing the relationship between AC charge current magnitude and magnetic field strength upon the magnetic reversal. A value of 1 (-1) indicates complete reversal from negative to positive (positive to negative) magnetic saturation states. Zero indicates no magnetic reversal.

in the opposite direction and zero indicates no magnetic reversal has occurred.

The switching distribution presented in figure 6.5 is typical of a perpendicularly magnetised sample undergoing current-induced magnetic reversal. No switching is observed in the regions where the magnetic field and/or the charge current are below the threshold required to induce magnetic reversal. Increasing either the magnetic field or charge current will allow for magnetic reversal once the threshold has been passed.

When the polarity of the magnetic field or charge current is changed, the direction in which symmetry breaking occurs is reversed, causing the direction in which magnetic reversal occurs to also reverse. Hence, each quadrant within figure 6.5 has the opposite polarity with respect to its adjacent quadrants. When the polarity of both the magnetic field and charge current is changed simultaneously, the magnetic reversal undergoes two polarity flips resulting in no net change, therefore, opposite quadrants are of the same polarity. The position of the threshold region defining the onset of magnetic reversal is, to a first approximation, equal for all polarity combinations. The possibility of asymmetric threshold positions is discussed later within section 6.4.5. The following section details the calculation of the damping-like effective field from the current-induced magnetic reversal data.

6.4.2 Measurements of the damping-like effective field

Figure 6.6 shows the remanence fraction as a function of applied DC magnetic field for ten different current magnitudes. The data for each current magnitude is equivalent to vertical slices of the lower right quadrant of figure 6.5. The data shows that for increasing current magnitudes, magnetic reversal occurs at a lower applied field value, indicating that the SOT strength is proportional to the charge current magnitude.

Using equation 6.2, it is possible to calculate the maximum damping-like effective field measurement contribution from magnetic reversal. As the data is approximately linear within the switching region (remanence fractions in the range of -0.1 to -0.9) with flat regions at higher and lower applied fields, an error function was chosen to model the data. The method of least squares was used to optimise the models with best fit solid lines added to figure 6.6. From equation 6.2, the gradient of the model is equal to H_{DL}/H_k^2.

Strictly speaking, the gradient must be constant for all applied magnetic field values within this method, however, inspection of figure 6.6 shows that this is only true for high currents within this sample. Inspection of the red, 12.5 mA data set shows a positive, non-zero gradient in the region of -220 Oe to -170 Oe with zero

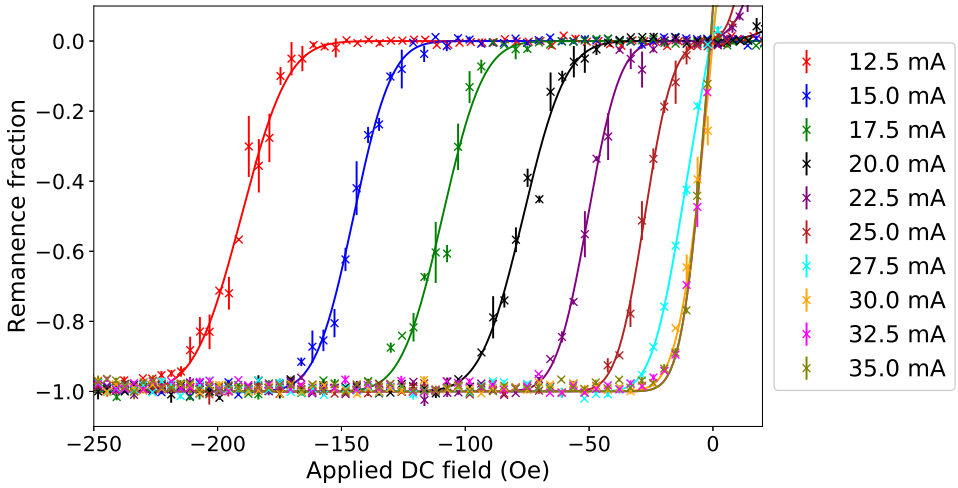

Figure 6.6: Remanence fraction (R_ω/R_0) as a function of the applied magnetic field for ten different AC charge current magnitudes. Best fit error functions (solid lines) have been added for each unique charge current.

gradient otherwise. The consequence of this difference will be discussed later in section 6.4.5 after a complete picture has been presented. As this chapter aims to determine the extent to which current-induced magnetic reversal can affect the effective field measurements, the maximum gradient observed will be used within the following analysis.

Figure 6.7 shows the calculated damping-like effective field as a function of the charge current density. The data appear linear within the charge current range investigated, consistent with other studies. At $J_c = 1 \times 10^{11}\text{Am}^{-2}$, the damping-like effective field is 46 ± 2 kOe which is several orders of magnitude greater than that presented for similar structures in literature [156–158]. As discussed earlier in section 6.2.2, current-induced magnetic reversal and correct damping-like effective field measurements share the same experimental symmetries, therefore, a large contribution to the measured damping-like effective field was expected. What is surprising is the sheer scale of the measured value compared to the expected value of 50-100 Oe for similar studies [156–158].

It is worth reminding the reader that this analysis is based upon the maximum gradient of the remanence fraction data in figure 6.6 and should be thought of as an upper limit of the effective field contribution. It is, however, interesting to put this value into context. To achieve the literature value of $H_{\text{DL}} \approx 50$ Oe, only 0.1 % of the sample area must undergo current-induced magnetic reversal while the remaining 99.9 % remains unchanged. For a MOKE laser spot size of radius 5 μm, this equates to an area of radius 160 nm undergoing magnetic reversal. The following section

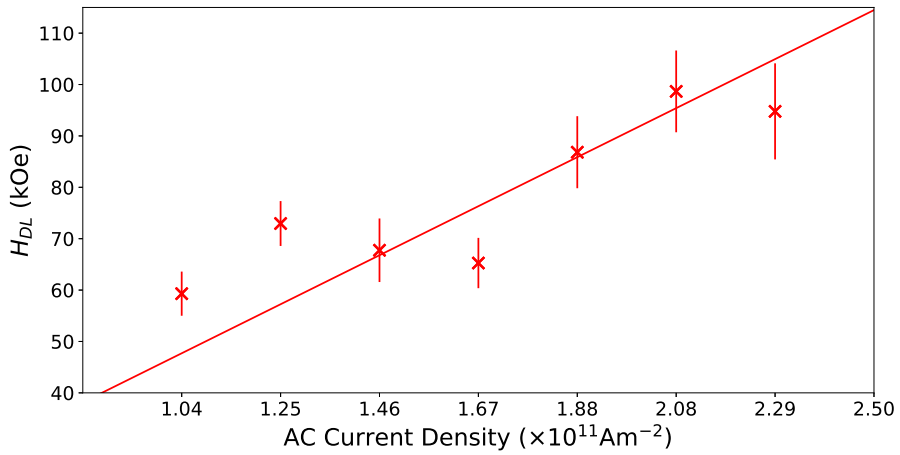

Figure 6.7: The magnitude of H_{DL} as a function of current density extracted from the best fit models to data in figure 6.6. A line of best has been added showing the linear proportionality of the damping-like effective field with charge current magnitude.

discusses the changes to the magnetic reversal process through the introduction of a non-zero angle between the applied magnetic field and the charge current.

6.4.3 Magnetic fields applied at an angle to the charge current

The angular dependence of the applied magnetic field has been varied within the range of $-45^{\circ} < \theta < 135^{\circ}$. Figure 6.8 shows the degree of magnetic reversal for eight unique angles within the magnetic field and charge current range of -230 Oe to 20 Oe and $1 \times 10^{11}\mathrm{Am}^{-2}$ to $3 \times 10^{11}\mathrm{Am}^{-2}$. For small applied field angles ($|\theta| \leqslant 30^{\circ}$), the switching maps are visually indistinguishable to the reader. Beyond $|\theta| = 30^{\circ}$, changes begin to appear with the most noticeable change occurring within the low current density data. Figure 6.8(a) ($\theta = -45^{\circ}$) shows that for the lowest current density probed ($1 \times 10^{11}\mathrm{Am}^{-2}$), the threshold for magnetic reversal to begin occurs at approximately 200 Oe. Comparing the equivalent current density in figure 6.8(b) ($\theta = 0$), the onset of magnetic reversal is reduced to approximately 175 Oe. This is further exemplified for $\theta = 60^{\circ}, 70^{\circ}$ within figures 6.8(d,e) respectively, whereby the required field magnitude for magnetic reversal is beyond the range studied.

When the external magnetic field is applied at an angle of $\theta = 90^{\circ}$, no magnetic reversal is observed. Figure 6.8(f) shows only minor changes in the Kerr signal remanence, particularly for current densities above $2.3 \times 10^{11}\mathrm{Am}^{-2}$. The small amount of observed magnetic reversal does not follow the expected symmetry reversal for

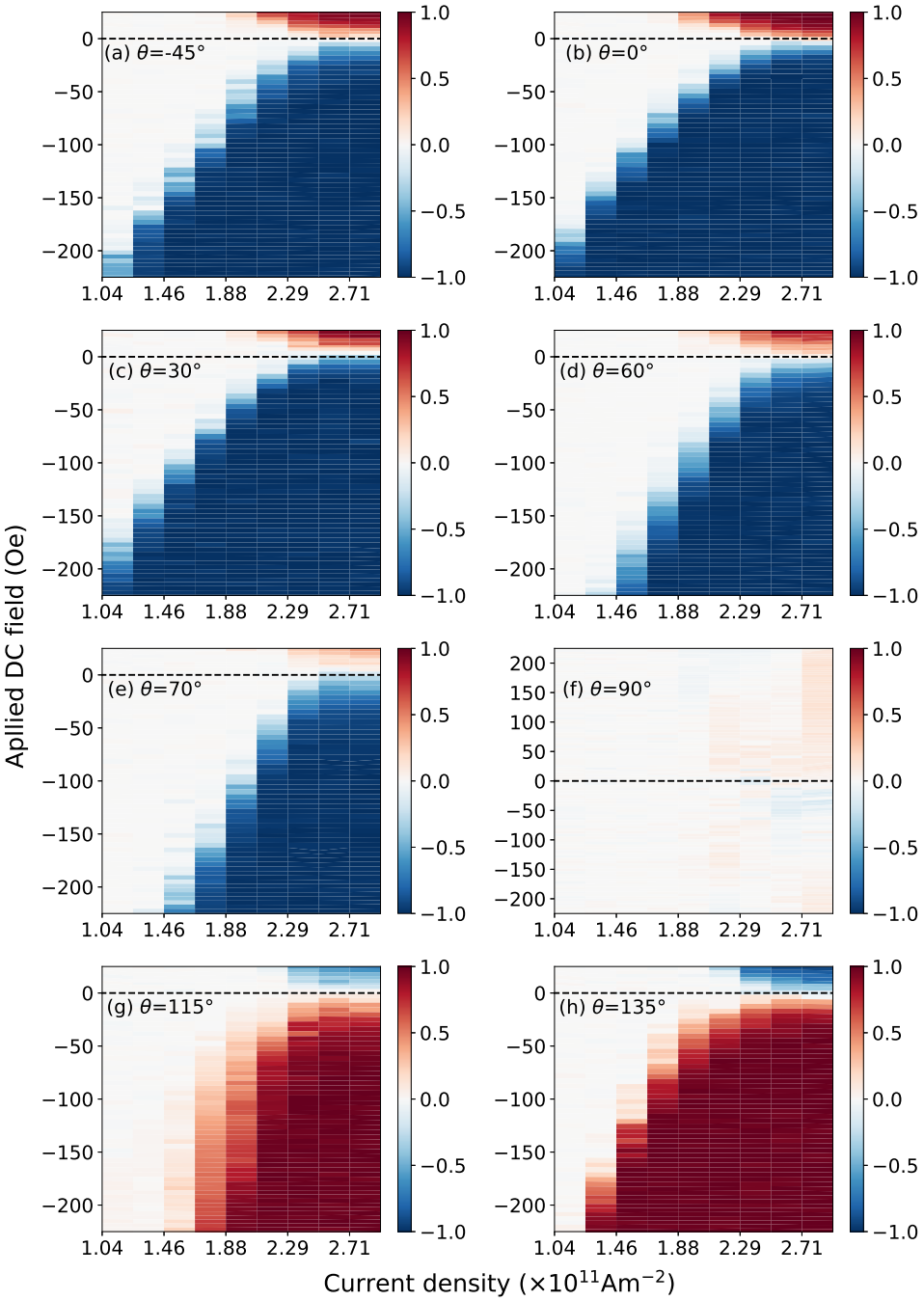

Figure 6.8: Single quadrant magnetic switching maps showing the change in magnetic reversal profile as the angle (θ) between the applied field and charge current is varied from $\theta = -45°$ (a) to $\theta = 135°$ (h). A value of 1 (-1) indicates complete reversal from negative to positive (positive to negative) magnetic saturation states. Zero indicates no magnetic reversal.

positive and negative applied field magnitudes. Hence, the cause of the non-zero measurement is attributed to small applied field misalignments or field-free magnetic reversal. Inspection of the switching maps for all angles other than $\theta = 90^\circ$ indicate that for current densities above $2.3 \times 10^{11} \mathrm{Am}^{-2}$, magnetic reversal can occur for applied field magnitudes less than 5 Oe. The magnet used for this investigation has a pole tip size of 3 mm and a pole to sample distance of approximately 20 mm. This configuration severely limits the maximum possible field quality and requires small alignment tolerances to ensure that the area of the sample being measured exists within the good field region of the magnet. The good field region of the magnet is defined as the region by which there exists a pure dipole field component. As the good field region of the magnet is expected to be approximately 1 mm^3 or less, the limited accuracy of the magnet alignment results in the plausible existence of a small field component transverse to the main dipole field direction. If this field component is near the threshold value to induce magnetic reversal of approximately 5 Oe, inconsistent magnetic reversal may occur giving rise to the signals observed for $\theta = 90^\circ$. Secondly, these signals may be attributed to field-free magnetic reversal, as detailed in chapter 5.

In figures 6.8(g,h), the applied magnetic field has a component antiparallel to the charge current resulting in a polarity change with respect to the results presented for $|\theta| < 90^\circ$. Aside from this polarity change, the results are approximately equal to their low angle counterparts, however, there exists some small discrepancies within quantitative features. For example, inspection of the low charge current region in figures 6.8(a,h) show that the magnetic field required for magnetic reversal is slightly higher for $\theta = 135^\circ$ than for $\theta = -45^\circ$. While this difference is noted at this stage, a full discussion of such differences is reserved for section 6.4.5. To briefly summarise the speculated cause, small field misalignments cause magnetic reversal to become favoured in one direction and restricted in the opposite direction producing asymmetric hysteresis loops. As the magnet required a physical realignment between field angle measurements, this imposed a finite limit to the achievable accuracy and/or consistency of such field misalignments between measurements at different angles. The following section builds upon the angular dependence of the magnetic reversal by measuring the effective field at each angle.

6.4.4 The angular dependence of the effective fields

Figure 6.9 shows the remanence fraction as a function of the applied magnetic field for ten different charge current magnitudes at seven different θ angles. As per the previous discussion for $\theta = 0$, there is an inverse relationship between the charge

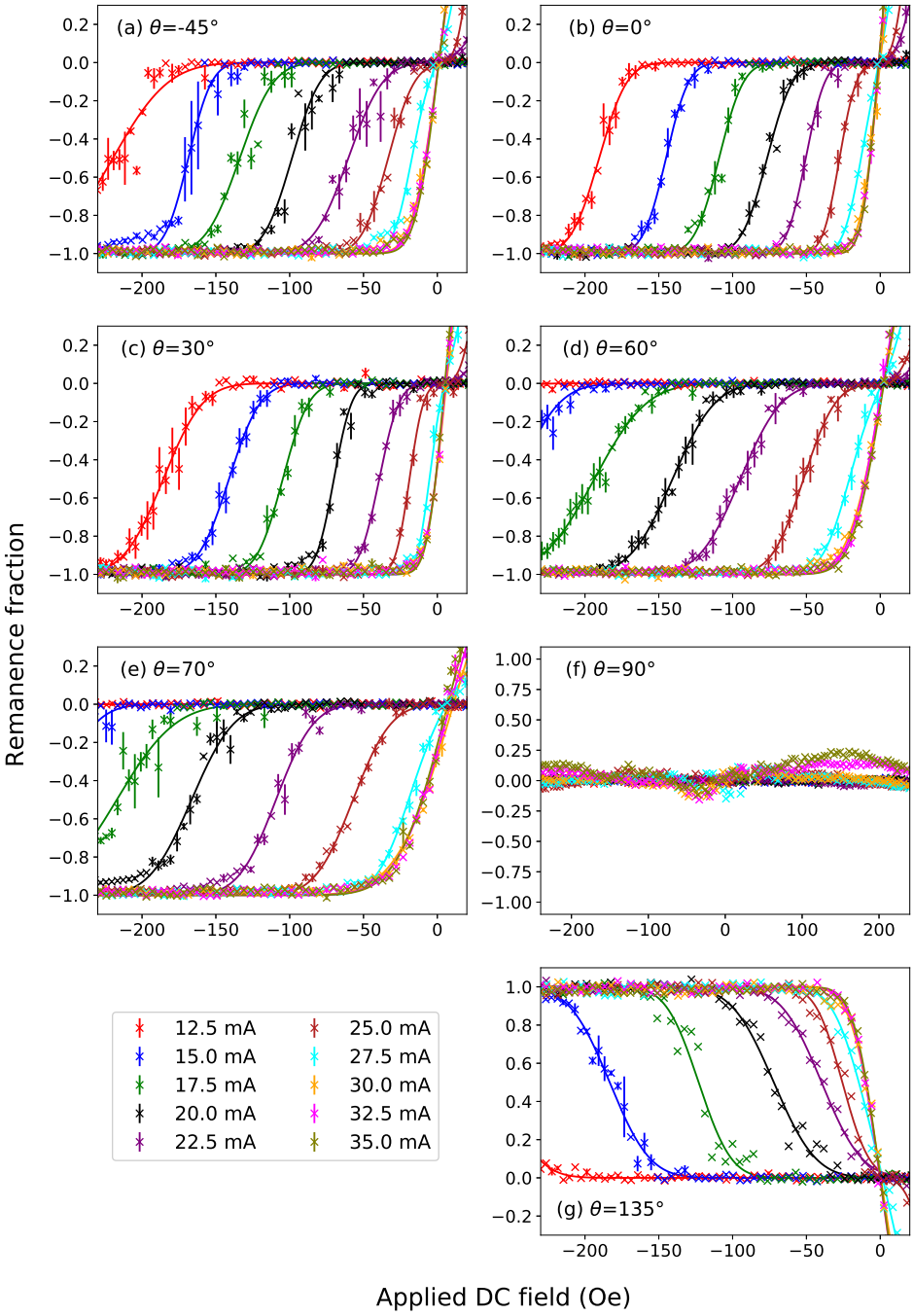

Figure 6.9: Remanence fraction (R_ω/R_0) at seven unique angles between the applied magnetic field the AC charge current.

current magnitude and applied magnetic field at the threshold of magnetic reversal. For $|\theta| > 30°$, current-induced magnetic reversal occurs beyond the magnetic field range studied within the low charge current region.

Comparing data at various angles for a singular charge current magnitude graphically displays the effective field variations. For example, inspection of the mid-range charge current value of 20 mA (black data points) shows a positive high gradient best fit curve within the switching region of figure 6.9(b) for $\theta = 0°$. As the value of θ is increased, the gradient within the magnetic reversal region decreases, indicating a reduction in the effective field strength. At $\theta = 90°$, the gradient is approximately zero before becoming negative for angles above $\theta = 90°$.

Using an identical method to that presented for $\theta = 0°$ in section 6.4.2, it is possible to determine the maximum effective field strength from the gradient of the best fit lines within figure 6.9. Figure 6.10 shows the calculated effective fields at $1 \times 10^{11}\text{Am}^{-2}$ for each θ value except for $\theta = 90°$. Due to the lack of current-induced magnetic reversal at this angle, the data were unsuitable for model fitting and parameter extraction.

The data presented within figure 6.10 represent the damping-like effective field at $\theta = 0°$ and the field-like effective field at $\theta = 90°$. The effective field measured at

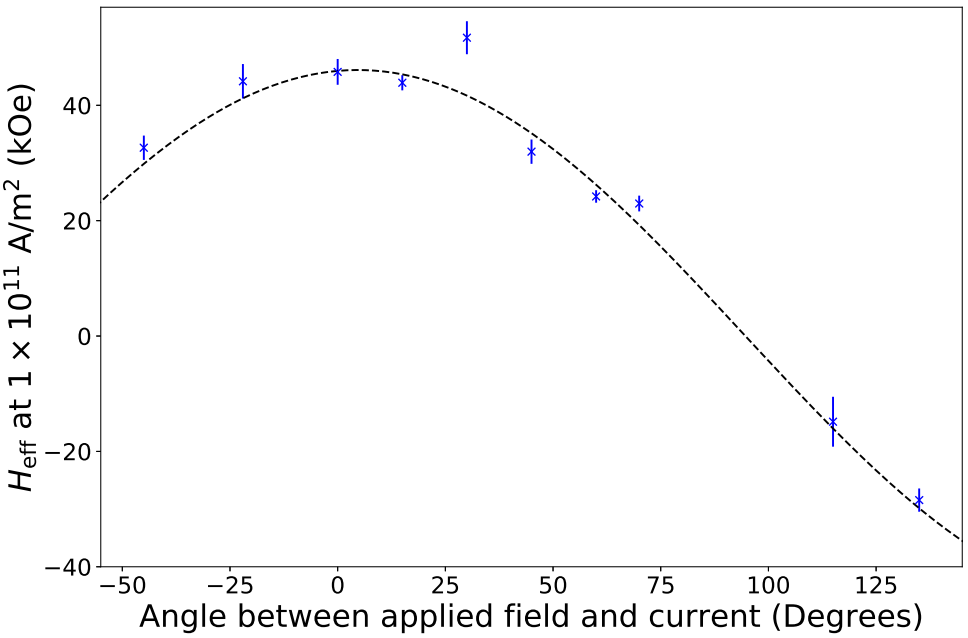

Figure 6.10: The measured effective field strength as a function of the angle between the applied magnetic field and the charge current. A trend line of the form $|H_{\text{DL}}| \cos\theta + |H_{\text{FL}}| \sin\theta$ has been added.

intermediate angles takes the form of,

$$H_{\text{eff}} = |H_{\text{DL}}| \cos\theta + |H_{\text{FL}}| \sin\theta. \tag{6.4}$$

Using this equation, the calculated effective fields are $H_{\text{DL}} = 46 \pm 2$ kOe and $H_{\text{FL}} = 4 \pm 2$ kOe at $1 \times 10^{11}\text{Am}^{-2}$. The damping-like effective field value is consistent with the previous calculation using the singular data set for $\theta = 0°$. For all θ values presented, the data fits the model well. Unfortunately, due to experimental limitations in the maximum applied magnetic field strength and the lack of current-induced magnetic reversal at $\theta \approx 90°$, it was not possible to obtain data points within this region. As the field-like effective field is multiplied by $\sin\theta$, it is desirable to have a high data point density in the region of $\theta = 90°$ for accurate amplitude evaluation. As the data presented does not satisfy this, the value obtained for the field-like effective field is highly unreliable. The following section discusses the presence of any additional field components which may impact on the measured effective field results.

6.4.5 Additional field contributions

Throughout this study, care was taken to achieve the best possible field alignment with respect to the charge current direction. However, due to the limited accuracy of the magnet used, there exists a finite yet non-zero error regarding the direction of the applied magnetic field. Other additional field components are unavoidable, such as the Oersted field, whereby chapter 5 describes the process in which current-induced magnetic reversal can occur via the Oersted field in the absence of an external field. These additional field components may give rise to asymmetric magnetic reversal maps, as discussed previously in sections 6.4.1 and 6.4.3.

Figure 6.11 shows the critical current density (or equivalently, the coercive current density) for current-induced hysteresis loops at four different field angles. At all angles, there is a clear reduction in the half loop width with increasing applied field magnitude. This reduction is, however, asymmetric with respect to the positive and negative critical current densities. Across all angles, a difference of up to 15 % is observed between the gradient of the positive and negative critical current densities as a function of the external field strength. This difference changes for different values of θ and does not form any observable pattern.

As the gradient asymmetry appears to preserve the linearity of the data, the cause of such asymmetry is also expected to be linear with the applied field strength

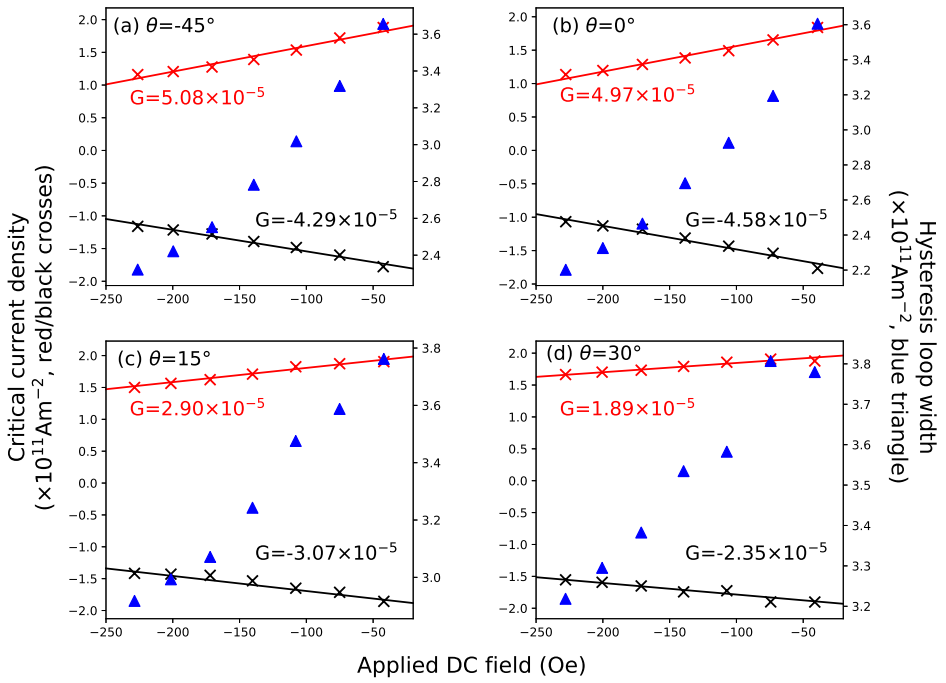

Figure 6.11: The positive and negative critical current densities, together with the associated half loop width, for current-induced magnetic reversal hysteresis loops. Each sub-figure contains data from seven hysteresis loops taken varying magnitudes of the DC magnetic field. The magnetic field is applied at an angle of $\theta = -45°, 0°, 15°$ and $30°$ for figures (a-d) respectively. The gradient, G, of the critical current density with respect to the applied DC field is shown on for each hysteresis group.

or charge current amplitude. First, the Oersted field alone can be ruled out as the cause. The transverse Oersted magnetic field within a uniform current carrying thin film of infinite length and width can be approximated by [140],

$$H_{\mathrm{Oe}} = \frac{2\pi J_{\mathrm{c}}}{10^3}\left(\left|z - \frac{l_z}{2}\right| - \left|z + \frac{l_z}{2}\right|\right) \tag{6.5}$$

where H_{Oe} is in Oersteds, z is the distance from the centre of the wire and l_z is the thickness of the wire. For the Hall bar of structure Pt(1 nm)/Co(0.6 nm)/Pt(4.4 nm), $|H_{\mathrm{Oe}}| \approx 8$ Oe at the location of the Co layer for the highest current density used within this chapter ($3.75 \times 10^{11}\mathrm{Am}^{-2}$). While the magnitude of the Oersted field is greater than the lowest applied field for which current-induced magnetic rever-

sal was observed (< 5 Oe), the direction is always transverse to the current flow ($\theta = 90°$). When an external field of up to 240 Oe was applied along this direction, no current-induced magnetic reversal was observed, hence, this suggests that the magnitude of the Oersted field alone is insufficient to cause the observed changes. The Oersted field can, however, induce field-free magnetic reversal if the orthogonality of the Oersted field and charge current is broken, details of which are within chapter 5.

Another possibility is the misalignment of the external field across multiple measurements. Synchronising the coordinate systems of the magnet and the Hall bar involved the use of optical bench elements and a camera in order to view the micron scale Hall bar. With the addition of each optical element within the MOKE system, a possible source of alignment error is introduced resulting in an uncertainty of the true angle of the Hall bar. For each measurement, the sample was aligned such that it is orientated horizontally when viewed with the camera, which, due to the alignment errors, is not necessarily horizontal with respect to the optical bench ($\theta = 0°$). Therefore, a finite error within the θ alignment is introduced. For out-of-plane (ϕ) misalignments, the magnet was positioned by eye using the substrate and pole tips as the reference.

The error in the angular alignment is estimated to be approximately 2° in both θ and ϕ. While this magnitude of field alignment error is not expected to produce significant additional field components alone, when coupled with a low field quality, these components may become non-negligible. The pole pieces of this magnet are of 3 mm in diameter and are separated by 40 mm. The low pole size to pole gap ratio produces only a very small good field region. Outside of this region, the field profile will not be a pure dipole field, hence, there exists small additional field components. The sum of both the additional field components due to the magnet misalignment and those arising from poor field quality may be of sufficient magnitude to induce the asymmetry observed in the critical current density. The random nature of the observed asymmetry is also accounted for as the magnet is manually realigned between measurements. The following section details the impact of incorrect effective field measurements on existing studies within the literature.

6.4.6 Implications on existing studies

Earlier within this chapter, it was highlighted that the effective field should be linear with respect to the applied magnetic field strength for all values. However, the data for the sample used here showed a distinct transition between a zero and finite gradient region within figures 6.6 and 6.9. This is attributed to the sample having

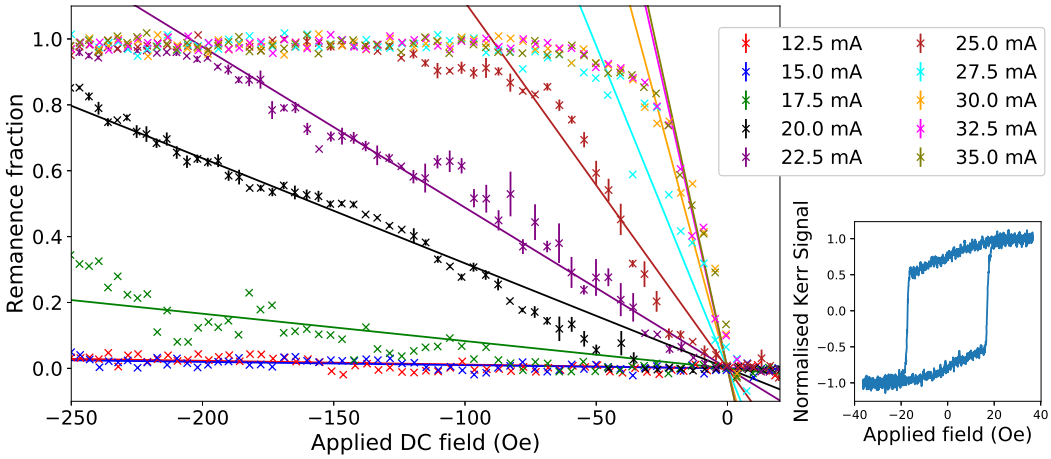

Figure 6.12: Remanence fraction data for a Pt(0.5 nm)/Co(0.6 nm)/Pt(4.5 nm) sample. Linear trend lines have been added for each unique charge current value. The polar field MOKE hysteresis loop showing a non-unity remanence is shown in the inset.

unity remanence within a standard field switched MOKE hysteresis loop. If the sample has a remanence value in between 0 and 1, the transition between regions with differing gradients disappear and the current-induced remanence fraction becomes linear across all regions.

Figure 6.12 shows the remanence fraction as a function of applied field magnitude for a sample with a polar field MOKE hysteresis remanence value of approximately 0.8. As the remanence fraction is less than one, there exists some magnetic reversal even for the smallest applied magnetic fields, contrary to samples with square hysteresis loops whereby the threshold equal to the coercive field must be reached. The presence of magnetic reversal at low fields removes the transition between zero and finite gradient regions within the remanence fraction data. As the data are now consistently linear for all applied magnetic fields, this is consistent with the effective field measurement method and would, therefore, be indistinguishable to true effective field measurements.

6.5 Conclusions

This investigation studied the impact of current-induced magnetic reversal on SOT effective field measurements within a perpendicularly magnetised Pt/Co/Pt Hall bar. The common methodology of AC modulation of the effective fields through the use of an AC charge current was modified to use the remanence fraction. When

compared to first or second harmonic lock-in amplifier signals, the remanence fraction allows for the isolation of any signal component which originates from magnetic reversal and does not measure the true effective field signal.

The Hall bar displayed current-induced magnetic reversal at various magnetic field strengths (up to 240 Oe) and charge current densities in the range of $1 - 4 \times 10^{11}\text{Am}^{-2}$. The direction of magnetic reversal changed when either the magnetic field or charge current polarity was reversed, as expected. While the magnetic field vector remained parallel to the charge current, the remanence fraction can be measured as a function of the applied magnetic field strength. The gradient is proportional to the damping-like effective field strength, whereby a value of $H_{\text{DL}} = 46 \pm 2$ kOe at $1 \times 10^{11}\text{Am}^{-2}$ was measured. This value is approximately three orders of magnitude greater than the literature accepted value of 50-100 Oe.

The effective field was measured with the external magnetic field applied at various angles with respect to the charge current. When the magnetic field and charge current are perpendicular, the effective field measured equals the field-like effective field. Due to the lack of inversion asymmetry, the Rashba effect is minimised and no field-like effective field was expected. However, due to the lack of suitable data within the region of $\theta = 90°$, a value of $H_{\text{FL}} = 4 \pm 2$ kOe at $1 \times 10^{11}\text{Am}^{-2}$ was obtained.

In samples of unity remanence, it has been shown that it may be possible to identify if current-induced magnetic reversal has occurred if there exists a transition between a near zero and finite gradient region. However, if the sample does not have unity remanence, it was shown that this transition disappears and the symmetry of the remanence fraction now matches what is expected of the true effective fields. The identical measurement symmetries, together with the enormous false effective field strengths measured, create the potential for current-induced magnetic reversal to greatly impact on the effective field measurements. For samples which possess a non-square hysteresis loop, this false effective field contribution can be undetectable.

Chapter 7

Magnetic and structural interface changes in Pt/CoFeTaB/Ir and its structural inverse

7.1 Introduction

Heavy metal/ferromagnetic structures have been extensively studied for their use in spintronic devices [38, 144, 159–173]. Heavy metals, which display strong spin-orbit coupling, have been used to generate spin currents in order to influence an adjacent ferromagnetic layer [174–176]. This phenomena formed the basis of chapters 5 and 6. More broadly, heavy metal/ferromagnetic structures have been studied for spin pumping [144, 159–162], spin Hall magnetoresistance [163–166], spin Seebeck effect [167–169], Dzyaloshinskii-Moriya interaction [170–172] and spin mixing conductance [38, 173].

Within these structures, the interface plays a key role in the observed effects [170, 177]. Structures comprised of Ta/CoFeB/MgO exhibit perpendicular magnetic anisotropy and are a promising candidate for commercial magnetic random access memory devices [178]. Within these structures, the Ta/CoFeB interface places a key role within the magnetic anisotropy, however, the structurally inverted thin film of MgO/CoFeB/Ta does not behave equally. Cheng *et al* show that the perpendicular magnetic anisotropy is much more sensitive to the Ta layer thickness in CoFeB/Ta structures compared to Ta/CoFeB [179]. For larger Ta cap thicknesses, the cause of the deterioration in perpendicular magnetic anisotropy strength is attributed to increased Ta diffusion and the formation of a magnetic dead layer. Understanding CoFeTaB thin-films will, therefore, allow for the greater understanding of other structures that exhibit Ta diffusion and magnetic dead layer formations.

Efforts have been made to engineer interfaces in order to improve device performance [180–182]. In other areas, interface variations have been utilised in order to study physical effects that originate from the adjacent layers [183–186]. One such study investigates the proximity-induced magnetisation in Pt/CoFeTaB/Pt trilayer structures, where the degree of spin polarisation in Pt changes by a factor of 10 for Pt/CoFeTaB interfaces compared to CoFeTaB/Pt [187]. Inyang *et al.* further show that the local composition of the amorphous CoFeTaB varies across the layer, with the subsequent interfacial magnetisation values being considerably higher than that of the bulk layer. Variations in alloy composition have also been studied in similar ferromagnetic layers for their impact on various sample properties in systems of CoFeTaB [188], CoFeB [189–191] and CoFe [192–194]. Annealing procedures are often included during the fabrication of thin films in order to modify sample properties [157, 195, 196]. Such procedures can also cause particular elements to diffuse more easily than the other elements within alloys, such as the formation of a B-Ta intermediate layer in CoFeB/Ta structures [188] or a Fe-O intermediate layer in CoFeB/MgO structures [197]. Both Pt/CFTB/Ir and Ir/CFTB/Pt structures were annealed at 300 °C for one hour under vacuum in order to investigate the possibility of preferential diffusion within the CoFeTaB alloy. Overall, knowledge of the interfacial properties within thin film structures is of utmost importance in order to understand the variations in reported numerical results and for the optimisation of future spintronic devices.

This chapter aims to extensively characterise the differences in both the structural and magnetic properties of Pt/CoFeTaB/Ir compared with its structural inverse of Ir/CoFeTaB/Pt. The chapter begins by investigating the depth-resolved density profile through the use of specular and off-specular X-ray reflectivity. To further quantify the interfacial properties, energy dispersive X-ray measurements are presented for the Pt/CoFeTaB/Ir sample. After the sample structure has been thoroughly quantified, the magnetic performance is evaluated through the use of polarised neutron reflectivity, MOKE and vibrating sample magnetometer measurements.

7.2 Structural properties

CoFeB is an amorphous alloy with a Curie temperature on the order of 1000 K [198, 199]. Doping the alloy with a transition metal such as Ta reduces the magnetic moment of the Fe atoms as well as the overall Curie temperature [200, 201]. By tuning the composition of the alloy, it is possible to obtain a Curie temperature of

approximately room temperature. This occurs at a composition of $Co_{32}Fe_{32}Ta_{20}B_{16}$ (hereby referred to as CFTB).

A total of four samples were used within this chapter; two trilayer samples of as-deposited Pt(3 nm)/CFTB(10 nm)/Ir(3 nm) and Ir(3nm)/CFTB(10nm)/Pt(3nm) together with two nominally equivalent structures annealed at 300 °C for one hour in vacuum. The samples were deposited onto a 20 mm × 20 mm substrate to ensure a good signal to noise ratio for the polarised neutron reflectivity (PNR) measurements. While MOKE and laboratory based X-ray reflectivity (XRR) studies were performed on the larger samples, the size was incompatible with vibrating sample magnetometer (VSM) and energy dispersive X-ray (EDX) measurements, hence, the samples were cut down post PNR measurements.

7.2.1 Specular X-ray reflectivity

XRR is a non destructive technique which determines the depth-resolved density profile of the sample. All four samples were measured as per the methodology presented within chapter 3 with the data, best fit models and resultant scattering length densities (SLD) shown in figure 7.1. The annealed sample SLD profiles are not shown as they are qualitatively indistinguishable from the as-deposited results.

The layer thickness, density and interface roughness are all encoded within the Kiessig fringes of the reflectivity profile. Taking the Pt/CFTB/Ir sample as an example, a dominant fringe periodicity is observed with a spacing of approximately 0.6°. The corresponding thickness, t, of the layer responsible for these fringes can be approximated by,

$$t = \frac{\lambda}{2(\sin(\frac{\theta_1}{2}) - \sin(\frac{\theta_2}{2}))}, \tag{7.1}$$

where λ is the wavelength of the X-rays (1.54 Å) and $\theta_{1(2)}$ is the value of 2θ for the Kiessig fringe minima. As the Kiessig fringes are separated by 0.6°, this equates to a layer thickness of 14.7 nm, which is approximately equal to the nominal total film thickness of 16 nm. There also exists a more subtle variation in the Kiessig fringes, where the depth of the fringe varies with a period of approximately 2.8°. The Kiessig fringes are much sharper at 2θ values of 3.2° and 6° compared to the adjacent fringes, which corresponds to a film thickness of 3.2 nm. Inspection of the Ir/CFTB/Pt data also reveals the same dominant periodicity of 0.6°, however, the less dominant Kiessig fringe features appear at a different point in 2θ. The deeper Kiessig fringes appear at approximately 2.4° and 5.5°, equating to a similar thickness

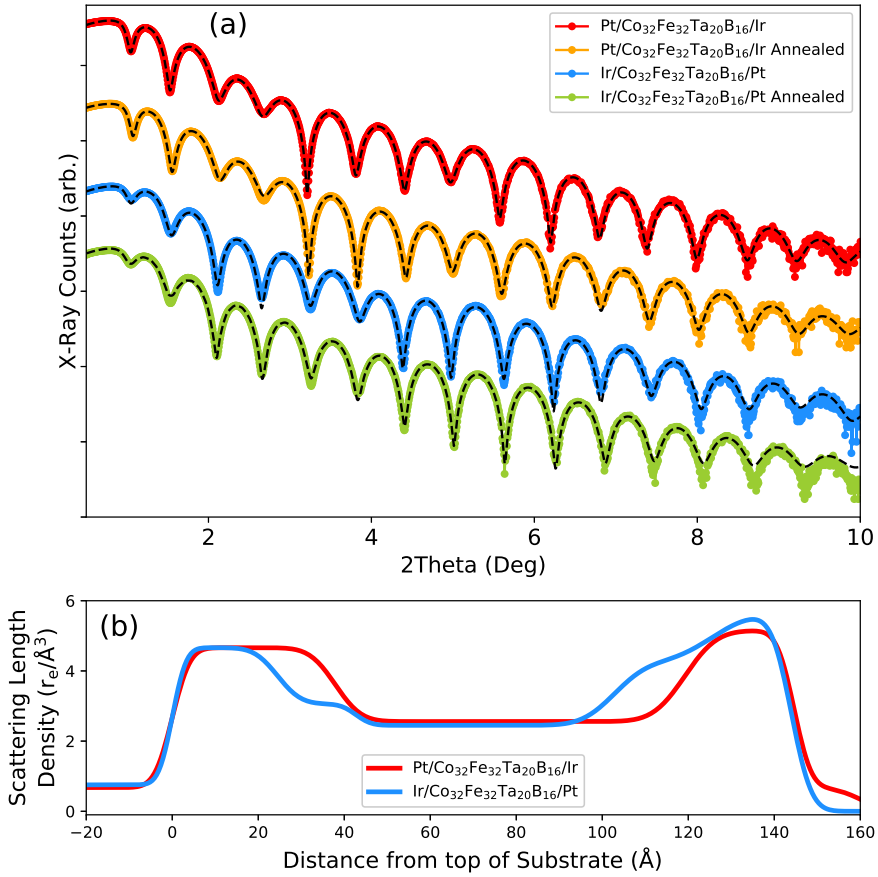

Figure 7.1: (a) XRR measurements along with their associated best fit models (dashed lines) for each sample. An offset has been added to each measurement for clarity. (b) The resultant SLD profiles for the as-deposited samples.

of 2.9 nm. The variation in Kiessig fringe depth is also less pronounced than that of Pt/CFTB/Ir, therefore, while the data for both samples indicate the presence of a layer with the approximate thickness of 3 nm, this layer is not necessarily identical between structures.

While the nominal thicknesses of the sample layers are 3 nm, 10 nm and 3 nm, it is clear from the SLD results that the actual layer thicknesses deviate from the nominal values. Inspection of the red, Pt/CFTB/Ir data set gives approximate thicknesses of 3.8 nm, 8.1 nm and 2.5 nm respectively (these values are also tabulated in table 7.1). These differences are attributed to growth rate calibration errors and do not impact upon the conclusions drawn from this chapter. The observed interface roughness values of 0.5 - 1 nm are typical of similar thin films. These numerical values extracted from the SLD profile correspond well with the visual analysis of the XRR profile. The dominant fringe spacing of 0.6°, which equates to a layer thickness of 14.7 nm, matches well with the total film thickness of 14.4 nm. The heavy metal layers have

	Lower HM (nm)	CFTB (nm)	Upper HM (nm)
Ir/CFTB/Pt	2.4	7.8	4.1
Ir/CFTB/Pt Annealed	2.4	7.8	4.3
Pt/CFTB/Ir	3.8	8.1	2.5
Pt/CFTB/Ir Annealed	3.8	8.2	2.4

Table 7.1: Layer thickness extracted from XRR models. An error of approximately 3 % is attached to each of the simulated parameters.

an average thickness of 3.25 nm which is approximately equal to that predicted from the Kiessig fringe depth variations. The fact that there is an asymmetry within the heavy metal layer thickness, and that the interfaces within the Pt/CFTB/Ir SLD appear sharper than those in Ir/CFTB/Pt, explains the difference in position and prominence of the Kiessig fringe depth variations. In both cases, the data for the annealed samples are visually indistinguishable from the as-deposited counterparts.

For Ir/CFTB/Pt, a more complicated SLD profile is observed with the introduction of intermediate layers between the CFTB layer and both heavy metal layers. When modeling the XRR data, initial models consisted of only three layers with each respective thickness and density set to the nominal values. The parameters were allowed to vary by up to 2.5 nm (thickness) and 15 % (density) to allow for thin film growth variations, however, a good fit model could not be obtained. Subsequently, intermediate layers were introduced individually to asses their impact on the quality of the fit, with the addition of two intermediate layers on either side of the CFTB layer providing the optimal fit with the least additional parameters.

The physical interpretation of the intermediate layers can take multiple forms. First, the model assumes a smooth, symmetric and Gaussian like interface, however, this is not necessarily true in practice. Effects such as roughness, intermixing and alloying may vary in magnitude across the interface creating a depth varying density profile. The X-ray beam used is 1 cm wide, therefore, the measured thickness is an average over a large area of the sample. Any variations of the layer thickness across the sample would be represented by an extended interface region. Finally, alloying may occur at the interface, creating regions where the local alloy composition differs from the bulk layer. Without complementary investigative techniques, it is not possible to distinguish the exact cause of the observed results from XRR measurements alone.

There is a lower limit to the observable layer thickness within XRR of approximately 0.5 - 1 nm, whereby approaching this limit decreases the observable features of this particular layer. Evidence of this was presented previously within chapter 5, figure 5.3, where results showed a minor SLD variation within the nominal region

	X-ray Scattering Factor (r_e)	Density (g/cm^3)	SLD (r_e/Å^3)
Platinum	73.7	21.4	4.9
Cobalt	24.6	8.9	2.2
Iron	24.8	7.9	2.1
Tantalum	67.5	16.6	3.7
Boron	5.0	2.3	0.7
Iridium	72.6	22.6	5.1

Table 7.2: Nominal X-ray scattering parameters for each element. The SLD is proportional to the product of the scattering factor and density.

of a 0.6 nm thick Co layer. However, it was not possible to determine if the density increased or decreased, and over what length scale this occurred. In the context of Pt/CFTB/Ir, the intermediate layers suggest that something occurs at the interface, for example, a variation in CFTB alloy composition or the intermixing of Ir (or Pt) within the alloy. Since this layer is of the order of the minimum observable feature within XRR, quantitative analysis of this region will come with increased errors in comparison to quantitative conclusions upon the bulk Pt, CFTB or Ir layers.

At this stage, it is not clear as to the reason why the structure of Ir/CFTB/Pt requires intermediate layers to model the XRR profile while Pt/CFTB/Ir does not. During the deposition process, the experimental parameters (such as target power, gas pressure, etc.) for the deposition of each element/alloy were consistent between samples. Each material was deposited onto the sample shutter for a period of time immediately prior to the sample deposition in order to clear any surface oxidation from the sputter target. It is expected that growth errors did not contribute to the observed results, therefore, attention turns to other sources.

The observed SLD is equal to the product of the local density and the X-ray scattering factor. Table 7.2 shows the X-ray scattering factors, bulk densities and the SLD for each element. The observed SLD magnitudes in figure 7.1 match well with the theoretical values. While XRR is not a full element specific technique, it is possible to rule out certain elements as the cause for intermediate layers from their SLD value. For both the Ir/CFTB and CFTB/Pt intermediate layers, it is clear that the SLD value is intermediate with respect to the SLD value of the bulk CFTB and heavy metal layers. We can, therefore, rule out the possibility of these intermediate layers being B rich due to its low X-ray scattering factor and density. The SLD of Pt, Ir and Ta is also much greater than that of Co and Fe, suggesting that either a small increase in the local Pt, Ir or Ta is required to increased the overall SLD value, compared to a considerable increase in Co or Fe concentration.

To investigate the interface structure in greater detail, the following section probes the atomic composition of the Pt/CFTB/Ir sample through the use of energy dispersive X-ray measurements.

7.2.2 Energy dispersive X-rays

Energy dispersive X-ray (EDX) measurements were performed on the as-deposited Pt/CFTB/Ir sample. To facilitate the measurements, a conventional transmission electron microscope specimen was created in a FEI Helios Nanolab 600 focused ion beam system using the methodology described by Giannuzzi *et al.* [202]. After transferring the sample to a JEOL 2100F FEG transmission electron microscope, a focused electron beam is scanned across the sample. The accelerating voltage used was 200 kV at normal incidence to the sample. The electron beam provides the energy required to promote an electron from an inner shell within a host atom in the sample. It is then possible for an outer shell electron to fill the electron hole, emitting electromagnetic radiation during the process. The energy levels of the electron shells are discrete, therefore, the energy of the radiation emitted when an outer electron fills an inner electron hole is also discrete. The element selectivity of EDX measurements is achieved by comparing the energy of the emitted X-ray with known values for particular elements, hence, the sample composition can be directly measured.

Figure 7.2 shows the raw electron microscope image (right) of the lamella, to-

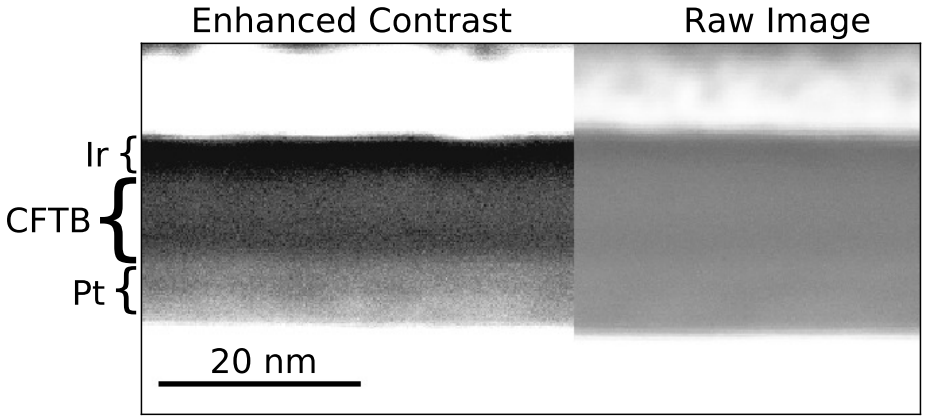

Figure 7.2: Transmission electron microscope image of the Pt/CFTB/Ir lamella. The raw image is shown on the right hand side which shows faint differences between sample layers. The contrast within the left hand image has been optimised post image acquisition such that the full contrast range extends over the sample region only, hence, the adjacent substrate and surface coating layers appear as a saturated white colour.

gether with an enhanced contrast image (left) for the sample area. The three individual sample layers can be clearly seen, together with some additional features. The Pt layer appears thicker than the Ir layer, consistent with the previous XRR results. Within the CFTB layer, there exists a darker stripe at the Pt interface, suggesting that the CFTB layer is not uniform in composition and/or density. This change was not observed within the XRR measurements.

Figure 7.3(a) and (b) show the normalised X-ray count rate for Fe and Pt as a function of distance from the substrate. The scanning direction is from the lower to upper edge of figure 7.2. Due to the limitations of the instrument used, it is not always possible to distinguish between the spectral lines of different elements. Figure 7.3(a) clearly shows both the lower and upper limits of the Fe region within the sample, however, figure 7.3(b) only displays a lower Pt interface. Modeling of the data involved fitting an error function by method of least squares to all regions which showed a clear transition of element abundance. Figure 7.3(c) shows the results of the data modeling for all elements except B. Due to the lack of a suitable spectral peak, it was not possible to acquire any data for the local B abundance.

Comparing the locations of the 50 % position when moving from left to right (deep within the trilayer structure towards the surface) within figure 7.3, it is clear that the seed layer consists of only Pt. Approximately 3 nm later, Fe and Co cross the 50 % mark at almost the same position. Although deposited as one complete layer, the Ta signal occurs 2-3 nm later than that of Fe and Co, suggesting that the interface region between Pt and CFTB is Ta deficient. This coincides with

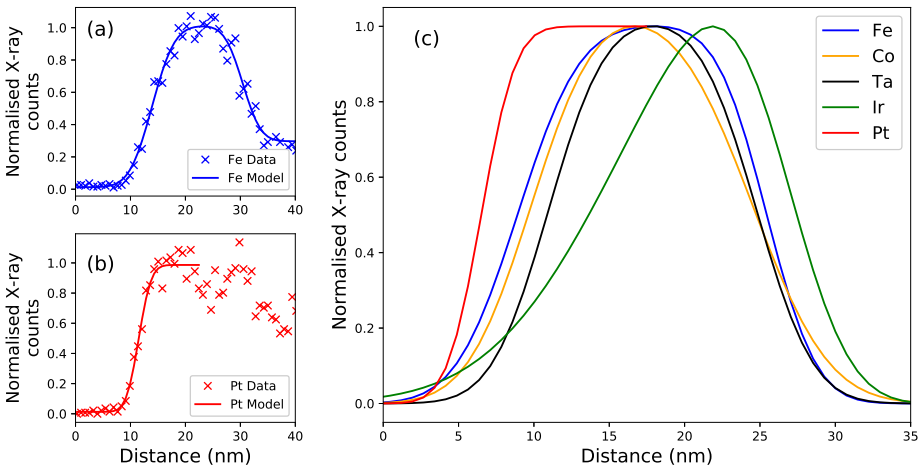

Figure 7.3: EDX measurements, together with error function models for the determination of the interface locations for Fe (a) and Pt (b). (c) Interface models for all elements (excluding boron) as a function of sample position.

the sample image in figure 7.2, where the CFTB layer appears to have partially separated. At the upper CFTB interface, the transitions of Co and Ta coincide, with Fe occurring less than 1 nm later. While this may suggest a thin Fe rich region at the CFTB/Ir interface, this region is not as pronounced as the composition variation at the Pt/CFTB interface. It was not possible to obtain EDX measurements upon the structurally inverted sample, however, the following section details off-specular XRR measurements on all samples in order to investigate any differences within the interfaces.

7.2.3 Off-specular X-ray reflectivity

Rocking curve XRR measurements allow for the the relative contributions of interface roughness and intermixing to be quantified. A detailed methodology has been presented previously in chapter 3. Figure 7.4 shows the specular XRR data along with two rocking curves for the as-deposited Pt/CFTB/Ir sample. The specular and off-specular data have been modeled simultaneously in order to confirm the validity of the resultant structure.

The resultant interface roughness and intermixing values for all samples are pre-

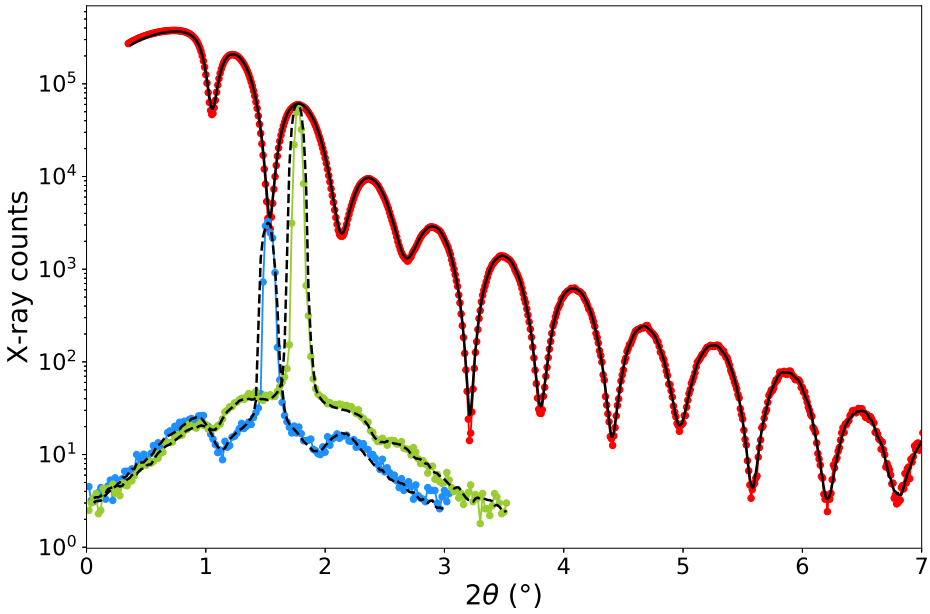

Figure 7.4: Specular XRR measurements (red) along with two rocking curve measurements at a 2θ detector angle of 1.54° (blue) and 1.90° (green). Best fit models (dashed and solid lines) were obtained from simultaneous specular and off-specular data fitting.

sented in table 7.3. The results indicate a clear difference within the structurally inverted interfaces, namely Pt(Ir)/CFTB interfaces are roughness dominated and CFTB/Pt(Ir) interfaces are dominated by intermixing. The observed result may be due to differences in the energy of sputtered atoms/clusters within the deposition process. Magnetron sputtering is a high energy deposition method, whereby sputtered atoms/clusters from the target material can re-sputter the sample surface and/or cause ion implantation under the surface if their kinetic energy is great enough [203]. Since the mass of Pt and Ir is greater than that of the average of Co, Fe, Ta and B, it is possible for sputtered Pt and Ir atoms/clusters to carry more kinetic energy than the average atom/cluster in sputtered CFTB. This higher energy would produce the observed intermixing dominated interface for CFTB/Pt(Ir). At the lower interface, the lower energy of CFTB sputtered atoms/clusters cannot be implanted as deeply within the Pt(Ir) layer, hence, this layer is roughness dominated.

Structural measurements have shown there to be large and observable differences within structurally symmetric, yet inverted thin films. Opposing interfaces can change from roughness to intermixing dominated, while variations in alloy composition are observed between regions in the immediate vicinity of the interface compared to that in the bulk layer. The following section investigates whether the observed structural changes impact upon the depth profile of the magnetisation.

	Pt/CFTB	Ir/CFTB	CFTB/Pt	CFTB/Ir
	As-Deposited			
Interface Roughness (Å)	4.1	4.0	3.0	2.9
Interface Intermixing (Å)	2.4	3.1	6.0	5.4
	Annealed			
Interface Roughness (Å)	4.2	4.1	3.0	3.0
Interface Intermixing (Å)	2.6	3.1	6.1	5.3

Table 7.3: The relative interface roughness and intermixing contributions for both the as-deposited and annealed structures, indicating a difference in the local interfacial environments between inverted interfaces. An error of approximately 3 % is attached to each parameter extracted from the simulation.

7.3 Magnetic properties

Polarised neutron reflectivity (PNR), MOKE and vibrating sample magnetometer (VSM) techniques were used to measure the magnetic properties of all four samples considered in this chapter. All measurements were performed on each individual sample, with the measurement order chosen such that the techniques which benefit from large samples (PNR) were performed before the samples were cut into smaller sizes. The VSM and MOKE techniques involved narrow bore cryostats, hence, it was not possible to use the larger sample size in all measurements.

7.3.1 Polarised neutron reflectivity

PNR measurements were performed at the PolRef beamline at the ISIS neutron source. A full description of the technique is presented in chapter 3. Here, the neutron reflectivity profile was measured at four temperatures for each sample under an in-plane saturating external field of 1000 Oe. The coercivity of all films was confirmed to be less than 100 Oe at all temperatures through MOKE measurements.

PNR is often used as a complementary technique to XRR due to the differing SLD scaling for different elements. The neutron scattering factors and resultant SLD values are shown in table 7.4, with a comparison to the X-ray SLD values shown in figure 7.5. Since X-ray scattering factors are proportional to the atomic number, XRR measurements provide a good contrast between elements of differing atomic numbers. However, neutron scattering factors are quasi-random which can give rise to a contrast between similar elements. For example, Co and Fe differ in atomic number by one and have a similar mass density, which results in almost identical X-ray SLD values. However, the neutron SLD values differ by a factor of 3.5.

The PNR data along with the best fit models are shown on the left hand side of figure 7.6, with the associated asymmetry profile shown on the right hand side. A

	Neutron Scattering Factor (fm)	Density (g/cm^3)	SLD (fm/Å^3)
Platinum	9.6	21.4	0.63
Cobalt	2.5	8.9	0.23
Iron	9.4	7.9	0.80
Tantalum	6.9	16.6	0.38
Boron	5.3	2.3	0.68
Iridium	10.6	22.6	0.75

Table 7.4: The nominal neutron scattering parameters for the elements used within the Pt/CoFeTaB/Ir structure.

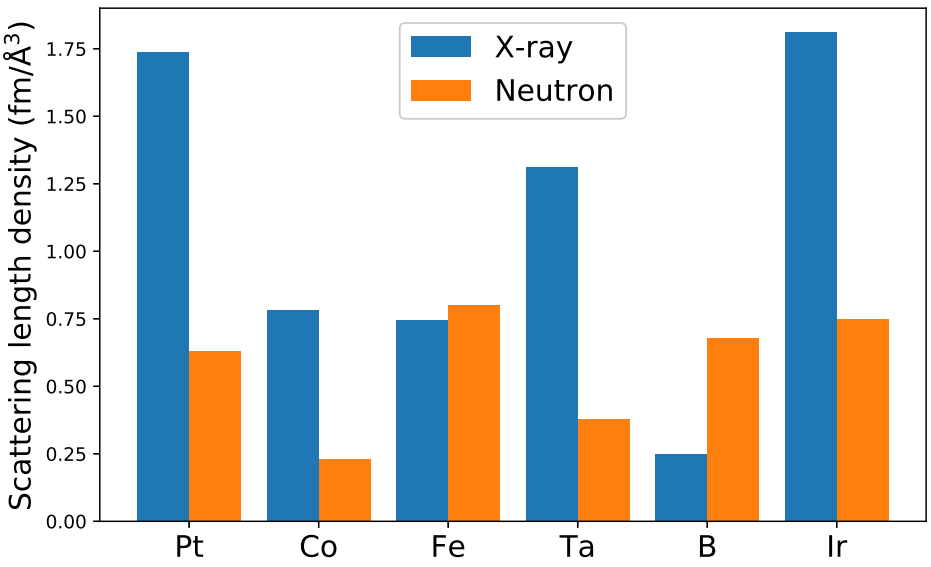

Figure 7.5: The variation in X-ray and neutron scattering parameters for each element used within this chapter. X-ray scattering factors are proportional to the atomic number, whereas neutron scattering factors are quasi-random, hence, contrast between different elements is achieved for the different techniques.

similar method to that used previously when visually analysing the XRR data can be employed for the PNR data. All measurements exhibit two large fringes in the range of 0.04 Å^{-1} $< Q <$ 0.13 Å^{-1}, which equates to a layer thickness of 14.0 nm. The higher frequency oscillations seen at Q values of less than 0.05 Å^{-1} are caused by the 100 nm thermally grown substrate oxide layer. The Kiessig fringes do not change position and/or depth as the temperature is varied, indicating no temperature-dependent structural changes. The only temperature-dependent change observed is a reduction in the magnitude of the asymmetry as the temperature is increased, indicating a reduction in the magnetisation.

The structural and magnetic SLD results from the best fit models are shown in figure 7.7. At the interface of Pt/CFTB, a small decrease in the CFTB structural SLD is observed across a 1.5-2 nm region. This region also exhibits a much larger magnetic SLD component when compared to the bulk CFTB layer. From the previous XRR and EDX measurements, it was suggested that this region is rich in Co and Fe along with a deficiency of Ta. Table 7.4 shows the neutron scattering factors for each element within the sample. Since the SLD value for Co is the lowest of all included elements, the reduction in the structural SLD is consistent with a Co rich interface region. This alloy composition variation has been observed in other

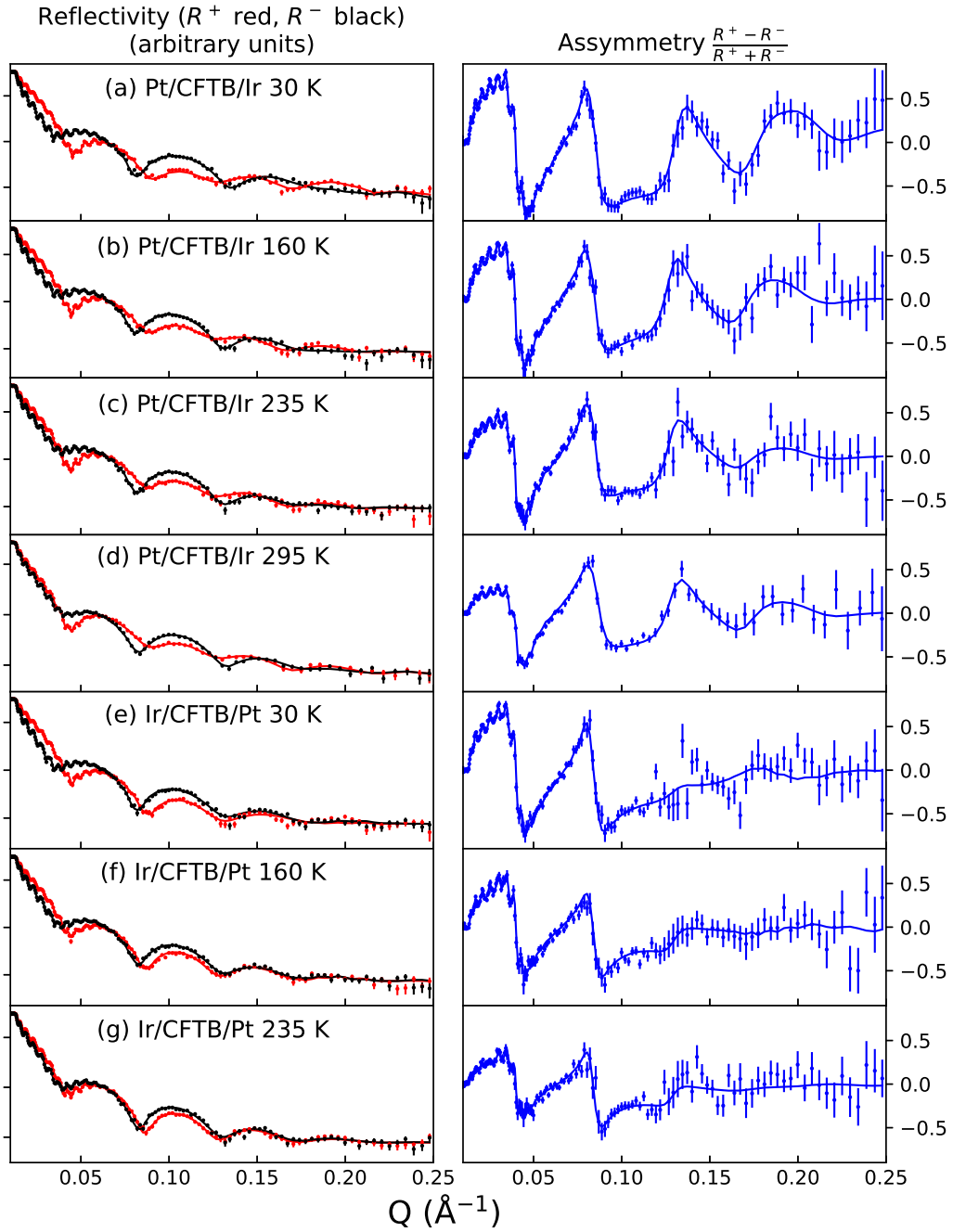

Figure 7.6: PNR data and their associated best fit curves (left) for the as-deposited samples at various temperatures. The 295 K measurement for Ir/CFTB/Pt has been omitted as the sample is not ferromagnetic at this temperature and does not display any magnetic asymmetry. A non-zero asymmetry (right) indicates the presence of ferromagnetism.

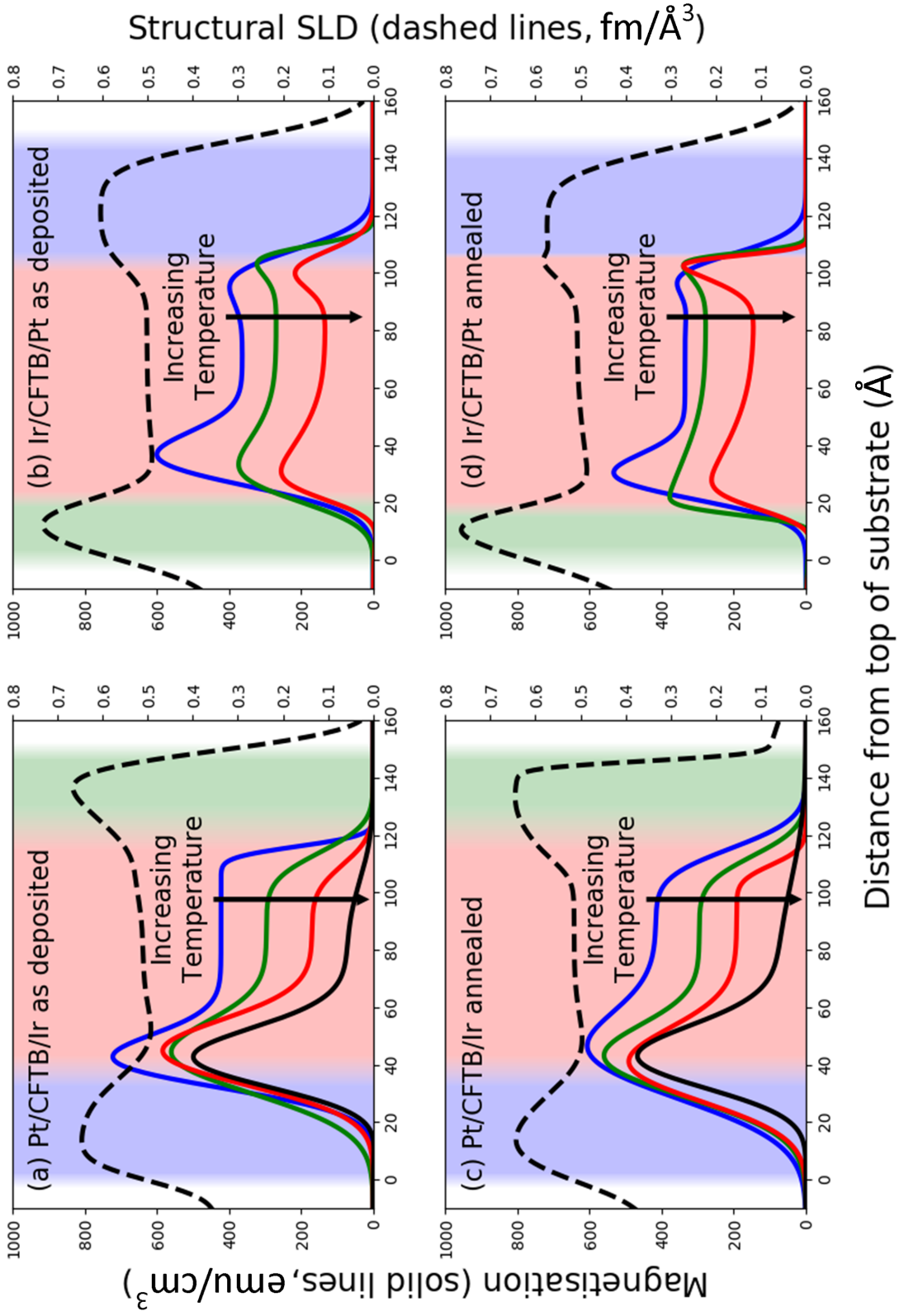

Figure 7.7: Extracted structural (black, dashed) and magnetic (solid) SLD profiles at 30 K (blue), 160 K (green), 235 K (red) and 295 K (black). The 295 K data for Ir/CFTB/Pt has been omitted due to the lack of ferromagnetism at this temperature. The background shading indicates the Pt (blue), CFTB (red) and Ir (green) regions, as determined from the structural SLD.

works [187], and may be attributed to different surface energy contributions from the differing elements within the CFTB alloy. It may be energetically favourable for Co and/or Fe to bond with the Pt layer, hence, causing Ta to diffuse away from the interface. This effect could be similar to that observed for Fe migration towards the interface in a CoFeB/MgO bilayer due to the preference of Fe-O bonding [197]. This Co and Fe rich and Ta deficient region should coincide with an increase of the local magnetisation, as observed in the magnetic SLD. Comparing the as-deposited and annealed Pt/CFTB interfaces, no differences are observed within the structural SLD while a slight reduction in the magnetic SLD is observed, particularly at low temperatures. It is thought that this is due to a small reduction in the extent of the Ta deficient region caused by increased intermixing, which is common when annealing thin films.

At the opposing CFTB/Ir interface, the opposite occurs, in which a slight increase in the structural SLD is observed, coupled with a reduction in the magnetic SLD. This observation is clearest in both the 160 K and 235 K data (green and red curves), where the value measured for the local magnetic SLD decreases to zero before the structural SLD magnitude increases, contrary to the case of Pt/CFTB where an overlap is observed. This can be explained with an increase in the local Ir concentration, as suggested by the increased intermixing observed at CFTB/Ir interfaces compared to Pt/CFTB in the previous off-specular XRR studies.

Turning the attention to the Ir/CFTB/Pt sample, a similar result is obtained for the lower Ir/CFTB interface when compared to that of Pt/CFTB. A small reduction is observed in the local structural SLD across a region of 1.5-2 nm. The magnetic SLD increases with respect to the bulk CFTB value, however, the temperature scaling differs to that of Pt/CFTB. Between 40 K and 235 K, the peak interface magnetic SLD for Pt/CFTB is reduced by 22 % (20 %) for the as-deposited (annealed) sample. For Ir/CFTB, this reduction is increased to 58 % (54 %). This suggests that the local Curie temperature of the Ir/CFTB interface is lower than that of Pt/CFTB, which may be caused by a greater concentration of Ta. While both interfaces are Ta deficient, Ir/CFTB is less deficient than Pt/CFTB. A more in-depth analysis of the magnetisation scaling with temperature is reserved for the following section after MOKE and VSM results have been presented.

Finally, the only remaining interface to study is CFTB/Pt. The structural SLD shows a similar increase in magnitude when compared to CFTB/Ir, consistent with Pt intermixing with the CFTB at the interface. In contrast to CFTB/Ir, an enhancement of the magnetic SLD occurs for CFTB/Pt, albeit to a lesser extent than that at the lower interface. This may be due to Co alloying more favourably to Pt

than Ir, however, such possibilities will be discussed in the following sections.

7.3.2 Temperature-dependent magnetometry

The Curie temperature was measured with the use of both a MOKE and a VSM instrument (Quantum Design MPMS 3). VSM measurements were performed in the temperature range of 30 K to 350 K, while MOKE measurements were obtained between 100 K and 300 K. Figure 7.8 shows MOKE results for three different temperatures for the Pt/CFTB/Ir as-deposited sample. As the temperature is increased, the magnetisation is reduced, as indicated by the reduction in the Kerr signal magnitude. Between measurements, all optical elements of the MOKE instrument are unchanged as to remove any Kerr signal variations bar that from the magnetisation change. The coercive field increases with decreasing temperature, as expected due to the lower thermal energy to aid magnetic reversal.

Figure 7.9 shows the normalised magnetisation results such that the measured magnetisation at 30 K is unity. This normalisation is required for two reasons. First, while MOKE measurements are, to a reasonable approximation, proportional to the magnitude of the magnetisation, quantitative values for the magnetisation cannot be obtained. Instead, relative differences can be measured if the optical setup remains identical such that the only variant between measurements is the magnetisation value. Secondly, MOKE, VSM and PNR measurements all probe different volumes of the sample, from 10's of microns (MOKE) to 10's of millimetres (PNR). Hence, if there exists some variance of sample properties across the sample, different tech-

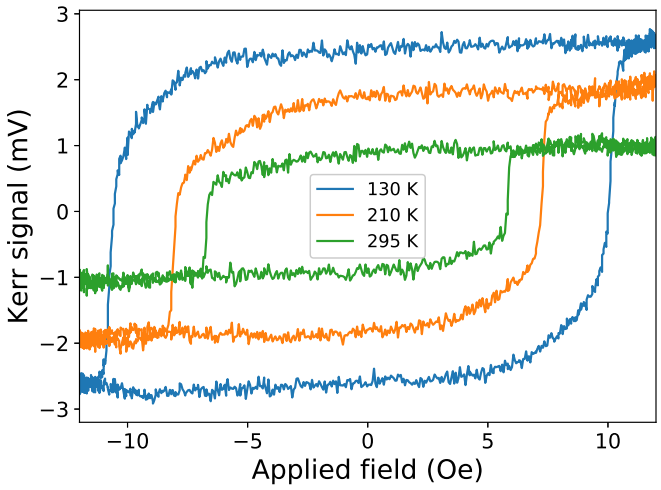

Figure 7.8: Longitudinal MOKE hysteresis loops for Pt/CFTB/Ir at three different temperatures. The experimental setup was kept constant in between readings, such that relative comparisons between Kerr signals could be made.

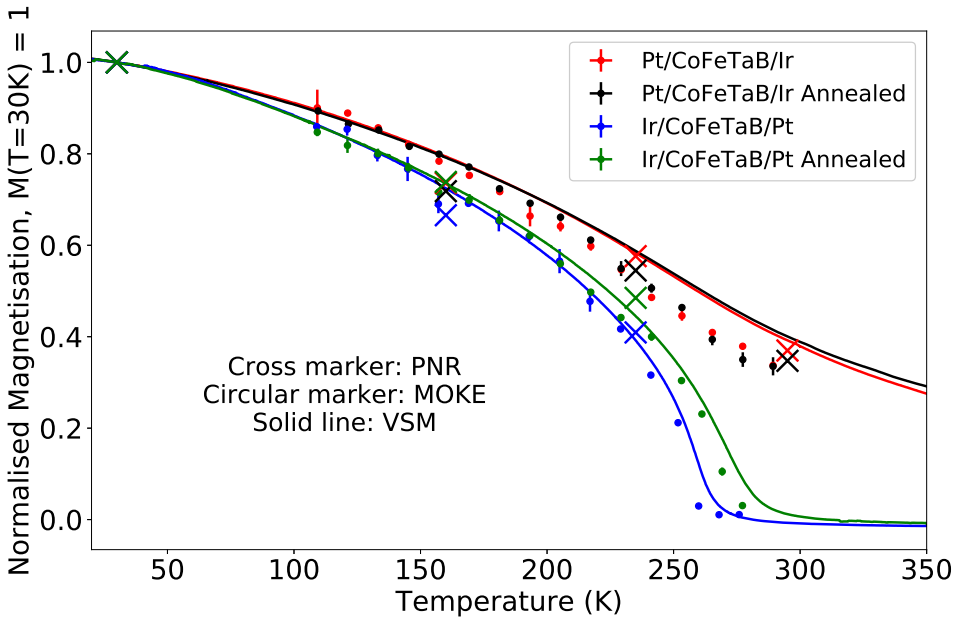

Figure 7.9: The magnetisation of all structures as measured by MOKE, VSM and PNR. The PNR data points were obtained from the integration of the magnetic SLD results.

niques may or may not be susceptible to such changes and the results obtained will vary accordingly. As it was not possible to obtain MOKE measurements at 30 K, the MOKE results have been normalised such that the signal equals that of the VSM data at 100 K.

The data presented in figure 7.9 are consistent between all techniques and across all samples. Ir/CFTB/Pt displays a relatively fast reduction in the magnetisation with increasing temperature which reduces to zero for a Curie temperature of approximately 265 K for the as-deposited sample. The annealed sample displays an increased Curie temperature of 275 K. The slight increase in Curie temperature of approximately 5 K for the VSM measurements when compared to MOKE data is attributed to local fluctuations in sample structure, thermometer calibration differences between instruments and differing measured quantities. While the MOKE method probes the local Curie temperature within a 20 μm region, VSM measurements require a sample that is approximately 3 mm by 3 mm. Any lateral variation of the local Curie temperature would, therefore, be averaged within the VSM measurements creating a smoother paramagnetic transition compared to that when measured by MOKE. The MOKE measurements were performed in a liquid nitrogen bath cryostat with a copper cryostat head. For accurate sample temperatures, both the sample and thermometer must be in good thermal contact with

the cryostat head. If this thermal connection was not perfect, the thermometer and sample may be at different temperatures, giving rise to a discrepancy between MOKE and VSM measurements. If this thermal connection is perfect, there is still the issue of differing thermometer calibrations across both systems which may also give rise to a small discrepancy. Finally, the MOKE data were extracted from the zero field Kerr voltage remanence, however, the VSM measurements involved a continuous temperature sweep at 10 K per minute in the presence of a small guide field of 100 Oe. The additional magnetic field-induced magnetisation within the VSM measurements could explain the additional signal observed in the region of the Curie temperature.

For Pt/CFTB/Ir, two regions within the magnetisation curve are observed. In the range of 30 K to 235 K, the magnetic signal is decreasing at an increasing rate. However, an inflection point is observed at 235 K, after which the rate of magnetisation decrease slows. This is consistent with the PNR results, where the interface and bulk magnetic SLD did not show equivalent temperature scaling in figure 7.7(a,c). Instead, the bulk CFTB magnetic SLD was reduced by 85 % in the range of 30 K to 300 K, whereas the interfacial magnetic SLD had only reduced by 25 % across the same temperature range. This suggests that the reduction in magnetisation from both VSM and MOKE measurements in figure 7.9 is dominated by the bulk CFTB layer in the range of 30 K to 235 K which has a Curie temperature near, yet above, 300 K. At approximately 235 K, the inflection point occurs when the bulk CFTB magnetisation is sufficiently reduced such that the interfacial magnetisation, which has a much higher Curie temperature, becomes the dominant contribution to the total magnetisation. This property creates a key difference between both samples, while the structures are nominally identical, inversion of the structure creates one sample which is ferromagnetic at room temperature, and one sample which isn't. From figure 7.9, the Curie temperature difference is expected to be in excess of 100 K. At 350 K, it is expected that the bulk magnetisation has reduced to zero for Pt/CFTB/Ir and that only interfacial magnetisation remains, if the trend observed in figure 7.7(a,c) of reducing bulk CFTB magnetisation continues.

	Pt/CFTB/Ir	Pt/CFTB/Ir Annealed	Ir/CFTB/Pt	Ir/CFTB/Pt Annealed
Magnetic Moment ($\times 10^{-5}$ emu)	6.840	12.714	10.345	8.047

Table 7.5: The magnetic moments as measured by SQUID magnetometry at 30 K. The large variance in measured values is likely due to the large differences in wafer size.

7.3.3 Ir doping of CoFeTaB

In section 7.3.1, it was stated that CFTB/Ir interfaces create a magnetic dead layer at temperatures above 160 K. To verify this, figure 7.10 shows temperature-dependent MOKE results for three samples of $CFTB_{1-x}Ir_x$(20 nm)/Pt(3 nm). The Ir doping was achieved by placing 5 mm diameter Ir discs onto the racetrack of the CFTB target during magnetron sputtering. This results in the sputtering of both materials, with the Ir concentration proportional to the relative area of the Ir chip to the underlying CFTB target. This methodology has been verified by EDX spectroscopy and was found to give accurate measurements (O. O.-Inyang, private communication). By measuring the ratio of covered against uncovered racetrack area, it is estimated that $x = 0$ %, 5 % and 10 % for the red, green and blue data sets respectively in figure 7.10.

By doping the CFTB with a small amount of Ir, it has been shown that the Curie temperature is reduced significantly. Since the off-specular XRR data shows that the CFTB/Ir interface is dominated by intermixing, it is thought that the magnetic dead layer within the CFTB layer is due to increased Ir intermixing rather than a Ta concentration increase. Inspection of the magnetic SLD data for the CFTB/Ir interface in figure 7.7(a) shows that the interface between finite and zero magnetisation changes with temperature. At 30 K, the reduction in magnetic SLD is sharp and occurs between the range of 112 Å and 120 Å. For higher temperatures, the lower position of the onset of the magnetic SLD interface occurs at a decreasing position. For 160 K, 235 K and 295 K, the initial point of magnetic SLD reduction occurs at 102 Å, 97 Å and 91 Å respectively. This is consistent with a composition gradient, where the differing local Curie temperatures due to the differing local alloy composition cause the magnetic interface to move as the temperature is varied.

The previous off-specular XRR results in section 7.2.3 indicate that the CFTB/Ir interface is intermixing dominated. From figure 7.10, it is evident that Ir concentrations of approximately 10 % are sufficient to reduce the Curie temperature to approximately 175 K. Using this data, it is estimated that the local Ir concentration would not be required to exceed 15 % over a 2 nm region in order to replicate the effects observed. This is further evidenced by the increase in structural SLD observed in figure 7.7 across the same region. Since the neutron SLD of Ir is twice that of Ta, and the interface is known to be intermixing dominated, the increase in structural SLD value, along with the magnetic dead layer, is highly likely to be caused by an Ir composition gradient within the CFTB interface region.

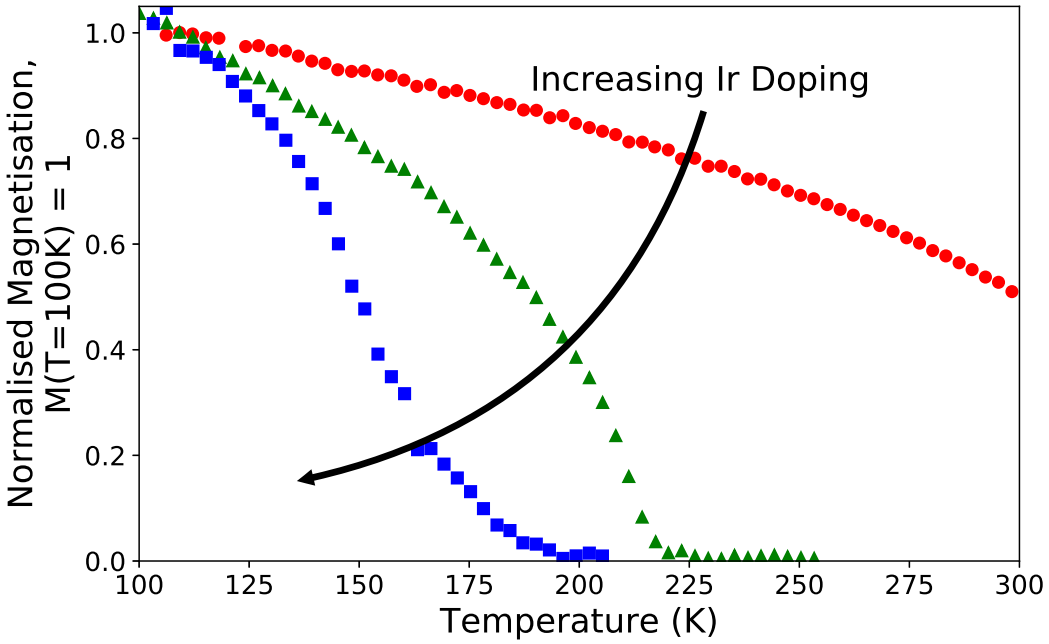

Figure 7.10: Normalised Kerr signal variations as a function of temperature for Ir doped CoFeTaB/Pt structures. The concentration of Ir within the red, green and blue data points is approximately 0 %, 5 % and 10 %.

7.4 Conclusions

Magnetic and structural variations of inverted trilayer structures were investigated through the use of PNR, specular and off-specular XRR, MOKE and VSM. Samples with a structure of Pt(3 nm)/CFTB(10 nm)/Ir(3 nm) and its structural inverse were studied as-deposited and after annealing at 300 °C for one hour.

The structural investigations reported two key differences. First, Pt(Ir)/CFTB interfaces are surface roughness dominated, whereas CFTB/Pt(Ir) interfaces are dominated by intermixing. It is thought that this difference is due to the energetic magnetron sputtering process, where the heavier Pt(Ir) atoms carry more kinetic energy when sputtered such that there is a higher likelihood of being implanted within the sample upon contact. Secondly, Pt(Ir)/CFTB and the inverted interface of CFTB/Pt(Ir) have differing affects on the CFTB region in the immediate vicinity of the interface. Pt(Ir)/CFTB produces a Ta deficient region extending approximately 1.5-2 nm into the bulk CFTB layer, however, no corroborated evidence of a Ta deficiency was observed for CFTB/Pt(Ir).

The observed structural differences also have an effect upon the magnetic behaviour of the trilayer samples. The Ta deficient region at the Pt(Ir)/CFTB interface produces both a higher magnetisation and Curie temperature when compared

to the bulk CFTB properties. This Ta deficiency is greater for Pt/CFTB than for Ir/CFTB. When the heavy metal is on top of CFTB, a difference between heavy metal choice is observed. The increased Ir intermixing within the CFTB interface region creates a magnetic dead layer above 160 K. The position of this magnetic dead layer extends further into the CFTB layer as the temperature is increased. However, for CFTB/Pt, the Pt intermixing produces a small magnetisation enhancement, possibly due to increased Co-Pt alloying.

The reported differences, both structurally and magnetically, can have a major impact on thin film studies where interface transport is important. Cecot *et al.* have shown that an interfacial magnetic dead layer in CoFeB/Ta interfaces reduces the perpendicular magnetic anisotropy of the system due to a suppression of the interface anisotropy contribution [204]. The reduction in perpendicular magnetic anisotropy can facilitate easier spin-orbit torque-induced magnetic reversal, since the switching threshold is inversely proportional to the square of the anisotropy field. In addition to anisotropy changes, Ta intermediate layers as thin as 0.5 nm have been shown to impact on the saturation magnetisation and damping within CoFeB/Ta/Pt systems [205]. In another study, the optimal critical current density for spin-orbit torque-induced magnetic reversal in CoFeB/Ta systems occurred when Ta intermixing was suppressed through the inclusion of Cu/Ag intermediate layers.

Applying this knowledge to the results shown here, it is clear that the differences observed in the structural and magnetic properties of Pt/CFTB/Ir and Ir/CFTB/Pt structures should have a considerable impact on spintronic devices. On the macroscopic scale, a change in Curie temperature of over 100 K means that room temperature spintronic devices are possible for ferromagnetic Pt/CFTB/Ir, yet not for paramagnetic Ir/CFTB/Pt. At lower temperatures, and on a microscopic scale, the local properties such as saturation magnetisation, DMI, damping and anisotropy will differ between inverted interfaces, hence, the underlying physics, along with any observed phenomena, is likely to be different at one interface compared to its structural inverse.

Chapter 8

Conclusions and future work

The design of a MOKE instrument has been presented, including the results of commissioning test. The instrument has been subsequently used to study spin-orbit torque effects in Pt/Co/Pt thin films and the structural and magnetic property variations in Pt/CoFeTaB/Ir trilayers.

8.1 Thesis conclusions

In chapter 5, the current-induced magnetic reversal of a Pt/Co/Pt rectangular bar was demonstrated, with and without an externally applied magnetic field. When an external magnetic field was applied, the switching behavior was typical of similar structures studied in the literature. When the external magnetic field was removed, deterministic bi-directional magnetic reversal was observed.

The Pt/Co/Pt sample was a rectangle with side lengths of 20 µm and 140 µm. Attached at either end were electrical contacts with a width of 60 µm and an overlap region of 20 µm. The sample was probed by raster scanning a MOKE laser spot across the sample in order to build a 2D Kerr remanence map from multiple hysteresis loop measurements. When the Hall bar was placed in the centre of the electrical contacts, the Kerr remanence map indicated two distinct Kerr voltage regions of opposite polarity, which were approximately equal in size.

Two further samples were investigated, where the Hall bar position was varied laterally with respect to the electrical contacts. Bi-directional switching was observed in all samples, but with different characteristics. As the Hall bar is displaced laterally towards the edge of the electrical contact, the switching region that is closest to the electrical contact centre grows in size and magnitude. When the Hall bar is parallel with the electrical contact edge, only a weak Kerr signal is observed on the side of the Hall bar that is furthest from the electrical contact centre.

The observed results did not match any existing methodologies for producing field-free current-induced magnetic reversal, hence, a new method involving the charge current Oersted field was proposed. By analysing current distribution studies within the literature, it is expected that the local current density is non-uniform throughout the thin film. In particular, the local current density is approximately uniform within the bulk electrical contact region, before funnelling into the Hall bar due to current crowding effects. This charge current funneling occurs both parallel and perpendicular to the sample plane. Oersted field simulations show that for the postulated charge current funnel, a non-zero magnetic field is generated parallel to the local charge current at the interface between Hall bar and electrical contact. This parallel field component is required for symmetry breaking in order to produce deterministic current-induced magnetic reversal. The spatial symmetry and polarity match the observed spatial pattern displayed by the Kerr remanence data. Simulations with Hall bars displaced laterally with respect to the electrical contacts were performed, which also match the spatial patterns of the Kerr remanence measurements. Therefore, field-free current-induced magnetic reversal starts with a nucleated domain at the interface between the electrical contact and Hall bar, where there exists a finite magnetic field parallel to the local charge current due to current crowding effects. This domain propagates along the length of the Hall bar, producing the observed spatially resolved Kerr remanence data.

Chapter 6 probed a common spin-orbit torque effective field measurement technique for its potential inaccuracies. A Pt/Co/Pt trilayer was used for this study. The technique involved measuring the oscillation of the magnetisation due to the AC effective fields produced by an AC charge current. The spin Hall effect predominately produces a damping-like effective field while the Rashba effect produces a field-like effective field. Since the Rashba effect requires structural inversion asymmetry, the effect should be minimised within the trilayer studied. As one Pt layer is much greater than the spin diffusion length of Pt and the opposing Pt layer thickness is lower than this length, a non-zero damping-like effective field was expected from the spin Hall effect. For accurate effective field measurements, the magnetisation must only tilt under the application of the charge current and no magnetic reversal should be present. This chapter studied the effect of unwanted magnetic reversal upon the resultant effective field strengths.

To isolate only the contributions from magnetic reversal, the Kerr remanence value of the MOKE hysteresis loops was chosen as a measure of the magnetisation oscillation. The Kerr remanence values for applied magnetic fields of up to 240 Oe and charge current densities in the range of $1 - 4 \times 10^{11}\mathrm{Am}^{-2}$ were measured.

By investigating the linearity of such Kerr remanence values with the applied field strength, the effective field strength can be calculated. Selectivity of the damping-like and field-like effective fields is achieved by applying the external magnetic field parallel and perpendicular to the charge current respectively.

Measurements indicated a damping-like effective field of $H_{\mathrm{DL}} = 46 \pm 2$ kOe at $1 \times 10^{11}\mathrm{Am}^{-2}$. This value is three orders of magnitude greater than the literature accepted value of $50 - 100$ Oe. A field-like effective field of $H_{\mathrm{FL}} = 4 \pm 2$ kOe at $1 \times 10^{11}\mathrm{Am}^{-2}$ was also obtained, however, due to the lack of data point density within the sensitive region, the field-like effective field measurement is unreliable.

In true effective field measurements, it was shown that the only identifying feature of unwanted current-induced magnetic reversal would appear as a distinct transition region for the gradient of the magnetisation oscillation amplitude as a function of applied magnetic field strength. However, this is only true for structures which display a near unity Kerr remanence. Measurements were performed for a sample with non-unity remanence, where this transition disappears and any unwanted current-induced magnetic reversal becomes undetectable.

In chapter 7, the temperature dependency of the structural and magnetic properties of Pt/CFTB/Ir and Ir/CFTB/Pt thin films was presented. The overall composition of the CFTB was $Co_{32}Fe_{32}Ta_{20}B_{16}$, which results in an amorphous alloy with a bulk Curie temperature of approximately 300 K.

Specular and off-specular XRR, PNR and EDX measurements all revealed structural variations within the trilayer thin films. First, off-specular XRR measurements revealed that ferromagnet/heavy metal interfaces are intermixing dominated while heavy metal/ferromagnet interfaces are roughness dominated. This is likely due to the energetic magnetron sputtering deposition process, where the heavier Pt and Ir atoms/clusters have a higher momentum than the average CFTB atom/cluster. Hence, Pt and Ir are more likely to be implanted into the sample surface creating an intermixed interface. Evidence of variations within the CFTB composition were also presented through specular XRR, EDX and PNR measurements. All techniques indicate a Ta deficient region of approximately 1.5 - 2 nm at the heavy metal/ferromagnet interface. However, no corroborated evidence of a Ta deficiency at the ferromagnet/heavy metal interface was observed.

The depth-resolved magnetisation was presented at 30 K, 160 K, 235 K and 295 K. It was shown that the Ta deficient region observed at heavy metal/ferromagnet interfaces, as indicated by the structural measurements, coincides with a substantial increase in the local magnetisation. However, for ferromagnet/heavy metal interfaces, a difference in heavy metal choice is observed. For CFTB/Pt, a moderate

increase in the local magnetisation is observed. It is thought that this is due to increased CoPt alloying in the intermixed interface region. For CFTB/Ir, a magnetic dead layer is observed which grows with increasing temperature. Temperature resolved MOKE data of Ir doped CFTB shows a decrease in Curie temperature for Ir concentrations of up to 10 %, which corroborates the conclusion of Ir intermixing being the cause of the observed magnetic dead layer.

The work in this thesis has furthered the knowledge of spin-orbit torque behaviour through demonstrating a novel technique for achieving field-free magnetic reversal. It has further presented a possible reason for the large discrepancies in spin-orbit torque quantities in the literature through false effective field measurements. It has been shown that careful sample engineering is required to achieve optimal devices, where significant structural and magnetic variations can occur after simple structure changes. Finally, this work has been achieved with the use of a purpose built MOKE instrument, where a detailed design report and commissioning results have been presented.

8.2 Future work

The field-free magnetic reversal presented in chapter 5 can be further explored with a systematic study of the electrical contact shape and size. This would allow for a greater understanding of the local current density distribution in the electrical contact. In particular, an electrical contact design which offers the option to apply the charge current through two unique electrical contact pathways, one with a charge current funnel and one without, would aid in confirming the methodology. It may also be possible to design a sample structure such that there exists an underlying conductive track which is insulated from the Hall bar above. A charge current can be applied to the underlying track in order to provide an Oersted field to the Hall bar, without contributing to the charge and/or spin current within the Hall bar. Quantification of the required Oersted field strength may then be possible through this method.

The effective field measurements presented in chapter 6 can be expanded on by investigating samples with various hysteresis loop shapes. This would further clarify which magnetic structures are particularly susceptible to measurement inaccuracies. This could include samples of differing ferromagnet and heavy metal elements as well as sample layer thickness.

Although the magnetic and structural variations in Pt/CFTB/Ir trilayers and its structural inverse was thoroughly investigated in chapter 7, the impact on spin-

related phenomena was not. This work could be extended to investigate the impact of the observed variations on the Dzyaloshinskii-Moriya interaction, spin mixing conductance, spin-orbit torques or other effects. The underlying cause of the Ta deficiency within the interfacial region of the CFTB layer was not fully concluded. Alloy stability studies and the interaction of CFTB with heavy metal seed layers could be further explored in order to understand the observed composition gradient. Studies involving various CFTB compositions and/or similar alloys such as CoFeB, CoFe, may also be beneficial to this investigation.

References

[1] M. N. Baibich, J. M. Broto, A. Fert, F. N. Van Dau, F. Petroff, P. Etienne, G. Creuzet, A. Friederich, and J. Chazelas, Physical Review Letters **61**, 2472 (1988).

[2] G. Binasch, P. Grünberg, F. Saurenbach, and W. Zinn, Physical Review B **39**, 4828 (1989).

[3] M. Julliere, Physics Letters A **54**, 225 (1975).

[4] J. Mathon and A. Umerski, Physical Review B **63**, 220403 (2001).

[5] T. Kishi, H. Yoda, T. Kai, T. Nagase, E. Kitagawa, M. Yoshikawa, K. Nishiyama, T. Daibou, M. Nagamine, M. Amano, *et al.*, in *2008 IEEE International Electron Devices Meeting* (IEEE, 2008) pp. 1–4.

[6] A. Schuhl and D. Lacour, Comptes Rendus Physique **6**, 945 (2005).

[7] Y. Huai *et al.*, AAPPS bulletin **18**, 33 (2008).

[8] K. Noma, M. Matsuoka, H. Kanai, Y. Uehara, K. Nomura, and N. Awaji, IEEE transactions on magnetics **42**, 140 (2006).

[9] A. Khvalkovskiy, D. Apalkov, S. Watts, R. Chepulskii, R. Beach, A. Ong, X. Tang, A. Driskill-Smith, W. Butler, P. Visscher, *et al.*, Journal of Physics D: Applied Physics **46**, 074001 (2013).

[10] X. Liu, K. Edmonds, Z. Zhou, and K. Wang, Physical Review Applied **13**, 014059 (2020).

[11] Z. A. Bekele, X. Liu, Y. Cao, and K. Wang, Advanced Electronic Materials **7**, 2000793 (2021).

[12] K. Belashchenko, A. A. Kovalev, and M. van Schilfgaarde, Physical Review B **101**, 020407 (2020).

[13] L. Zhang, X. Zhang, M. Wang, Z. Wang, W. Cai, K. Cao, D. Zhu, H. Yang, and W. Zhao, Applied Physics Letters **112**, 142410 (2018).

[14] N. Mikuszeit, O. Boulle, I. M. Miron, K. Garello, P. Gambardella, G. Gaudin, and L. D. Buda-Prejbeanu, Physical Review B **92**, 144424 (2015).

[15] M. Cubukcu, O. Boulle, N. Mikuszeit, C. Hamelin, T. Brächer, N. Lamard, M.-C. Cyrille, L. Buda-Prejbeanu, K. Garello, I. M. Miron, *et al.*, IEEE Transactions on Magnetics **54**, 1 (2018).

[16] K. Jhuria, J. Hohlfeld, A. Pattabi, E. Martin, A. Y. A. Córdova, X. Shi, R. L. Conte, S. Petit-Watelot, J. C. Rojas-Sanchez, G. Malinowski, *et al.*, Nature Electronics **3**, 680 (2020).

[17] S. Li, S. Goolaup, J. Kwon, F. Luo, W. Gan, and W. S. Lew, Scientific Reports **7**, 1 (2017).

[18] Y.-C. Lau, D. Betto, K. Rode, J. Coey, and P. Stamenov, Nature Nanotechnology **11**, 758 (2016).

[19] S. Peng, D. Zhu, W. Li, H. Wu, A. J. Grutter, D. A. Gilbert, J. Lu, D. Xiong, W. Cai, P. Shafer, *et al.*, Nature Electronics **3**, 757 (2020).

[20] Q. Wang, J. Domann, G. Yu, A. Barra, K. L. Wang, and G. P. Carman, Physical Review Applied **10**, 034052 (2018).

[21] T. Chuang, C. Pai, and S. Huang, Physical Review Applied **11**, 061005 (2019).

[22] S. Łazarski, W. Skowroński, J. Kanak, Ł. Karwacki, S. Ziętek, K. Grochot, T. Stobiecki, and F. Stobiecki, Physical Review Applied **12**, 014006 (2019).

[23] Q. Ma, Y. Li, D. Gopman, Y. P. Kabanov, R. Shull, and C. Chien, Physical Review Letters **120**, 117703 (2018).

[24] D. MacNeill, G. Stiehl, M. Guimaraes, R. Buhrman, J. Park, and D. Ralph, Nature Physics **13**, 300 (2017).

[25] A. M. Humphries, T. Wang, E. R. Edwards, S. R. Allen, J. M. Shaw, H. T. Nembach, J. Q. Xiao, T. J. Silva, and X. Fan, Nature Communications **8**, 1 (2017).

[26] C. B. Seung-heon, V. P. Amin, Y.-W. Oh, G. Go, S.-J. Lee, G.-H. Lee, K.-J. Kim, M. D. Stiles, B.-G. Park, and K.-J. Lee, Nature Materials **17**, 509 (2018).

[27] J.-G. Zhu, Proceedings of the IEEE **96**, 1786 (2008).

[28] W. Zhao, T. Devolder, Y. Lakys, J.-O. Klein, C. Chappert, and P. Mazoyer, Microelectronics Reliability **51**, 1454 (2011).

[29] X. Qiu, P. Deorani, K. Narayanapillai, K.-S. Lee, K.-J. Lee, H.-W. Lee, and H. Yang, Scientific Reports **4**, 1 (2014).

[30] K. Garello, I. M. Miron, C. O. Avci, F. Freimuth, Y. Mokrousov, S. Blügel, S. Auffret, O. Boulle, G. Gaudin, and P. Gambardella, Nature Nanotechnology **8**, 587 (2013).

[31] M. Hayashi, J. Kim, M. Yamanouchi, and H. Ohno, Physical Review B **89**, 144425 (2014).

[32] S. Emori, U. Bauer, S. Woo, and G. S. Beach, Applied Physics Letters **105**, 222401 (2014).

[33] Y. Wang, P. Deorani, X. Qiu, J. H. Kwon, and H. Yang, Applied Physics Letters **105**, 152412 (2014).

[34] M. Isasa, E. Villamor, L. E. Hueso, M. Gradhand, and F. Casanova, Physical Review B **91**, 024402 (2015).

[35] Z. Xu, G. D. H. Wong, J. Tang, E. Liu, W. Gan, F. Xu, and W. S. Lew, Applied Physics Letters **118**, 062406 (2021).

[36] L. Zhu, D. C. Ralph, and R. A. Buhrman, Physical Review B **99**, 180404 (2019).

[37] W. Zhang, W. Han, X. Jiang, S.-H. Yang, and S. S. Parkin, Nature Physics **11**, 496 (2015).

[38] L. Zhu, D. C. Ralph, and R. A. Buhrman, Physical Review Letters **123**, 057203 (2019).

[39] S. Blundell, *Magnetism in condensed matter* (American Association of Physics Teachers, 2003).

[40] J. Schliemann, International Journal of Modern Physics B **20**, 1015 (2006).

[41] G. Vignale, Journal of Superconductivity and Novel Magnetism **23**, 3 (2010).

[42] G. Bihlmayer, O. Rader, and R. Winkler, New Journal of Physics **17**, 050202 (2015).

[43] O. Krupin, G. Bihlmayer, K. Starke, S. Gorovikov, J. Prieto, K. Döbrich, S. Blügel, and G. Kaindl, Physical Review B **71**, 201403 (2005).

[44] K. Shanavas, Z. S. Popović, and S. Satpathy, Physical Review B **90**, 165108 (2014).

[45] R. Rowan-Robinson, *Spin-orbit phenomena and interfacial proximity effects in magnetic multilayers*, Ph.D. thesis, Durham University (2016).

[46] E. Sagasta, Y. Omori, S. Vélez, R. Llopis, C. Tollan, A. Chuvilin, L. E. Hueso, M. Gradhand, Y. Otani, and F. Casanova, Physical Review B **98**, 060410 (2018).

[47] C. Stamm, C. Murer, M. Berritta, J. Feng, M. Gabureac, P. M. Oppeneer, and P. Gambardella, Physical Review Letters **119**, 087203 (2017).

[48] J. Smit, Physica **24**, 39 (1958).

[49] L. Berger, Physical Review B **2**, 4559 (1970).

[50] R. Karplus and J. Luttinger, Physical Review **95**, 1154 (1954).

[51] J. Sinova, S. Murakami, S.-Q. Shen, and M.-S. Choi, Solid State Communications **138**, 214 (2006).

[52] I. M. Miron, G. Gaudin, S. Auffret, B. Rodmacq, A. Schuhl, S. Pizzini, J. Vogel, and P. Gambardella, Nature materials **9**, 230 (2010).

[53] A. Manchon, H. C. Koo, J. Nitta, S. Frolov, and R. Duine, Nature materials **14**, 871 (2015).

[54] T. Tanaka, H. Kontani, M. Naito, T. Naito, D. S. Hirashima, K. Yamada, and J. Inoue, Physical Review B **77**, 165117 (2008).

[55] H. Wang, C. Du, Y. Pu, R. Adur, P. C. Hammel, and F. Yang, Physical review letters **112**, 197201 (2014).

[56] C.-F. Pai, Y. Ou, L. H. Vilela-Leão, D. Ralph, and R. Buhrman, Physical Review B **92**, 064426 (2015).

[57] J. Sinova, S. O. Valenzuela, J. Wunderlich, C. Back, and T. Jungwirth, Reviews of modern physics **87**, 1213 (2015).

[58] T. Kimura, Y. Otani, T. Sato, S. Takahashi, and S. Maekawa, Physical review letters **98**, 156601 (2007).

[59] A. Hoffmann, IEEE transactions on magnetics **49**, 5172 (2013).

[60] A. Brataas, Y. V. Nazarov, and G. E. Bauer, Physical Review Letters **84**, 2481 (2000).

[61] Y. Tserkovnyak, A. Brataas, and G. E. Bauer, Physical Review Letters **88**, 117601 (2002).

[62] K. Carva and I. Turek, Physical Review B **76**, 104409 (2007).

[63] K. Xia, P. J. Kelly, G. Bauer, A. Brataas, and I. Turek, Physical Review B **65**, 220401 (2002).

[64] M. Tokaç, S. Bunyaev, G. Kakazei, D. Schmool, D. Atkinson, and A. Hindmarch, Physical Review Letters **115**, 056601 (2015).

[65] P. Yang, Q. Shao, G. Yu, C. He, K. Wong, X. Lu, J. Zhang, B. Liu, H. Meng, L. He, *et al.*, Applied Physics Letters **117**, 082409 (2020).

[66] Shipley, "Microposit s1800 series photoresists datasheet," `https://amolf.nl/wp-content/uploads/2016/09/datasheets_S1800.pdf`, (Online, Accessed: 01.12.2021).

[67] M. Birkholz and P. F. Fewster, *High-Resolution X-ray Diffraction* (Wiley Online Library, 2005) pp. 297–341.

[68] D. Eastwood, *Durham E-Theses Grazing Incidence X-ray Scattering from Magnetic Thin Films and Nanostructures*, Ph.D. thesis, Ph. D. thesis, Durham University (2009).

[69] E. Hecht, *Optics* (Pearson Education, fifth edition, 2016).

[70] J. Als-Nielsen, D. Jacquemain, K. Kjaer, F. Leveiller, M. Lahav, and L. Leiserowitz, Physics Reports **246**, 251 (1994).

[71] J. Als-Nielsen and D. McMorrow, *Elements of modern X-ray physics* (Wiley, New York, second edition, 2001).

[72] L. G. Parratt, Physical Review **95**, 359 (1954).

[73] H. Kiessig, Annalen der Physik **402**, 715 (1931).

[74] S. Sinha, E. Sirota, S. Garoff, and H. Stanley, Physical Review B **38**, 2297 (1988).

[75] M. Wormington, Philosophical Magazine Letters **74**, 211 (1996).

[76] O.-O. Inyang, *Magnetic proximity effect and interfacial spin dependent transport in ferromagnet/heavy metal thin films*, Ph.D. thesis, Durham University (2018).

[77] J. Kerr, The London, Edinburgh, and Dublin Philosophical Magazine and Journal of Science **3**, 321 (1877).

[78] M. Faraday, Philosophical Transactions of the Royal Society of London **136**, 1 (1846).

[79] Z. Qiu and S. D. Bader, Review of Scientific Instruments **71**, 1243 (2000).

[80] A. Westphalen, M.-S. Lee, A. Remhof, and H. Zabel, Review of Scientific Instruments **78**, 121301 (2007).

[81] I. Soldatov and R. Schäfer, Review of Scientific Instruments **88**, 073701 (2017).

[82] J. Zak, E. Moog, C. Liu, and S. Bader, Journal of Applied Physics **68**, 4203 (1990).

[83] S. D. Bader, Journal of Magnetism and Magnetic Materials **100**, 440 (1991).

[84] J. Bland, M. Padgett, R. Butcher, and N. Bett, Journal of Physics E: Scientific Instruments **22**, 308 (1989).

[85] Tektronix, "TBS1000 series datasheet," `https://uk.tek.com/datasheet/digital-storage-oscilloscopes` (2020).

[86] National Instruments, "PCIe-6351 datasheet," `https://www.ni.com/en-gb/support/model.pcie-6351.html` (2020).

[87] D. Allwood, G. Xiong, M. Cooke, and R. Cowburn, Journal of Physics D: Applied Physics **36**, 2175 (2003).

[88] Thorlabs, "LPS-660-FC product webpage," `https://www.thorlabs.com/thorproduct.cfm?partnumber=LPS-660-FC` (2020).

[89] Thorlabs, "FD11A product webpage," `https://www.thorlabs.com/thorproduct.cfm?partnumber=FD11A` (2020).

[90] T. Spicer, C. Durrant, P. Keatley, V. Kruglyak, W. Chen, G. Xiao, and R. Hicken, Journal of Physics D: Applied Physics **52**, 355003 (2019).

[91] S. Trudel, G. Wolf, H. Schultheiß, J. Hamrle, B. Hillebrands, T. Kubota, and Y. Ando, Review of Scientific Instruments **81**, 026105 (2010).

[92] National Instruments, "Support web pages, signal ghosting," `https://knowledge.ni.com/KnowledgeArticleDetails?id=kA00Z0000019KzzSAE&l=en-GB` (2020).

[93] P. Gambardella and I. M. Miron, Philosophical Transactions of the Royal Society A: Mathematical, Physical and Engineering Sciences **369**, 3175 (2011).

[94] A. Manchon, J. Železnỳ, I. M. Miron, T. Jungwirth, J. Sinova, A. Thiaville, K. Garello, and P. Gambardella, Reviews of Modern Physics **91**, 035004 (2019).

[95] K.-F. Huang, D.-S. Wang, H.-H. Lin, and C.-H. Lai, Applied Physics Letters **107**, 232407 (2015).

[96] L. Liu, O. Lee, T. Gudmundsen, D. Ralph, and R. Buhrman, Physical Review Letters **109**, 096602 (2012).

[97] I. M. Miron, K. Garello, G. Gaudin, P.-J. Zermatten, M. V. Costache, S. Auffret, S. Bandiera, B. Rodmacq, A. Schuhl, and P. Gambardella, Nature **476**, 189 (2011).

[98] L. Liu, C.-F. Pai, Y. Li, H. Tseng, D. Ralph, and R. Buhrman, Science **336**, 555 (2012).

[99] C. Bi, L. Huang, S. Long, Q. Liu, Z. Yao, L. Li, Z. Huo, L. Pan, and M. Liu, Applied Physics Letters **105**, 022407 (2014).

[100] G.-Y. Guo, S. Murakami, T.-W. Chen, and N. Nagaosa, Physical Review Letters **100**, 096401 (2008).

[101] R. Ramaswamy, J. M. Lee, K. Cai, and H. Yang, Applied Physics Reviews **5**, 031107 (2018).

[102] K.-S. Lee, S.-W. Lee, B.-C. Min, and K.-J. Lee, Applied Physics Letters **102**, 112410 (2013).

[103] M. Akyol, G. Yu, J. G. Alzate, P. Upadhyaya, X. Li, K. L. Wong, A. Ekicibil, P. Khalili Amiri, and K. L. Wang, Applied Physics Letters **106**, 162409 (2015).

[104] G. Yu, P. Upadhyaya, Y. Fan, J. G. Alzate, W. Jiang, K. L. Wong, S. Takei, S. A. Bender, L.-T. Chang, Y. Jiang, *et al.*, Nature Nanotechnology **9**, 548 (2014).

[105] B. Cui, H. Wu, D. Li, S. A. Razavi, D. Wu, K. L. Wong, M. Chang, M. Gao, Y. Zuo, L. Xi, *et al.*, ACS Applied Materials & Interfaces **11**, 39369 (2019).

[106] S. Fukami, C. Zhang, S. DuttaGupta, A. Kurenkov, and H. Ohno, Nature Materials **15**, 535 (2016).

[107] Y.-W. Oh, S.-h. C. Baek, Y. Kim, H. Y. Lee, K.-D. Lee, C.-G. Yang, E.-S. Park, K.-S. Lee, K.-W. Kim, G. Go, *et al.*, Nature Nanotechnology **11**, 878 (2016).

[108] A. van den Brink, G. Vermijs, A. Solignac, J. Koo, J. T. Kohlhepp, H. J. Swagten, and B. Koopmans, Nature Communications **7**, 1 (2016).

[109] K. Cai, M. Yang, H. Ju, S. Wang, Y. Ji, B. Li, K. W. Edmonds, Y. Sheng, B. Zhang, N. Zhang, *et al.*, Nature Materials **16**, 712 (2017).

[110] L. You, O. Lee, D. Bhowmik, D. Labanowski, J. Hong, J. Bokor, and S. Salahuddin, Proceedings of the National Academy of Sciences **112**, 10310 (2015).

[111] J. M. Lee, K. Cai, G. Yang, Y. Liu, R. Ramaswamy, P. He, and H. Yang, Nano Letters **18**, 4669 (2018).

[112] A. Pimpin and W. Srituravanich, Engineering Journal **16**, 37 (2012).

[113] M. Yasaka *et al.*, The Rigaku Journal **26**, 1 (2010).

[114] S. Grauby, B. Forget, S. Hole, and D. Fournier, Review of Scientific Instruments **70**, 3603 (1999).

[115] G. Tessier, M. Polignano, S. Pavageau, C. Filloy, D. Fournier, F. Cerutti, and I. Mica, Journal of Physics D: Applied Physics **39**, 4159 (2006).

[116] T. Favaloro, A. Ziabari, J.-H. Bahk, P. Burke, H. Lu, J. Bowers, A. Gossard, Z. Bian, and A. Shakouri, Journal of Applied Physics **116**, 034501 (2014).

[117] T. Favaloro, J.-H. Bahk, and A. Shakouri, Review of Scientific Instruments **86**, 024903 (2015).

[118] R. Wilson, B. A. Apgar, L. W. Martin, and D. G. Cahill, Optics Express **20**, 28829 (2012).

[119] B. Rodmacq, A. Manchon, C. Ducruet, S. Auffret, and B. Dieny, Physical Review B **79**, 024423 (2009).

[120] T. Young Lee, D. Su Son, S. Ho Lim, and S.-R. Lee, Jounral of Applied Physics **113**, 216102 (2013).

[121] L.-X. Ye, C.-M. Lee, J.-W. Syu, Y.-R. Wang, K.-W. Lin, Y.-H. Chang, and T.-h. Wu, IEEE Transactions on Magnetics **44**, 3601 (2008).

[122] J. Torrejon, G. Malinowski, M. Pelloux, R. Weil, A. Thiaville, J. Curiale, D. Lacour, F. Montaigne, and M. Hehn, Physical Review Letters **109**, 106601 (2012).

[123] J. Curiale, A. Lemaître, G. Faini, and V. Jeudy, Applied Physics Letters **97**, 243505 (2010).

[124] S. Woo, M. Mann, A. J. Tan, L. Caretta, and G. S. Beach, Applied Physics Letters **105**, 212404 (2014).

[125] J.-C. Rojas-Sánchez, P. Laczkowski, J. Sampaio, S. Collin, K. Bouzehouane, N. Reyren, H. Jaffrès, A. Mougin, and J.-M. George, Applied Physics Letters **108**, 082406 (2016).

[126] N. Perez, E. Martinez, L. Torres, S.-H. Woo, S. Emori, and G. Beach, Applied Physics Letters **104**, 092403 (2014).

[127] S. Mizukami, E. Sajitha, D. Watanabe, F. Wu, T. Miyazaki, H. Naganuma, M. Oogane, and Y. Ando, Applied Physics Letters **96**, 152502 (2010).

[128] L. Melo, A. Vaz, M. Salvadori, and M. Cattani, Journal of Metastable and Nanocrystalline Materials **20**, 623 (2004).

[129] N. Gusev, I. Y. Pashen'kin, M. Sapozhnikov, O. Udalov, and P. Yunin, Technical Physics **64**, 1646 (2019).

[130] D. Ravelosona, D. Lacour, J. Katine, B. Terris, and C. Chappert, Physical Review Letters **95**, 117203 (2005).

[131] P. Haazen, E. Murè, J. Franken, R. Lavrijsen, H. Swagten, and B. Koopmans, Nature Materials **12**, 299 (2013).

[132] K. Kinoshita, H. Honjo, S. Fukami, R. Nebashi, K. Tokutome, M. Murahata, S. Miura, N. Kasai, S. Ikeda, and H. Ohno, Japanese Journal of Applied Physics **53**, 03DF03 (2014).

[133] R. Hertel, arXiv preprint arXiv:0804.4010 (2008).

[134] P. Zhang, Y. Lau, and R. Gilgenbach, Journal of Physics D: Applied Physics **48**, 475501 (2015).

[135] P. Zhang, Y. Lau, and R. S. Timsit, IEEE Transactions on Electron Devices **59**, 1936 (2012).

[136] H. Murrmann and D. Widmann, IEEE Transactions on Electron Devices **16**, 1022 (1969).

[137] M. Bogdanov, K. Bulashevich, O. Khokhlev, I. Y. Evstratov, M. Ramm, and S. Y. Karpov, Physica Status Solidi C **7**, 2124 (2010).

[138] M.-H. Nguyen, D. Ralph, and R. Buhrman, Physical Review Letters **116**, 126601 (2016).

[139] H.-D. Liu, Y.-P. Zhao, G. Ramanath, S. Murarka, and G.-C. Wang, Thin Solid Films **384**, 151 (2001).

[140] B. Krüger, *Current-Driven Magnetization Dynamics: Analytical Modeling and Numerical Simulation*, Ph.D. thesis, University of Hamburg (2012).

[141] M. Gradhand, D. V. Fedorov, P. Zahn, and I. Mertig, Physical Review B **81**, 245109 (2010).

[142] K. Kondou, H. Sukegawa, S. Mitani, K. Tsukagoshi, and S. Kasai, Applied Physics Express **5**, 073002 (2012).

[143] X. Tao, Q. Liu, B. Miao, R. Yu, Z. Feng, L. Sun, B. You, J. Du, K. Chen, S. Zhang, *et al.*, Science Advances **4**, eaat1670 (2018).

[144] W. Zhang, V. Vlaminck, J. E. Pearson, R. Divan, S. D. Bader, and A. Hoffmann, Applied Physics Letters **103**, 242414 (2013).

[145] S. Emori, U. Bauer, S.-M. Ahn, E. Martinez, and G. S. Beach, Nature Materials **12**, 611 (2013).

[146] J. Kim, J. Sinha, M. Hayashi, M. Yamanouchi, S. Fukami, T. Suzuki, S. Mitani, and H. Ohno, Nature Materials **12**, 240 (2013).

[147] L. Liu, R. Buhrman, and D. Ralph, arXiv preprint arXiv:1111.3702 (2011).

[148] M. Jamali, K. Narayanapillai, X. Qiu, L. M. Loong, A. Manchon, and H. Yang, Physical Review Letters **111**, 246602 (2013).

[149] R. M. Rowan-Robinson, A. Hindmarch, and D. Atkinson, Journal of Applied Physics **124**, 183901 (2018).

[150] T. Schulz, K. Lee, B. Krüger, R. L. Conte, G. V. Karnad, K. Garcia, L. Vila, B. Ocker, D. Ravelosona, and M. Kläui, Physical Review B **95**, 224409 (2017).

[151] K. Meng, J. Miao, X. Xu, Y. Wu, X. Zhao, J. Zhao, and Y. Jiang, Physical Review B **94**, 214413 (2016).

[152] K. Hasegawa, M. Mizuguchi, Y. Sakuraba, T. Kamada, T. Kojima, T. Kubota, S. Mizukami, T. Miyazaki, and K. Takanashi, Applied Physics Letters **106**, 252405 (2015).

[153] T. Seki, R. Iguchi, K. Takanashi, and K. Uchida, Journal of Physics D: Applied Physics **51**, 254001 (2018).

[154] A. Bose, S. Bhuktare, H. Singh, S. Dutta, V. Achanta, and A. Tulapurkar, Applied Physics Letters **112**, 162401 (2018).

[155] P. Metaxas, J. Jamet, A. Mougin, M. Cormier, J. Ferré, V. Baltz, B. Rodmacq, B. Dieny, and R. Stamps, Physical Review Letters **99**, 217208 (2007).

[156] C. Hin Sim, J. Cheng Huang, M. Tran, and K. Eason, Applied Physics Letters **104**, 012408 (2014).

[157] P. Sethi, S. Krishnia, S. Li, and W. Lew, Journal of Magnetism and Magnetic Materials **426**, 497 (2017).

[158] S. Chen, D. Li, B. Cui, L. Xi, M. Si, D. Yang, and D. Xue, Journal of Physics D: Applied Physics **51**, 095001 (2018).

[159] V. Vlaminck, J. E. Pearson, S. D. Bader, and A. Hoffmann, Physical Review B **88**, 064414 (2013).

[160] Z. Feng, J. Hu, L. Sun, B. You, D. Wu, J. Du, W. Zhang, A. Hu, Y. Yang, D. Tang, *et al.*, Physical Review B **85**, 214423 (2012).

[161] H. Nakayama, K. Ando, K. Harii, T. Yoshino, R. Takahashi, Y. Kajiwara, K.-i. Uchida, Y. Fujikawa, and E. Saitoh, Physical Review B **85**, 144408 (2012).

[162] O. Mosendz, J. Pearson, F. Fradin, G. Bauer, S. Bader, and A. Hoffmann, Physical Review Letters **104**, 046601 (2010).

[163] H. Nakayama, M. Althammer, Y.-T. Chen, K.-i. Uchida, Y. Kajiwara, D. Kikuchi, T. Ohtani, S. Geprägs, M. Opel, S. Takahashi, *et al.*, Physical Review Letters **110**, 206601 (2013).

[164] J. Kim, P. Sheng, S. Takahashi, S. Mitani, and M. Hayashi, Physical Review Letters **116**, 097201 (2016).

[165] S. Marmion, M. Ali, M. McLaren, D. Williams, and B. Hickey, Physical Review B **89**, 220404 (2014).

[166] S. Cho, S.-h. C. Baek, K.-D. Lee, Y. Jo, and B.-G. Park, Scientific Reports **5**, 1 (2015).

[167] D. Meier, D. Reinhardt, M. Van Straaten, C. Klewe, M. Althammer, M. Schreier, S. T. Goennenwein, A. Gupta, M. Schmid, C. H. Back, *et al.*, Nature Communications **6**, 1 (2015).

[168] M. Gamino, J. Santos, A. Souza, A. Melo, R. Della Pace, E. Silva, A. Oliveira, R. Rodríguez-Suárez, F. Bohn, and M. Correa, Journal of Magnetism and Magnetic Materials **527**, 167778 (2021).

[169] B. Yang, Y. Xu, M. Schneider, J. Shi, *et al.*, in *APS March Meeting Abstracts*, Vol. 2014 (2014) pp. D48–013.

[170] A. W. Wells, P. M. Shepley, C. H. Marrows, and T. A. Moore, Physical Review B **95**, 054428 (2017).

[171] C. Deger, Scientific Reports **10**, 1 (2020).

[172] A. Hrabec, N. Porter, A. Wells, M. Benitez, G. Burnell, S. McVitie, D. McGrouther, T. Moore, and C. Marrows, Physical Review B **90**, 020402 (2014).

[173] T. Fache, J. Rojas-Sanchez, L. Badie, S. Mangin, and S. Petit-Watelot, Physical Review B **102**, 064425 (2020).

[174] S. Karimeddiny, J. A. Mittelstaedt, R. A. Buhrman, and D. C. Ralph, Physical Review Applied **14**, 024024 (2020).

[175] M. Alghamdi, M. Lohmann, J. Li, P. R. Jothi, Q. Shao, M. Aldosary, T. Su, B. P. Fokwa, and J. Shi, Nano Letters **19**, 4400 (2019).

[176] M. Akyol, W. Jiang, G. Yu, Y. Fan, M. Gunes, A. Ekicibil, P. Khalili Amiri, and K. L. Wang, Applied Physics Letters **109**, 022403 (2016).

[177] L. Zhu, D. Ralph, and R. Buhrman, Physical Review Letters **122**, 077201 (2019).

[178] S. Ikeda, K. Miura, H. Yamamoto, K. Mizunuma, H. Gan, M. Endo, S. Kanai, J. Hayakawa, F. Matsukura, and H. Ohno, Nature Materials **9**, 721 (2010).

[179] C.-W. Cheng, W. Feng, G. Chern, C. Lee, and T.-h. Wu, Journal of Applied Physics **110**, 033916 (2011).

[180] H.-Y. Lee, S. Kim, J.-Y. Park, Y.-W. Oh, S.-Y. Park, W. Ham, Y. Kotani, T. Nakamura, M. Suzuki, T. Ono, *et al.*, APL Materials **7**, 031110 (2019).

[181] Y. Chen, Q. Zhang, J. Jia, Y. Zheng, Y. Wang, X. Fan, and J. Cao, Applied Physics Letters **112**, 232402 (2018).

[182] X. Li, K. Fitzell, D. Wu, C. T. Karaba, A. Buditama, G. Yu, K. L. Wong, N. Altieri, C. Grezes, N. Kioussis, *et al.*, Applied Physics Letters **110**, 052401 (2017).

[183] C. Swindells, H. Głowiński, Y. Choi, D. Haskel, P. Michałowski, T. Hase, P. Kuświk, and D. Atkinson, Applied Physics Letters **119**, 152401 (2021).

[184] H. Yuasa, K. Tamae, and N. Onizuka, AIP Advances **7**, 055928 (2017).

[185] X. Ma, G. Yu, X. Li, T. Wang, D. Wu, K. S. Olsson, Z. Chu, K. An, J. Q. Xiao, K. L. Wang, *et al.*, Physical Review B **94**, 180408 (2016).

[186] C. Swindells, A. Hindmarch, A. Gallant, and D. Atkinson, Applied Physics Letters **116**, 042403 (2020).

[187] O. Inyang, L. Bouchenoire, B. Nicholson, M. Tokaç, R. Rowan-Robinson, C. Kinane, and A. Hindmarch, Physical Review B **100**, 174418 (2019).

[188] M. TOKAÇ, Cumhuriyet Science Journal **42**, 715 (2021).

[189] K. Tsunekawa, Y.-S. Choi, Y. Nagamine, D. D. Djayaprawira, T. Takeuchi, and Y. Kitamoto, Japanese Journal of Applied Physics **45**, L1152 (2006).

[190] A. Gayen, G. K. Prasad, S. Mallik, S. Bedanta, and A. Perumal, Journal of Alloys and Compounds **694**, 823 (2017).

[191] A. Hindmarch, A. Rushforth, R. Campion, C. Marrows, and B. Gallagher, Physical Review B **83**, 212404 (2011).

[192] S. J. Yoon, B. G. Kim, I. T. Jeon, J. H. Wu, and Y. K. Kim, Applied Physics Express **5**, 103003 (2012).

[193] A. Soundararaj and J. Mohanty, Surface Engineering and Applied Electrochemistry **56**, 159 (2020).

[194] E. Yun, W. Win, and R. Walser, IEEE Transactions on Magnetics **32**, 4535 (1996).

[195] C. O. Avci, K. Garello, C. Nistor, S. Godey, B. Ballesteros, A. Mugarza, A. Barla, M. Valvidares, E. Pellegrin, A. Ghosh, *et al.*, Physical Review B **89**, 214419 (2014).

[196] Y. Ou, C.-F. Pai, S. Shi, D. Ralph, and R. Buhrman, Physical Review B **94**, 140414 (2016).

[197] A. Hindmarch, K. Dempsey, D. Ciudad, E. Negusse, D. Arena, and C. Marrows, Applied Physics Letters **96**, 092501 (2010).

[198] H. Sato, P. Chureemart, F. Matsukura, R. Chantrell, H. Ohno, and R. Evans, Physical Review B **98**, 214428 (2018).

[199] J. G. Alzate, P. Khalili Amiri, G. Yu, P. Upadhyaya, J. A. Katine, J. Langer, B. Ocker, I. N. Krivorotov, and K. L. Wang, Applied Physics Letters **104**, 112410 (2014).

[200] K. Fukamichi and R. Gambino, IEEE Transactions on Magnetics **17**, 3059 (1981).

[201] M. Tokaç, Journal of Non-Crystalline Solids **572**, 121080 (2021).

[202] L. A. Giannuzzi and F. A. Stevie, Micron **30**, 197 (1999).

[203] H. Matsui, H. Toyoda, and H. Sugai, Journal of Vacuum Science & Technology A: Vacuum, Surfaces, and Films **23**, 671 (2005).

[204] M. Cecot, Ł. Karwacki, W. Skowroński, J. Kanak, J. Wrona, A. Żywczak, L. Yao, S. van Dijken, J. Barnaś, and T. Stobiecki, Scientific Reports **7**, 1 (2017).

[205] Z. Zhu, B. Zhao, W. Zhu, M. Tang, Y. Ren, Q. Jin, and Z. Zhang, Applied Physics Letters **113**, 222403 (2018).